Intracellular micromechanics of the syncytial *Drosophila* embryo

by Alok Daniel Weßel

Intracellular micromechanics of the syncytial *Drosophila* embryo

Dissertation

for the award of the degree
„Doctor rerum naturalium"
of the Georg-August-Universität Göttingen

within the doctoral program

Physics of Biological and Complex Systems

of the Göttingen Graduate School for Neurosciences, Biophysics, and Molecular Biosciences (GGNB)

of the Georg-August University School of Science (GAUSS)

submitted by

Alok Daniel Weßel

from Friedberg, Germany

Göttingen, January 30th, 2015

Members of the thesis committee:

Prof. Dr. Christoph F. Schmidt (1st reviewer and supervisor)
Drittes Physikalische Institut
Georg-August Universität Göttingen

Prof. Dr. Jörg Großhans (2nd reviewer)
Institut für Entwicklungsbiochemie, Universitätsmedizin
Georg-August Universität Göttingen

Prof. Dr. Detlev Schild
Abteilung für Neurophysiologie und Zelluläre Biophysik, Universitätsmedizin
Georg-August Universität Göttingen

Additional members of the examination committee:

Dr. Iwan Schaap
Drittes Physikalische Institut - Biophysik
Georg-August Universität Göttingen

Prof. Dr. Anette Zippelius
Institut für Theoretische Physik
Georg-August Universität Göttingen

Prof. Dr. Sarah Köster
Institut für Röntegenphysik
Georg-August Universität Göttingen

Date of the oral examination: March 23rd, 2015

Affidavit

I herewith declare that I have produced this dissertation without the prohibited assistance of third parties and without making use of aids other than those specified; notions taken over directly or indirectly from other sources have been identified as such. This dissertation has not previously been presented in identical or similar form to any other German or foreign examination board.

The thesis work was conducted from February 2011 to January 2015 under the supervision of Prof. Dr. Christoph F. Schmidt at the Third Institute of Physics - Biophysics.

Alok Daniel Weßel   Göttingen, January 30th, 2015

Abstract

A developing embryo is a striking and fascinating example of self-organization and collective behavior of biological matter. In the presented work, I investigated the cytoplasmic interior of *Drosophila melanogaster* embryos. In its early stage the embryo forms a syncytium, i.e. multiplying nuclei are not yet separated by cell membranes, but are interconnected by cytoskeletal polymer networks consisting of actin and microtubules. Between division cycles 9 and 13, nuclei form a 2D cortical layer with the cytoskeleton associated to it. To probe the mechanical properties and dynamics of this self-organizing "pre-tissue", I measured shear moduli in the embryo by high-speed video microrheology. Therefore, I built a multi-color fluorescence microscope for simultaneously imaging at high speeds with frame rates of up to several kHz and at normal video rates in order to access an extended frequency range. I recorded position fluctuations of injected micron-sized fluorescent beads and characterized the viscoelasticity of the embryo in different locations. Thermal fluctuations dominated over non-equilibrium activity for frequencies between 0.3 and 1000 Hz. Between nuclear layer and central yolk the cytoplasm was homogeneous and viscously-dominated, with a viscosity three orders of magnitude higher than that of water. Close to the nuclear layer, particularly close to the cortex, I found an increase of the elastic and viscous moduli consistent with an increased microtubule density. Mechanical response near the nuclear layer is likely to be caused by loosely entangled microtubule networks, whereas in the interior, towards the central yolk, it is due to a macromolecular solution. Drug-interference experiments showed that microtubules contribute to the measured viscoelasticity inside the embryo, whereas actin only plays a minor role in the regions I probed with the micron sized beads, i.e. outside of the actin caps and cortex. Measurements at different stages of the nuclear division cycle showed little variation. During nuclear separation at anaphase I found directed motion of probe particles, the only measurable sign for non-equilibrium activity, so far.

Secondly I investigated single-walled carbon nanotubes (CNT) as fluorescent and trappable probes by means of the custom-built setup incorporating near-infrared imaging and spectroscopy instruments as well as multiple trapping lasers and an interferometric detection system. CNTs have an intrinsic near-infrared fluorescence, emitting within a wavelength window almost free of autofluorescence in biological tissue. Hence, imaging of single CNTs injected into the whole living fly embryo by wide-field microscopy was possible. Mean squared displacements of tracked CNTs within the embryonic cytoplasm showed diffusive and subdiffusive motion as well as

directed movements, some of them correlating with nuclear motion. *In vitro* experiments characterized CNTs as fluorescent probes, lacking fluorescence intermittency, exhibiting short fluorescence cycle lifetimes and high photostability (though lower than in previous findings). I optically trapped CNTs, simultaneously confirmed by fluorescence microscopy and interferometric detection. The shape of a position power spectral density of a trapped CNT was close to a Lorentzian and the measurement of the position variance allowed a determination of the number of trapped particles. No clear signs for resonance effects on trapping efficiency were observed.

Table of contents

Introduction | 1

In the following thesis I will show and explain theoretical basics and results of measurements I performed under the supervision and in the labs of Prof. C. F. Schmidt at the third physical institute at the university of Göttingen. The subject was the characterization of intracellular mechanics of the early *Drosophila* embryo by means of micron-sized probes as well as carbon nanotubes with sizes on the nanometer scale.

Motivation | 1.1

Biophysics is the science where physical principles and methods are applied to biological systems to measure and model their behavior. Thereby a unique range of interesting phenomena was found. In the field of structure formation and mechanics biological materials are a fascinating example of self-organizing soft matter, i.e. by itself they form complex structures to perform dynamic functions. Their heterogeneous structure leads to a broad range of mechanical responses on stress depending on the probed timescale. Single cells, for instance, were found to be elastic on timescales of seconds but start to flow on longer timescales [1–3]. Furthermore, cells and biological matter are not simply passive objects. They seem to circumvent the second law of thermodynamics to form autonomous islands of low entropy, i.e. high ordering. The truth is that molecular machines in various forms transform chemical energy (mostly in the form of ATP and GTP) into mechanical forces. The cytoskeleton, for example, is a structural element of every eukaryotic cell consisting of extended polymers and associated proteins. On the one hand, it was found to exert forces by itself, due to polymerization of cytoskeletal filaments like actin and microtubules. On the other hand, it provides a scaffold for transmitting forces generated by molecular motor proteins, which bind to it and translate along it [4, 5]. These mechanisms enable cells to sense and transduce forces [6]. Biological systems are out of equilibrium and often referred to as 'active matter'.

The next step is the quantitative understanding of collective behavior on the mesoscopic level and its interplay with molecular dynamics on the microscopic scale. The understanding and modeling of collective phenomena in complex active matter will have impact on medical tissue treatment and the new field of tissue engineering.

The biological subject for the presented studies here are developing fly embryos, which are an impressive example of self-organizing biological matter. The fruit fly *Drosophila melanogaster* is a well established system in biology, particularly in the research field of developmental biology. Its embryo is transparent (to a certain extent), the number of cells is still small, it is rapidly developing and genetically well-studied and controlled . Its molecular structure, particularly cytoskeletal structures, are extensively studied and resolved [7–9]. In its early developmental stages the embryo forms a syncytium, i.e. multiplying nuclei are not yet separated by cell membranes, but are interconnected by cytoskeletal polymer networks consisting of actin and microtubules. In the syncytial stage, nuclei and cytoskeleton form a well-structured 2D cortical layer.

A bottom-up approach to understand cell mechanics is the study of (active) cytoskeletal networks *in vitro* [10, 11]. The distribution of filaments inside the syncytial embryo makes it an interesting system to study the mechanical properties of *in-vivo* networks. Furthermore, it can be seen as a giant single cell developing towards multi-cellular tissue, hence being kind of a 'pre-tissue'.

There exist several techniques in the field of biophysics to study mechanical properties of soft matter [11]. In general rheology is the science of flow and deformation of matter. It characterizes the response of a material to an applied stress. A standard method is the use of large-scale rheometers, which measure bulk properties of viscoelastic materials. A special variant called microrheology is more appropriate for applications in biological systems since it measures mechanical properties locally, on the micrometer length scale [12].

In the presented work I studied the mechanical properties of the cytoplasm of early fly embryos including a cortical, well-structured monolayer of nuclei and associated cytoskeletal structure. I could then characterize the viscoelastic interior of the fly eggs.

As stated above, the formation of well-organized patterns in active materials can be modeled as an interplay of active force generating elements in a viscoelastic medium. Therefore, a detailed understanding of single motor proteins and their potential communication with each other is crucially needed. To approach this problem we introduced novel nanostructures as fluorescent markers into the fly embryo. Carbon nanotubes have an intrinsic fluorescence within a near-infrared wavelength window, which is almost free of autofluorescence in biological tissue. Hence, they turned out to be highly promising fluorescent markers for single-molecule imaging within whole organisms [13]. In fact we recently showed that the high photostability and lack of fluorescence intermittency of carbon nanotubes allowed long term tracking of single motor proteins within cells [14], where typical single molecule studies suffered from short recording times due to blinking and fast bleaching. Thus, I applied the same methodology onto early fly embryos to study its cytoplasm and potential motor dynamics.

A thorough single- molecule study of motor proteins within cells and tissue includes a characterization of force generating processes. For that purpose local force sensors are needed. Furthermore, it is favorable to locally exert forces with a well-known

spectrum to analyze responses of the surrounding (which is the bridge to microrheology again). Within the last two decades the use of optical tweezers became a standard technique in the biosciences [15, 16]. A focused laser beam traps dielectric particles due to radiation forces. Typically glass or latex beads in the order of microns are used as probes. For intracellular experiments these sizes are often not feasible. Moreover, forces are exerted indiscriminately to other objects than the probe. In the last decade, triggered by the increased advent of nanotechnology, trapping of nanostructures was reported [17]. Therefore, I investigated the capability of optically trapping single carbon nanotubes. For even smaller particles, namely neutral atoms it was shown that they can be trapped due to enhanced responses to optical forces near optical dipole transitions. The presented work is approaching the question if this is possible for carbon nanotubes, too. In sum, the motivation for this part of the project was to find small probes for intracellular force measurements, which might have a probe-specific enhanced trapping efficiency.

Outline | 1.2

The requirement for near-infrared fluorescence microscopy, optical trapping and high-speed microscopy for video-based microrheology necessitated the construction of a complex measuring setup. This setup is described in detail in chapter 2. Control experiments prove its multi-fold features. The capability of an optimized NIR imaging made the following publication possible:

N. Fakhri, **A. D. Wessel**, C. Willms, M. Pasquali, D. R. Klopfenstein, F. C. MacKintosh, and C. F. Schmidt, "High-resolution mapping of intracellular fluctuations using carbon nanotubes", Science, vol. 344, no. 6187, pp. 1031-1035, 2014

Chapter 3 explains the theoretical basis of microrheology and gives a detailed description of the numerical implementation of the method. The analysis routines are a collection of preexisting tracking and microrheology scripts as well as self-written Matlab programs. Noise sources and artifacts will be discussed as well as how they are compensated. Control experiments characterize tracking performance and prove a correct calibration.
The main experimental result of the thesis is presented in chapter 4: The viscoelastic properties within the syncytial fly embryo were measured in different regions of the embryo, at different time points during the nuclear division cycle and in chemically perturbed embryos. The results will be published in a paper that is submitted and currently under revision:

Alok D. Wessel, Maheshwar G. Reddy, Jörg Grosshans, Christoph F. Schmidt, "The mechanical properties of early Drosophila embryos measured by high-speed video microrheology"

In chapter 5 carbon nanotubes are introduced as luminescent probes. Their fluorescent properties were characterized. I also show tracking results of carbon nanotubes dispersed within early fly embryos.

The theoretical basics for understanding enhanced optical trapping near resonances and the experimental results of carbon nanotube trapping are given in chapter 6. Chapter 7 concludes the work and gives an outlook for potential follow-up investigations in future.

The custom-built setup | 2

The construction, extension and optimization of the measurement instrument was an important part of the work for this thesis. It resulted in a multi-functional and complex setup, which had undergone steady development and improvements. The setup contains mainly two sections. The first one covers the function of multi-color high-speed imaging which was used for the application of video microrheology and visible/ near-infrared imaging. The second part contains equipment and devices for optical trapping, which is related to the subproject of carbon nanotube trapping. Both parts are integrated in one setup and can be used simultaneously. They will be described in detail in this section.

Description of the setup | 2.1

Key components of the setup are the two fixed objectives, one in a vertical orientation, the other one in a horizontal orientation (see fig. 2.1 and 2.2). The first one is a Nikon 63x high-NA (1.27) water-immersion objective with especially high optical transmission in the near infrared range (for details see item (1) in the particle list in the appendix). The second one is a Zeiss 100x high-NA (1.46) oil-immersion objective (2). A sample stage is associated to the objective. It is mounted onto a positioning unit, which is manually adjustable along the xyz axis with micrometer screws (3). The sample stage at the Nikon objective has an additional three-axes piezo positioner (4) with positioning precision in the nanometer range. Also the sample holder at the Zeiss objective has an additional piezo positioning unit with nanometer precision (5) and is steerable along the optical axis (see fig. 2.3 D). Both objectives are used in epifluorecence geometry. There are five lasers for illumination (see fig. 2.3 E), they emit at wavelengths of 488 nm (50 mW, Coherent Obis, (6)), 532 nm (50 mW, Coherent Compass, (7)), 561 nm (500 mW, Cobolt Jive, (8)) and 637 nm (25 mW, Coherent Cube, (9)). The intensity of the 488 nm, 532 nm and 637 nm laser is adjusted by neutral density filter wheels with a gradient in optical density (10). The power of the 561 nm laser can be adjusted by turning a $\lambda/2$ waveplate, which is followed by a polarizer. The four lasers are coincided by appropriate dichroic mirrors (13,14,15) and expanded with a telescope lens pair with focal lengths of $f_1 = 40\ mm$ and $f_2 = 300\ mm$ (16,17). The fifth illumination laser is a titanium-sapphire laser (see fig. 2.3 F) with tuneable wavelengths (range 725-820, see section 2.3) when used in continuous emission mode (Coherent Mira, (18)). Its
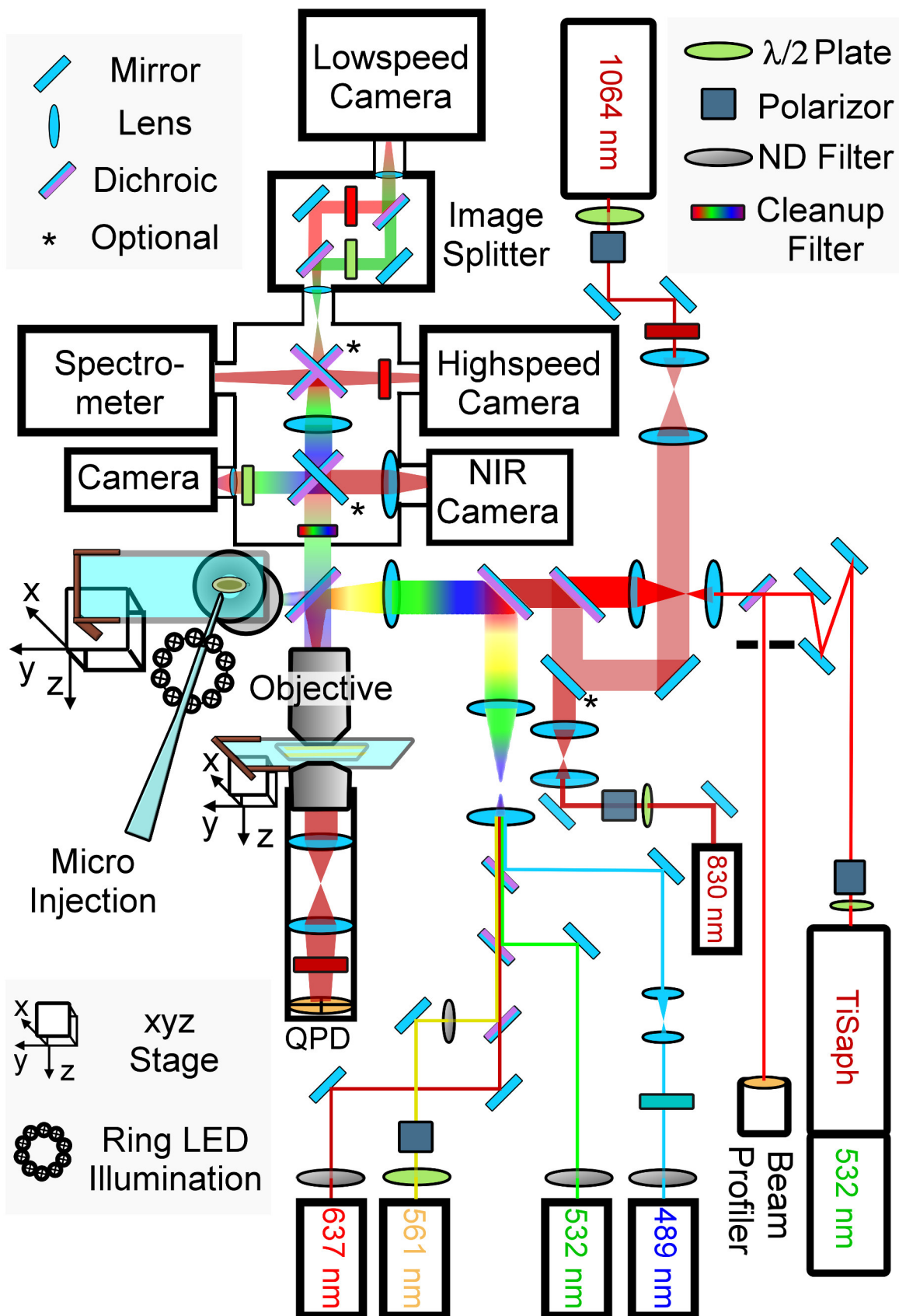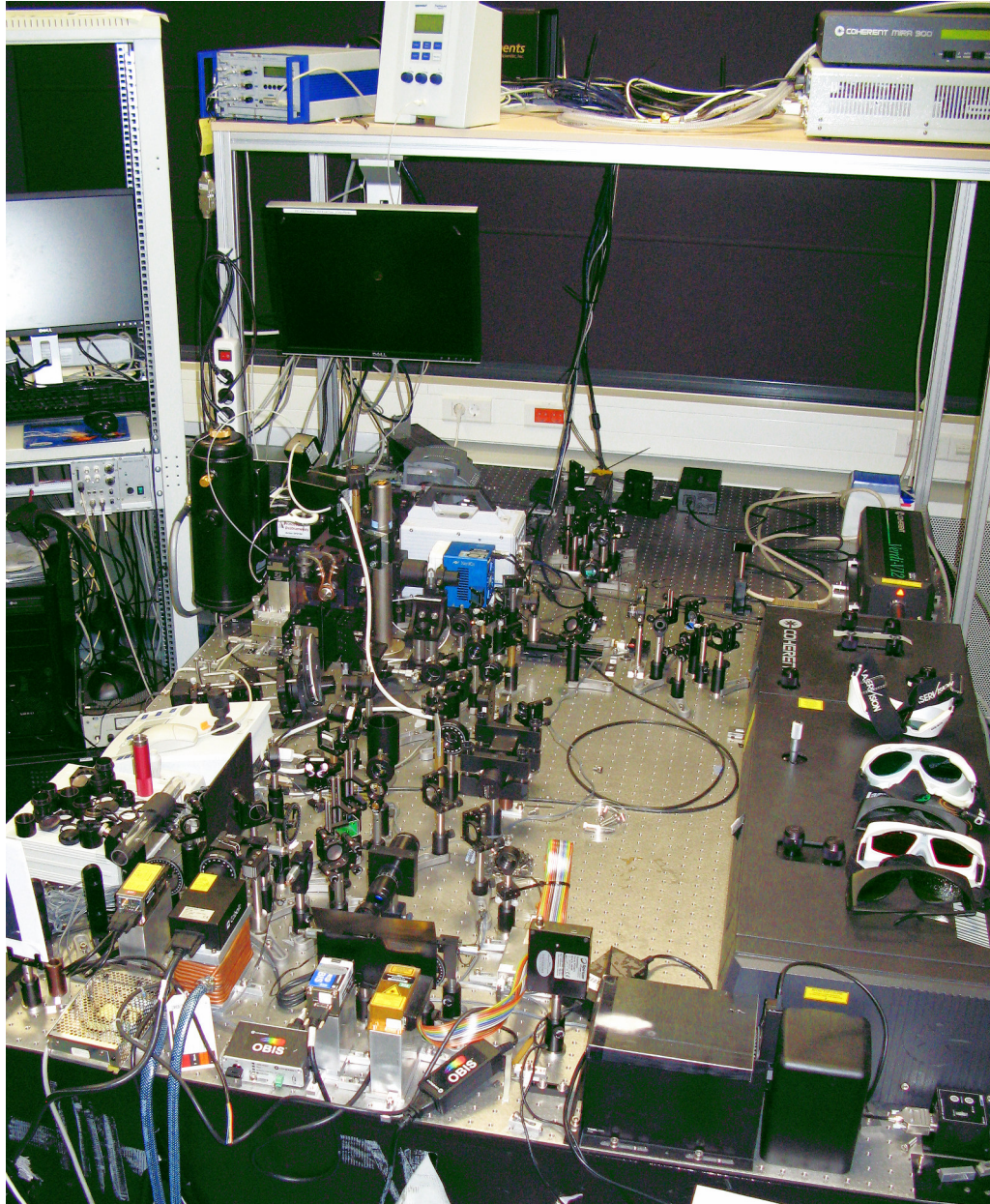
Figure 2.1: Schematic drawing of the measurement setup

Figure 2.2: Illustrating picture of the measurement setup

intensity can be adjusted by a combination of a $\lambda/2$ waveplate followed by a polarizer. The beam traverses a combination of mirrors for beam steering (see section 2.4.3), which also includes pinholes and a beam profiler (19) and is then expanded by a pair of telescope lenses with focal lengths of $f_3 = 35\ mm$ and $f_4 = 150\ mm$ (20, 21). The five illumination lasers are then coincided by a dichroic mirror (25) and directed onto a lens, which focuses the light into the back focal plane of one of the objectives. There is the option of using different lenses $f_5 = 150\ mm$, $f_6 = 150\ mm$, $f_7 = 75\ mm$ (22,23,24) for the different objectives and sizes of illuminated fields of view. There are different exchangeable dichroic mirror which can be placed in front of the Zeiss objective (25,26,27) in order to mirror the light into the objective and let the emitted light pass through in a long-pass manner. The dichroic mirror for the Nikon objective is a special multi short-pass dielectric mirror (28).
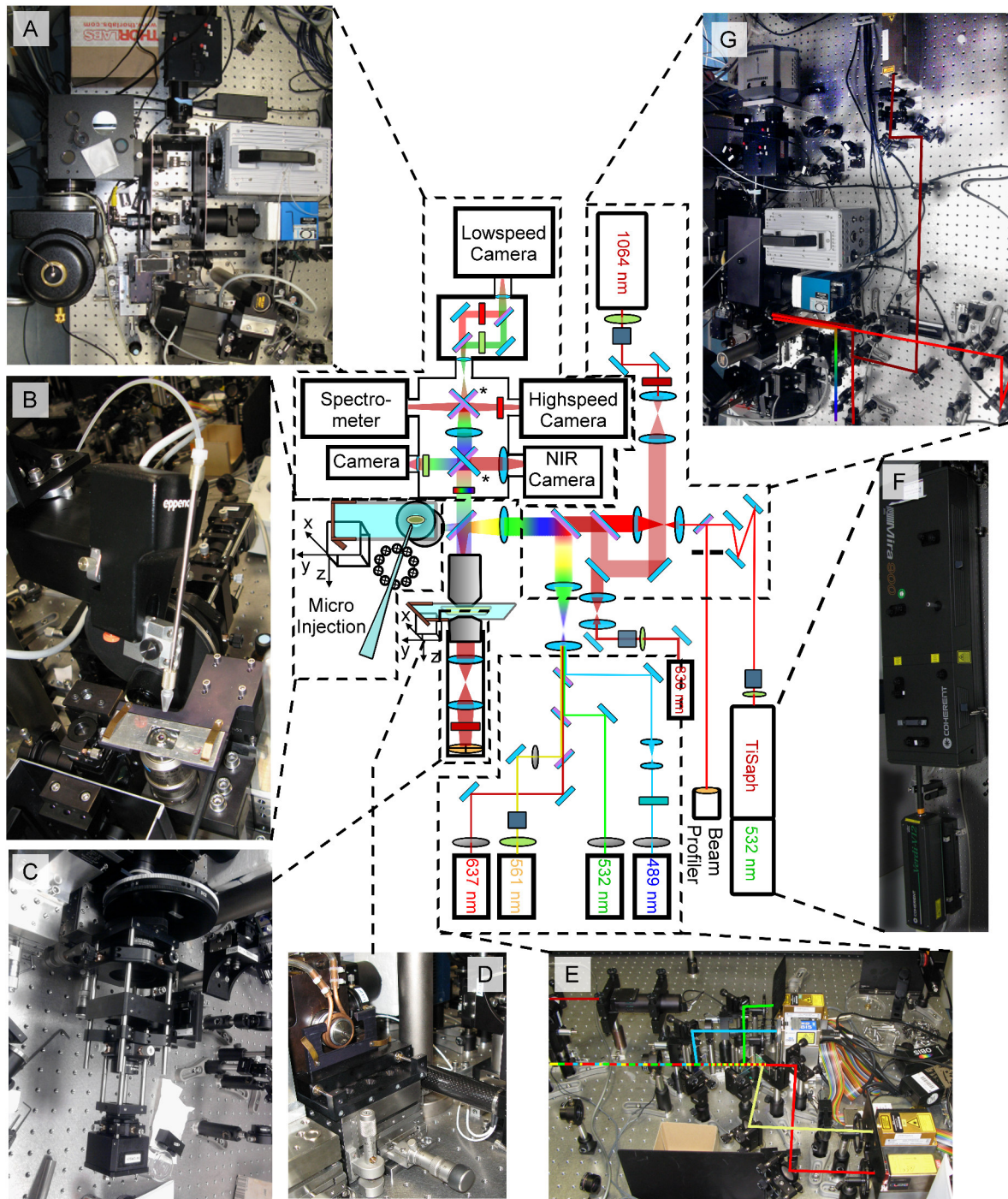
Figure 2.3: Illustrating pictures of the measurement setup
(A) Detection part showing the aluminum box at the center surrounded by four cameras, the image splitter and the spectrometer. **(B)** Nikon objective with sample holder and injection needle holder. **(C)** Interferometric laser tweezer detection. **(D)** Zeiss objective with a heating tube attached to it and its associated sample stage with manual and piezo positioning elements. **(E)** Laser excitation and trapping sources (beginning at the front): 637 nm, 561 nm, 488 nm, 532 nm, and 830 nm. **(F)** Titanium-sapphire laser with its optical pumping laser. **(G)** Beam path of the titanium sapphire, 830 nm and 1064 nm trapping lasers.

The Nikon objective is equipped with an Eppendorf injection needle holder (see fig. 2.3 B) and micro injector (29,30). On the detection side there is a combination of mirrors and filters in a light-shielding aluminum box providing different light

paths according to different detectors (see fig. 2.3 A): First the light passes through one of the emission filters mounted in a filter wheel.

1. Then the sample plane can optionally be imaged onto the chip of a Xenics near infrared sensitive, Indium Gallium Arsenide, CMOS camera (31) after traversing an infrared long-pass filter (32), a mirror and a tube lens $f_{TL,1} = 165\ mm$ (33). This light path was used for near-infrared imaging (see chapter 5).

2. The light can also be deflected onto a video camera (34). It is filtered (35) and focused onto the camera chip by a lens with a focal length of $f_8 = 60\ mm$ (36). Here we obtain a comparably low magnification of 18x of the sample. This detection path was used for micro injection (see chapter 4).

3. In a third detection path an exchangeable tube lens (either a Nikon lens with $f_{TL,2} = 200\ mm$ (37) or a Zeiss lens with $f_{TL,1} = 165\ mm$ (33) focuses the light into the input plane of an image splitter (38). In there, a lens collimates the light to split it by means of a dichroic mirror (39) by color into a green and a red channel. In both channels light is filtered with emission filters (40,41) and then mirrored and imaged onto different regions of an Andor low-noise EMCCD camera (42). This detection channel was particularly used to image green fluorescing GFP and red fluorescing beads (see chapter 4). In general the dichroic splitting filter cube can be replaced by a single channel cube.

4. A dichroic mirror (43) can be placed between the tube lens and the image splitter to simultaneously direct the red light onto a Photron high-speed CMOS camera (44) after filtering (45). This detection path was used to do high-speed imaging of red fluorescent beads (see chapter 4).

5. By placing a mirror between tube lens and image splitter a fifth detection path can be used: Here, the light is focused into the input plane of a spectrometer (46, details see section 2.3).

There are three infrared laser sources for the purpose of optical trapping: a 1064 nm Coherent Compass laser (47), a 830 nm diode laser (48), and the titanium-sapphire laser. The intensity of the 1064 nm laser can be adjusted by the use of a $\lambda/2$ waveplate and a polarizer. Then the beam is expanded by a telescope lens pair with focal lengths of $f_9 = 50\ mm$ and $f_{10} = 150\ mm$ (49, 50). By that the beam has a diameter of approx. 5.5 mm in order to overfill the back aperture of the objective. Then it is coincided with the beam of the titanium-sapphire laser by means of an appropriate dichroic mirror (51) and the visible laser beams and finally hits the objective centered and perpendicular where it forms the optical trap (see fig. 2.3 G).
The 830 nm laser's intensity is adjusted by a $\lambda/2$ waveplate followed by a polarizer. The beam is expanded by a pair of lenses with focal lengths of $f_{11} = 30\ mm$ and $f_{12} = 100\ mm$ (52, 53). One of the mirrors used to deflect the 1064 nm laser is switchable. By taking it out of the beam path the 830 nm laser can be coincided with the titanium-sapphire laser to finally hit the objective and form a trap.
The principle of laser interferometry is used to detect the position of a trapped

object (see section 2.4.1). Therefore, a Zeiss condenser (54) collects the light of the optical trap (see fig. 2.3 C). A lens pair with focal lengths of $f_{13} = 250\ mm$ and $f_{14} = 45\ mm$ (55,56) images the back focal plane of the condenser onto a quadrant photo diode (57). The light is filtered in front of the diode with an appropriate bandpass filter (58).

2.2 | Multi-color imaging and high-speed microscopy

As described in section 2.1 the setup has different detection channels and according cameras, which can be used simultaneously or subsequently by replacing mirrors. Images of the same sample were taken to proof this (see fig. 2.4). The use of a
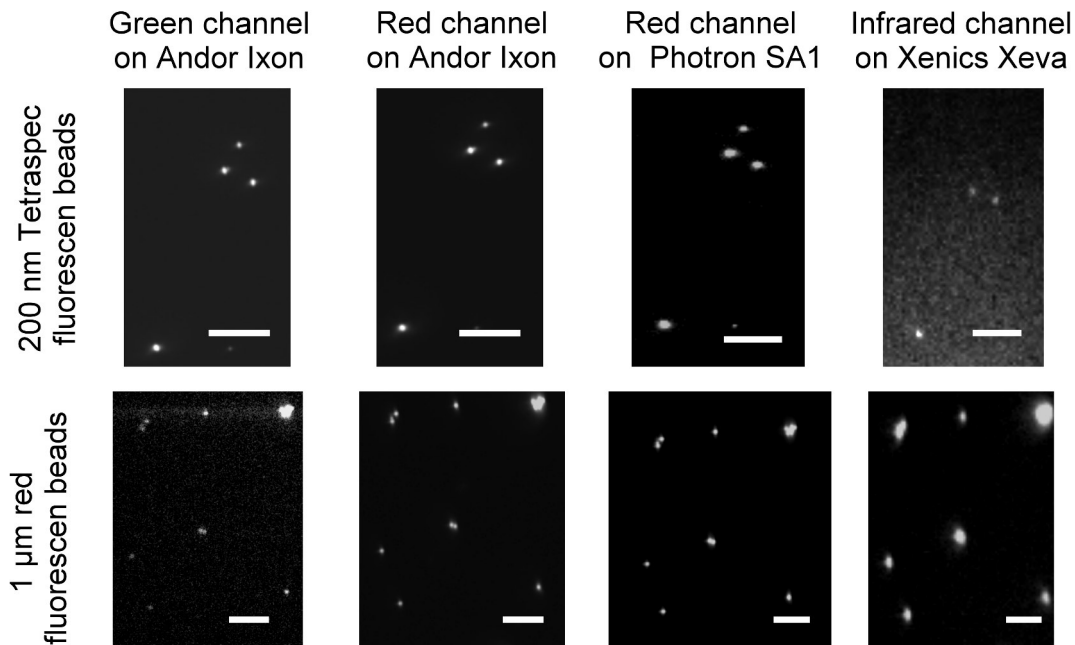
Figure 2.4: Exemplary fluorescence images of multi-color beads
Images showing the same fluorescent beads recorded in the different detection channels of the setup. First row: 200 nm TetraSpec™ beads, which emit light over a broad range of wavelengths. Second row: $1\ \mu m$ diameter red fluorescent microspheres, which where used for the microrheology measurements. A sixfold higher illumination intensity was used to get a strong enough signal of the TetraSpec™beads in the near infrared channel and a strong enough signal of the red beads in the green channel. Scale bar: $10\ \mu m$

high-speed camera is a special feature of the setup. As expected, we found that high illumination intensities are needed for fast imaging. The higher the frame rate, the lower gets the exposure time and thus the number of collected photons whereas a part of the noise floor stays constant. Figure 2.5 illustrates the clear need of illumination intensities up to 300 mW (leading to peak power illumination densities of $\varrho = 6\ kW/cm^2$) in order to image at frame rates up to 8 or even 16 kHz, which was desirable for the video-microrheology experiments. Figure 3.6 in chapter 3 will show that a too low light intensity at high-speed sampling interferes with a correct determination of particle's fluctuations.
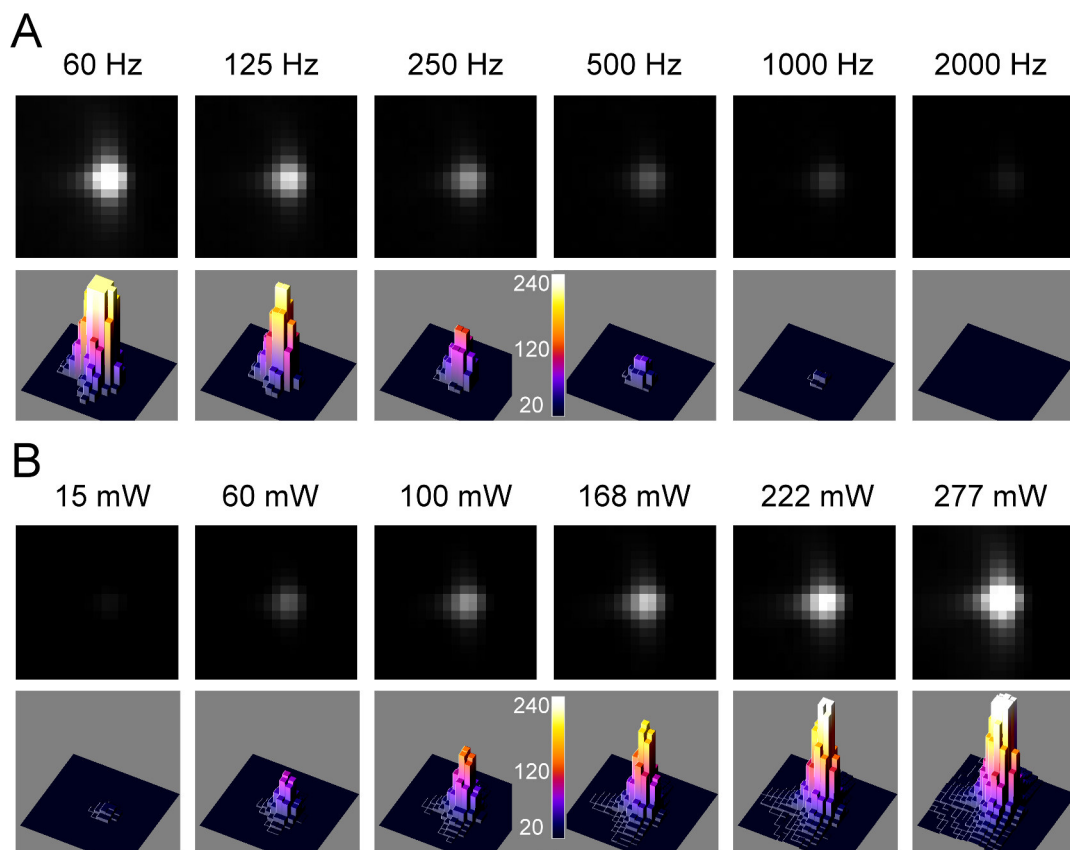
Figure 2.5: Images and intensity maps of fluorescing beads at different frame rates and excitation intensities
(A) Series of fluorescence images of the $1~\mu m$ red fluorescent beads taken with the Photron high-speed camera at different frame rates (first row). Intensity maps of the imaged beads show a strong decrease of the signal to noise ratio with increasing frame rate (second row). Images were taken at an illumination intensity of 6 mW corresponding to an intensity density of 120 W/cm^2. **(B)** Images of a red fluorescing bead taken at a frame rate of 8 kHz for increasing illumination intensities (first row). The 3D intensity maps of the depicted beads show that high illumination intensities are needed to restore a good signal to noise ratio when imaging with high sampling frequencies (second row).

2.3 | **Near-infrared fluorescence spectroscopy**

A spectrometer is an instrument which collects a light signal, spreads the light in space as a function of wavelength and measures the intensity of these spatial distinct rays. The spectrometer used for our setup is a combination of an Acton spectrograph with a near-infrared sensitive InGaAs detector (46) consisting of a 512 linear array of liquid nitrogen cooled photo diodes. The spectrograph has a Czerny Turner geometry [18]: A curved mirror (b) collimates the light coming from the entrance slit (a) and reflects it onto a grating (c) (see fig. 2.6 A). The grating reflects the incoming light at different angles according to their wavelength. A second curved mirror (d) images the entrance slit onto the detector (e). The Acton spectrograph
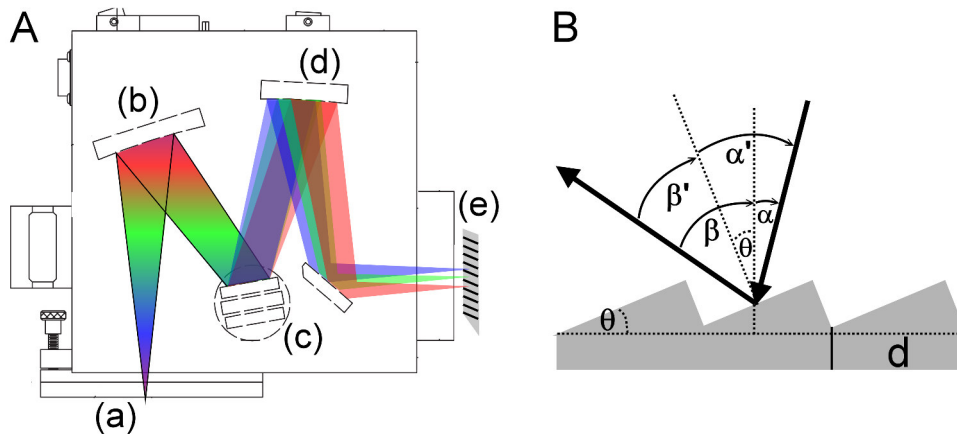
**Figure 2.6: Schematic illustrations of the key elements of a spectrometer**
(A) Schematic drawing of the light path inside the acton sp-2150 spectrograph. **(B)** Geometry of a blazed grating with line distance d. Adapted from [19]

has two grating slots. A stepping motor can exchange the gratings and set the angle between incident ray and grating normal. The grating is the spectrum-resolving element. The fundamental grating equation states that $\sin(\alpha) + \sin(\beta) = g \cdot k \cdot \lambda$ where α, β are the angle of incidence and diffraction, respectively, g is the density of grooves in the grating, λ is the wavelength of light and k is the order of refraction (see fig. 2.6 B). Our spectrometer uses blazed gratings where each grating line has a saw-tooth shape in order to optimize the refractive efficiency for one refraction order of a certain wavelength (the 'blazed' wavelength). The incident and refracted rays have angles α and β to the normal of the substrate. The long face of the triangle is tilted against the substrate by an angle θ so that $\alpha' = \beta' = \theta$ [20].

By rotating the grating with respect to the incoming light, different parts of the angular spectrum will be imaged onto the detector array. Each angle corresponds to a center wavelength of the limited wavelength window on the detector. Therefore, the instrument must be calibrated for different center wavelengths.

In order to translate the pixel number of the detector array into a physical unit the spectrometer has to be calibrated. This has to be done for each grating and center wavelength separately. As a first step the 300 groves/mm grating was aligned to a center wavelength of 725 nm just enough to see the 489 nm laser at the lower bound of this wavelength window. Then the lasers with the wavelengths of 532 nm, 561 nm, 637 nm and a diode alignment laser were used to produce a reference signal (see fig. 2.7 A). By that a wavelength window up to approximately 950 nm could be calibrated. In a second step I measured the tuneable wavelength of the titanium-sapphire laser, which was in the range of 725 nm to 820 nm and used these peaks as new reference signals (see fig. 2.7 B).
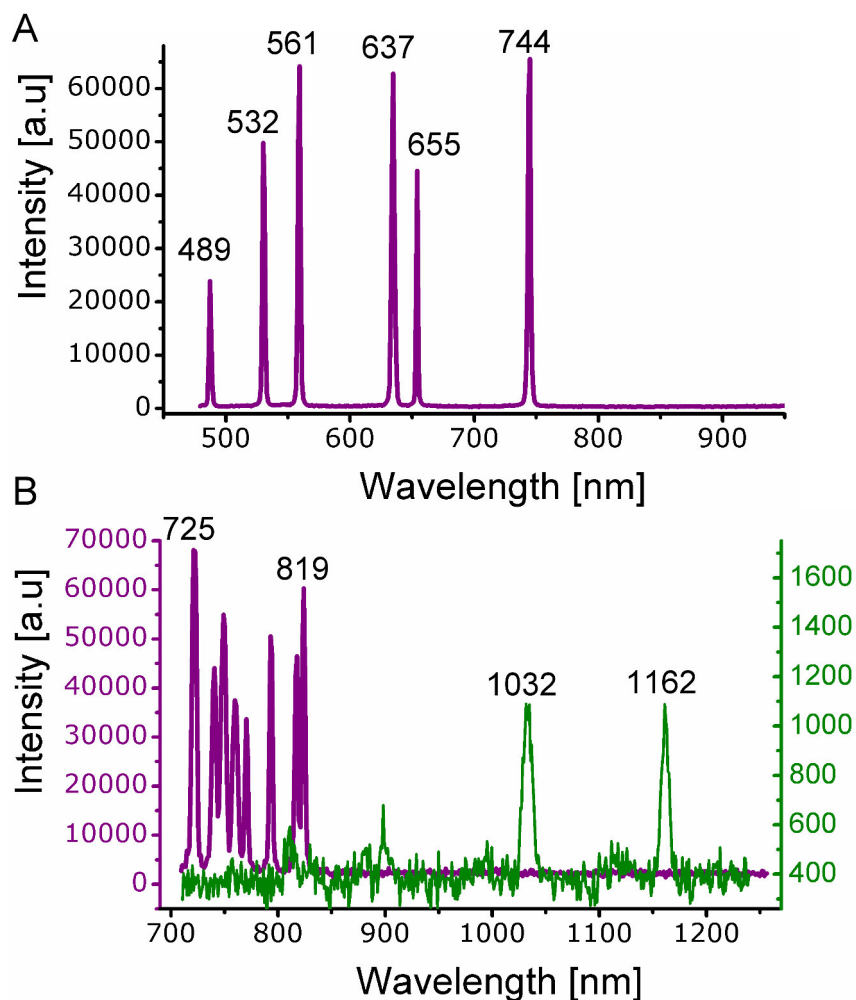
Figure 2.7: Calibration of the spectrometer
(A) Spectrum of six lasers mirrored into the spectrometer. The lasers from 489 nm to 655 nm were use as reference signals to calibrate this wavelength window with a center wavelength of 725 nm and to determine the tuneable wavelength of the titanium-sapphire laser, which in this case was 744 nm. **(B)** The outputs of the titanium-sapphire laser with its different wavelengths was used to calibrate the wavelength window with a center wavelength of 950 nm. Interestingly the room light has two distinct emission peaks, which made calibrations at even longer wavelengths possible.

By that a wavelength window of approximately 710 nm to 1190 nm with a center wavelength of 950 nm could be calibrated. By chance I found the room light, a neon tube, to have two sharp and distinct emission peaks at 1032 nm an 1162 nm. This fact made a calibration of the range from 970nm to 1430 nm, center wavelength 1200 nm, possible. By that a wavelength range from 480 nm to 1430 nm could, in principle, be measured.
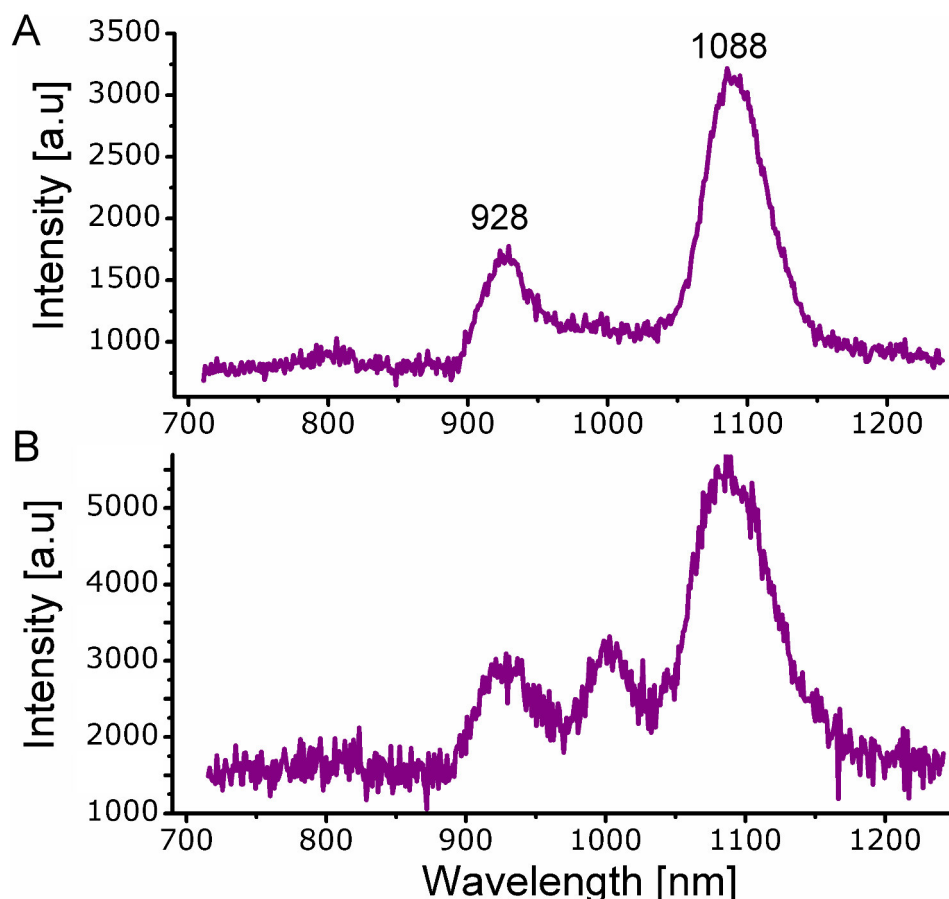
Figure 2.8: Calibration of the spectrometer
(A) Spectrum of a plain glass water chamber recorded close to the coverslip. The two broad peaks stem from fluorescence of the glass. **(B)** A carbon nanotube sample imaged in a glass water chamber. Compared to panel A one can see a third peak but the background signal interferes with it.

Figure 2.8 shows two spectra. The first spectrum was taken from a plain sample chamber built with standard glass coverslips and filled with water. When illuminated with the 561 nm laser or the titanium-sapphire laser the glass fluoresces leading to the two depicted peaks. Figure 2.8 B shows the spectrum of an individual carbon nanotube on a glass surface. The mentioned fluorescence signal from the glass strongly interferes with the nanotube signal. That is why we used cover slides made of quartz for NIR imaging.

Photons carry a momentum $p = h/\lambda$, which will be transferred partly upon reflection or refraction to a dielectric particle. Under certain conditions the arising forces can form a potential well, in which the particle can be trapped. For particles much larger than the wavelength ray optics can be applied (the case of small objects will be discussed in chapter 6). If photons are reflected from the particle's surface a net force along the light beam will arise, the scattering force.
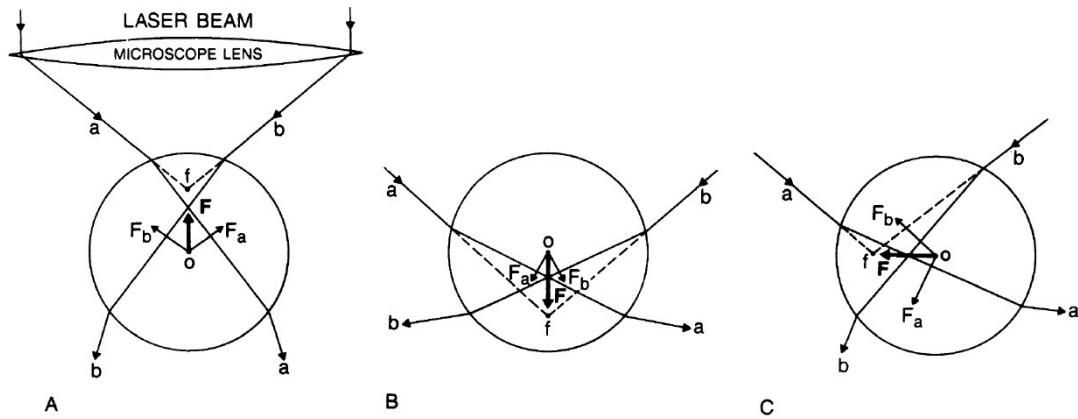
Figure 2.9: Ray-optics description of the gradient force
An objective lens focuses a laser beam to a focal point f. **(A)**-**(C)** show three possible positions of a microsphere O with respect to the focus. The two outermost rays a and b are shown. They are refracted when impinging onto the particle. In all cases momentum transfer causes a net force $\vec{F} = \vec{F}_a + \vec{F}_b$ towards the focus of the beam, the gradient force. Adapted from [21].

Figure 2.9 A-C qualitatively introduces a second force caused by momentum transfer by showing three possible locations of a refractive particle with respect to the focal spot of a focused light beam. The force which occurs is due to a gradient in intensity, hence called gradient force. It always points along the intensity gradient towards the focus. That is why lenses with high numerical apertures are used to create steep gradients. Besides this simple understanding of the gradient force a thorough calculation includes multiple refractions and reflections as well as polarization effects. The optical trapping pioneer Ashkin gives a complete calculation for the ray optics scenario in [21].

Interferometric detection | 2.4.1

A convenient way to detect the position of a trapped particle with high temporal and spatial resolution is to detect an interferometric pattern. It arises from a superposition of the trapping laser and the part of the beam which is scattered by the trapped particle. Gittes and Schmidt [22] calculated the first order angular far field distribution of intensity of a Rayleigh particle laterally being displaced from the focus by x to be

$$\frac{\delta I_{\theta,\phi}(x)}{I_{tot}} = \frac{2k^3\alpha}{\pi r^2} \exp\left(-x^2/\omega_0^2\right) \cdot \sin\left(kx\sin\theta\cos\phi\right) \exp\left(-k^2\omega_0^2\theta^2/4\right)$$

where $\delta I_{\theta,\phi}(x)/I_{tot}$ is the relative change of intensity under angles θ, ϕ (see fig. 2.10) at distance r, which is the principal plane of the condenser. ω_0 is the $1/e^2$ radius of the waist of a zero-order Gaussian beam, k is the wave number and α the polarizability. A condenser collects the light and translates the angular distribution into
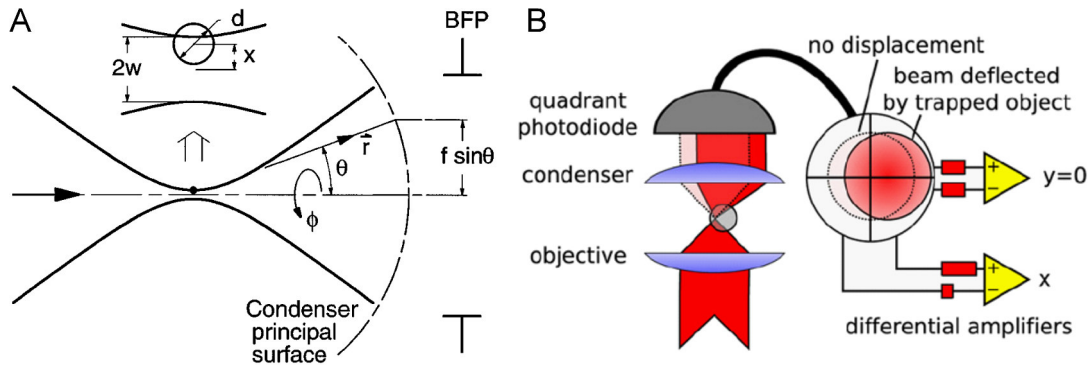
Figure 2.10: Interferometric detection of a trapped particle
(A) Explanation of the scattering position and angles of a trapped particle: x is the lateral displacement of a sphere with diameter d in a beam with waist w, scattering light under angles (θ, ϕ). A condenser with focal length f collects scattered and unscattered light. **(B)** Principle of an interferometric detection of a trapped particle with a quadrant photo diode: A lateral offset of a trapped particle from the focus causes a displaced interference pattern on the QPD, which is recognized by a differential amplifier. Adapted from [22] and [23].

a spatial intensity distribution at it's back focal plane (BPF). The BFP is imaged onto a quadrant photo diode (QPD), which is aligned with the x- and y-axis. In order to calculate the amounts of light falling onto the two halves (+) and (-) of the QPD along the $\pm$x-axis one integrates the angular distribution and obtains (for small $\theta \approx 0$) the detector response

$$\frac{I_+ - I_-}{I_+ + I_-} = \frac{16k\alpha}{\sqrt{\pi}\omega_0^2} \exp\left(-2x^2/\omega_0^2\right) \int_0^{x/\omega_0} \exp(y^2)dy$$

The last part is Dawson's integral and can be calculated numerically [24]. The response depends on particle diameter and size of the beam waist. In the range of about $\pm$ 200 nm it can be well approximated to be linear.

Figure 2.11 A shows a picture of how the interferometric detection was implemented in the setup used for this thesis. Two lenses image the BFP of the condenser with an appropriate magnification onto the QPD (see fig. 2.11 H and section 2.1). This was proven by sharply imaging the iris at the BFP of the condenser (see fig. 2.11 B) with a camera, which had replaced the QPD for that purpose. Figure 2.11 C-G show exemplary images of the BFP when a 2 μm particle was trapped, thermally fluctuating around the trap center.
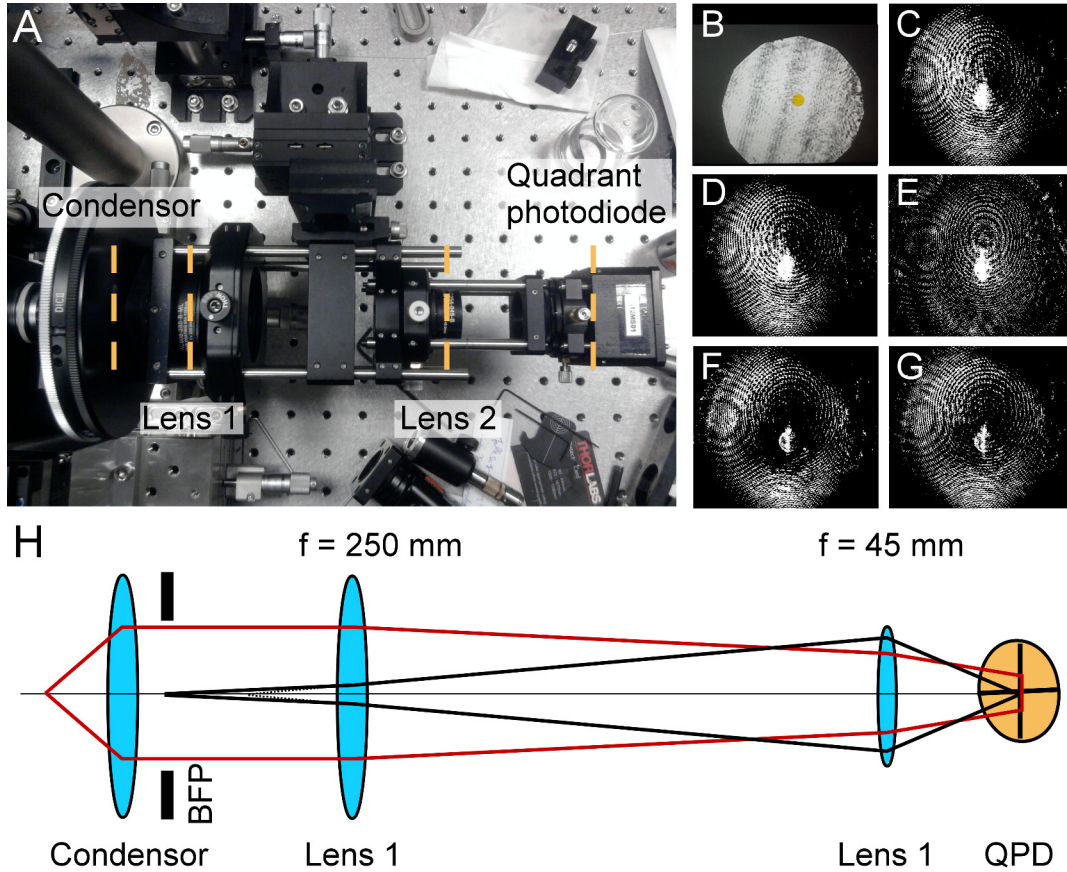
Figure 2.11: Interferometric detection of trapped particles
(A) Picture of the interferometric detection system incorporating two lenses, which image the back focal plane (BFP) of a condenser onto a quadrant photo diode (QPD). **(B)** The image shows the half-opened iris at the BFP of the condenser recorded by a camera placed at the plane of the QPD. By that a correct BFP imaging and magnification can be confirmed. **(C - G)** Images of the condenser's BFP when a $2\ \mu m$ polystyrene bead was optically trapped. One can see an interference pattern, which is changing over time according to the position of the bead relative to the trap center. **(H)** Schematic drawing of the light path (red) and the BFP imaging (black).

Trapping microspheres | 2.4.2

Trapping polystyrene microspheres with a diameter of $2\ \mu m$ worked with the titanium-sapphire laser, the 830 nm laser and the 1064 nm. An exemplary dataset of a red fluorescing bead trapped by the 1064 nm laser is shown in figure 2.12. The bead was trapped and detected by the interferometric detection and simultaneously its fluorescence was recorded. The bead's center of mass trajectory shows the confinement of its motion by the trap (see fig. 2.12 A) until the optical tweezer is turned off. Since the force responsible for trapping is linear in a certain range around the trap center, the motion of a trapped particle can be modeled as a thermally driven overdamped motion in a harmonic potential.

$$m\frac{d^2\mathbf{x}}{dt^2} = -\gamma\frac{d\mathbf{x}}{dt} + \kappa x + \boldsymbol{\zeta}\left(t\right) \tag{2.1}$$
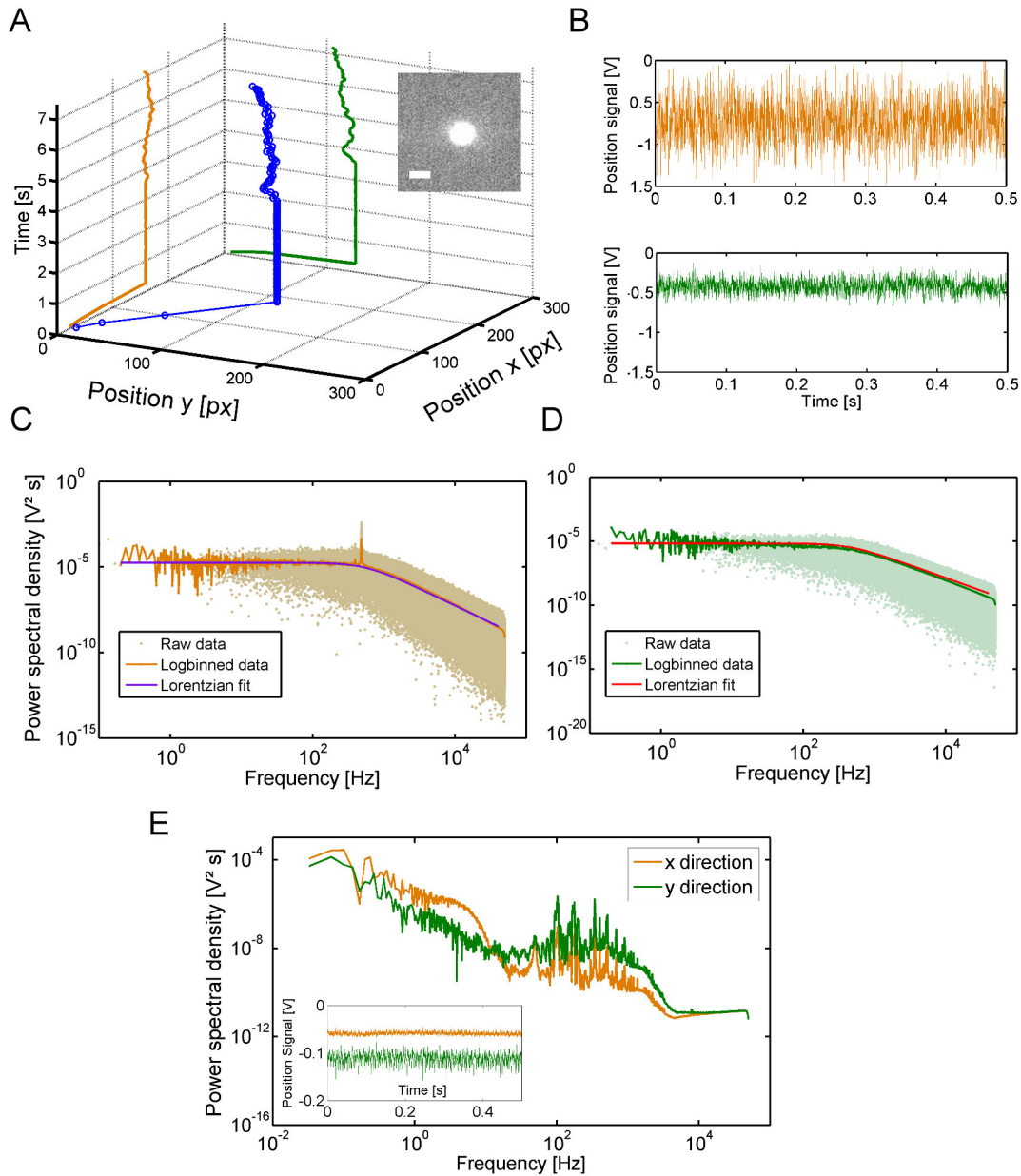
Figure 2.12: Position signal and PSD of a trapped bead
(A) The 3D plot shows the position time trajectory of a microsphere recorded with a video camera while being optically trapped and released. The trajectory shows the bead's center of mass being pulled into the trap center. It stays trapped for a few seconds until the trap is turned off and the bead starts its free Brownian motion. Inset: Fluorescence image of the $2~\mu m$ red fluorescent polystyrene bead, simultaneously imaged while optically trapped. Scale bar: $3~\mu m$. **(B)** Position signal over time of the first half of a second taken by the interferometric position detection. The two curves correspond to x and y direction. **(C)** and **(D)** Power spectral density of the bead's position signal inside the optical trap in x and y direction, respectively. The shaded dots show the raw data whereas the solid orange and green lines correspond to a mean signal averaged over 750 logarithmically spaced bins. The pink and red solid lines show the fitted function of a Lorentzian form $PSD(f) = A/(f^2 + f_c^2)$ with $A_x = 5.5 \pm 2.1~V^2$, $A_y = 1.3 \pm 3.1~V^2$ and corner frequencies of $f_{c,x} = 554.3 \pm 28.9~Hz$ and $f_{c,y} = 451.0 \pm 18.3~Hz$. The data points are in good agreement with the theoretical expectations for an over damped particle in a harmonic potential. **(E)** Control measurement: Power spectral density and QPD voltage signal (inset) of an empty trap in water.

with mass of the particle m, friction coefficient γ, constant of the restoring force κ and the random thermal force ζ, which originates from the collision of the particles with solvent molecules. Latter one has a constant 'white noise' spectrum $|\zeta(f)|^2 = 4\gamma k_B T$ and it is $\langle \zeta(t) \rangle = 0$. The power spectral density of the particle's position is the absolute squared of the Fourier transformed position signal, and hence given by [25]

$$S(f) = \frac{k_B T}{\gamma \pi^2 (f_c^2 + f^2)}$$

where $f_c = \kappa/2\pi\gamma$ is the so called corner frequency.

Figure 2.12 C and D show exemplary PSDs of a trapped microsphere, which follow very well the proposed Lorentzian shape and which is well above the noise floor measure with an empty trap (see fig. 2.12 E).

Trapping with the titanium-sapphire laser | 2.4.3

One of the original ideas of the project was to use the titanium-sapphire laser as a trapping laser of which the wavelength could be tuned in order to study the wavelength dependence of trapping forces. However, this laser turned out to be technically challenging in the sense of trapping. At some point beam pointing instabilities occurred, which interfered with the requirement for a stable trap detection. Figure
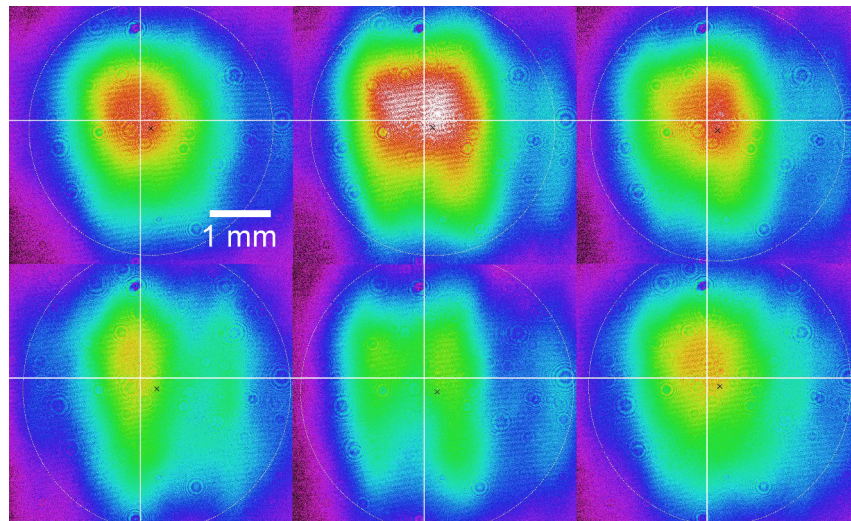
Figure 2.13: **Beam pointing instabilities of the titanium-sapphire laser**
Six false-color images of the beam profile of the titanium-sapphire laser taken within a period of 3 hours during strong shape and angular fluctuations. Colors code for intensity, ranging from red (high value) over green to blue (low value).

2.13 shows six images of the beam profile taken at a period of strong fluctuations of the beam's shape and position. Though an extreme example it illustrates the problem of this unstable laser. Probably these fluctuations are caused by a feedback loop for the temperature control of the diode laser, which pumps the Verdi laser, which then again pumps the titanium-sapphire laser. However, it was possible to

trap particles with the titanium-sapphire laser but the beam fluctuations interfered with the interferometric detection (see fig. 2.14).
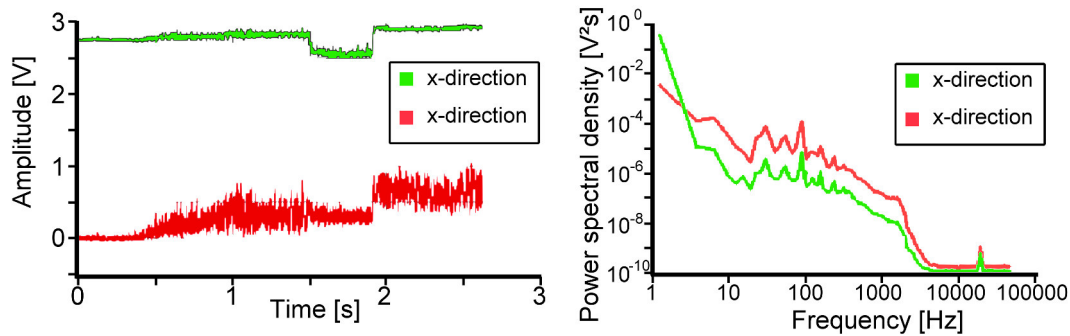
Figure 2.14: Beam pointing instabilities mess up the interferometric position detection
Raw position signal from the interferometric detection of a 2 μm polystyrene bead trapped with the titanium-sapphire laser. In the time domain (left) distinct jumps due to beam position fluctuations are visible. The power spectral density of the particle's position (right) can hardly be described by a Lorentzian function.

Figure 2.15 A and B show two trouble shooting arrangements: The first one incorporates three mirrors, two pinholes and a beam profiler to manually account for beam pointing instabilities, which occur on the time scale of days. The two pinholes function as two reference points in order to reset position and angle of the beam in two dimensions. The second arrangement incorporates a fine pinhole (in the order of a micrometer) within a Galilean telescope to clean up the beam. A lens transforms the intensity distribution of an incoming beam into its Fourier spectrum at the focal plane. The diffraction limited spot of a TEM$_{00}$ Gaussian beam has a diameter (at the 99 % contour) of $D = \lambda \cdot f / r_{1/e^2}$, with wavelength λ, focal length of an aspheric lens f and beam radius r. Major parts of any deviation from this ideal distribution will be visible in side lobes in the spatial spectrum (see fig. 2.15 B, left upper panel). By placing a pinhole, which slightly exceeds the central spot into the focal plane of the first lens, the beam can be 'cleaned up'. A second lens collimates the beam again. Then the beam profile resembles a zero-order Gaussian beam.
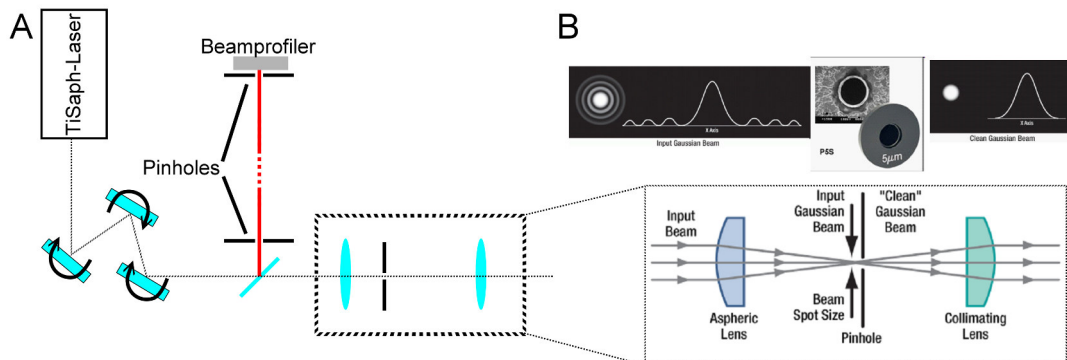
Figure 2.15: Beam steering and clean up optics for the titanium-sapphire laser
(A) Three mirrors, two pinholes and a beam profiler for position detection serve as a compensator for long term beam pointing fluctuations of the titanium-sapphire laser. **(B)** A laser beam is spatially filtered by placing a fine pinhole into the focal plane of a telescope. Adapted from [26]

Video-based microrheology | 3

Introduction to viscoelasticity and microrheology | 3.1

Investigating the mechanical properties of biological samples is about understanding its response to forces. In contrast to traditional fields in physics which measure the mechanical responses of solids one observes that biological materials are 'soft'. That means that these materials might behave somewhere within between the classical cases of a rigid solid and a viscous fluid.

Linear Viscoelasticity | 3.1.1

In shear experiments purely elastic solids store the applied energy when being deformed by a force (see fig. 3.1) and release it upon reversing the deformation. Its elasticity E is the constant relating shear stress σ to strain ϵ: $\sigma = E\epsilon$[1]. A purely viscous fluid starts to flow as a reaction to shear stresses. It is $\sigma(t) = \eta\dot{\epsilon}(t)$. All energy is dissipated by the fluid's internal friction. Viscoelastic materials can exhibit both parts of this behavior. In a viscoelastic material a single stress relaxation process is replaced by many possible ones. The Boltzmann super position principle leads to a general stress strain relation

$$\sigma(t) = \int_{-\infty}^{t} G(t - t')\epsilon(t)dt' \qquad \Leftrightarrow \qquad \sigma(\omega) = G(\omega)\epsilon(\omega)$$

which becomes a linear relation in frequency (since the integration limit in the left expression can be extended to infinity because $G(\Delta t) = 0$ there; then the integral becomes a convolution). $G(\omega)$ is the frequency dependent shear modulus. The real part is called storage modulus and contains the elastic in-phase response of the system, whereas the imaginary part contains the viscous response and is called loss modulus.

---

[1]A thorough theoretical treatment involves second order tensor fields of stress and strain. For simplicity of explanation the one dimensional case is shown here.

Since a viscoelastic material might have a broad distribution of timescales it is favorable to measure its response to stresses on different timescales.

$$\varepsilon = \delta \, / \, l = \tan \alpha \sim \alpha$$

$$\sigma = f \times A$$
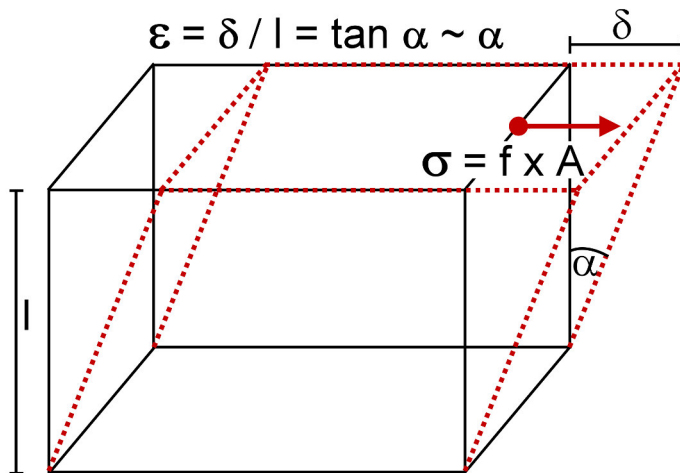
Figure 3.1: **Schematic drawing of a shear deformation**
A tangential force f on the top surface with area A causes a stress σ and a shear deformation of the volume element. The strain ϵ can be described by the shear angle α.

This is done by oscillatory measurements where a (superposition of) oscillating deformation at varying frequencies is applied to the sample and the amplitude and phase of its response is measured (see fig. 3.2).

3.1.2 | Microrheology

The standard experimental method in rheology is the use of a rheometer where a material of interest is placed between two moving plates to create a shear deformation similar to what is shown in figure 3.1. This has been a powerful method to measure rheological material properties for decades. However, biological samples turn out to be challenging regarding the following points: They have a rich dynamical behavior exhibiting different rheological responses on different timescales. Typical rheometers can measure shear moduli up to a few hundred Hertz, thus it is favorable to use techniques which can access higher frequency ranges.
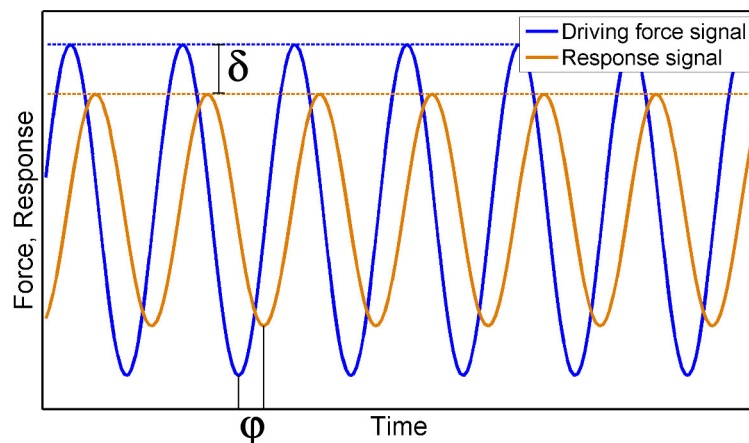
Figure 3.2: Oscillatory measurement
In oscillatory measurements the response of the system to a deformation is measured. Phase shift φ and change in amplitude δ are measured with respect to a sinusoidal driving force at a certain frequency.

Furthermore, it is often of interest to study small objects like cells which have an inhomogeneous structure. Thus, one wants to measure mechanical properties locally.

These requirements can be fulfilled by a technique called microrheology. Here one uses small probes which are dispersed in the sample to measure the shear modulus locally at the position of the probe. In active microrheology one exerts force onto the probe particle and at the same time records its response to it. Technically this can be realized for instance by an optical tweezer which can be oscillated at different frequency. After determining the position of the particle within the trap (e.g by an interferometric detection) one can measure amplitude and phase shift of the response just like as it is shown in figure 3.2. For the fly embryos studied in this work (see chapter 4) it turned out to be favorable to use a technically less demanding approach called passive microrheology.

Passive microrheology | 3.1.3

In passive microrheology one uses, in contrast to an externally driven force, the thermal noise with its well-known white noise spectrum caused by the collision with solvent molecules which push the probe particles. An important finding of statistical thermodynamics is the fluctuation dissipation theorem. It relates the thermal fluctuations of a system in equilibrium to its response to (externally) applied forces which put the system out of equilibrium. Already in 1905 when Einstein formulated his theoretical description of the Brownian motion of small particles in a fluid, he introduced the well-known equation $D = k_b T/\gamma$ (Boltzmann constant k_B, temperature T). This was already a form of the fluctuation dissipation theorem: It relates the diffusion constant D, a quantity which describes particle fluctuations, to the friction coefficient γ which determines the (macroscopic) dissipation in the system when exposed to a force.

A more general form of the fluctuation dissipation theorem is the following

$$Im\left(\chi(\omega)\right) = \frac{\omega}{2k_B T} Re\left[C^{AB}(\omega)\right] \tag{3.1}$$

where $C^{AB}(\omega) = \mathcal{F}\left[\langle B(0)A(t)\rangle_0\right]$, A and B are observable quantities of the thermodynamical system and $\langle\ \rangle_0$ is the equilibrium average. If both, A and B equal the position $x(t)$ of a particle (e.g. embedded in a complex fluid) then $C^{AB}(\omega) = |x(\omega)|^2$ becomes the power spectral density of the particle's position. Here again we find the dissipative part of the system's response to external perturbation $Im\left(\chi(\omega)\right)$ related to the equilibrium fluctuation of it.

The linear response function χ for a time-invariant system is defined by

$$x(t) = \int \chi(t,t')f(t')dt' \qquad \text{with} \qquad \chi(t,t') = \begin{cases} \chi(t-t') & \text{for} \qquad t > t' \\ 0 & \text{otherwise} \end{cases}$$

Time-invariance of the system implies the first line and causality the second. This leads to a linear relation in frequency space

$$x(t) = \int_{-\infty}^{t} \chi(t-t')f(t')dt' \qquad \Leftrightarrow \qquad x(\omega) = \chi(\omega) \cdot f(\omega)$$

$x(t)$ is an observable, e.g. the particle's position and f the force acting on the system.

χ is a causal function ($\chi(t) = 0$ for $t < 0$) and thus fulfills the requirement for a Kramers-Kronig relation which relates the real and imaginary part of the response function $\chi(\omega) = \chi'(\omega) + i\chi''(\omega)$ in the following way

$$\chi'(\omega) = \frac{1}{\pi}\mathcal{P}\int_{-\infty}^{\infty} \frac{\chi''(\omega')x}{\omega'^2 - \omega^2}d\omega' \qquad (3.2)$$

where P denotes the Cauchy principal value[2]. The response function can be completed by that, provided that $\chi''(\omega)$ is known over a large enough frequency range.

A particle embedded into a viscoelastic medium and exposed to a force f will induce a stress field $\sigma \propto f$. This field is related to a strain field $\epsilon \propto x$ which is proportional to the displacement x of the bead. For a combined shear and compressional deformation of a small volume element stress σ_{ij} and strain ϵ_{ij} are related by $\sigma_{ij} = 2G\left[\epsilon_{ij} + \delta_{ij}\sum_k \nu/\left(1-2\nu\right) \cdot \epsilon_{kk}\right]$. G is the shear modulus (at zero frequency $\omega \to 0$) and ν is the Poisson ratio.

A model for a typical experimental geometry in microrheology is a bead embedded in an incompressible ($\nu = 1/2$) polymer network of unknown viscoelasticity. The assumption of incompressibility is valid above a certain crossover frequency, when the motion of the network strongly couples by viscous drag force to the surrounding solvent. Below this transition a two fluid model has to be applied, where compressional deformation of the network is possible. One can apply a continuum model for the surrounding medium if the bead diameter exceeds the mesh size of the network [27]. Then elastic equilibrium $\partial\sigma_{ij}/\partial x_i = 0$ and no-slip boundary conditions at the rigid spherical surface of the bead lead to a generalized Stokes relation for the compliance and response function χ

$$x(\omega) = \chi(\omega) \cdot f(\omega) = \frac{1}{6\pi R \cdot G(\omega)} \cdot f(\omega) \qquad (3.3)$$

With this in hand one has the toolbox to determine the shear modulus locally, inside a complex fluid

---

[2]This means the singularity at $\omega = 0$ is approached in the integration process from left ($\omega - \epsilon$) and right ($\omega + \epsilon$) for the limit of $\omega \longrightarrow 0$.

Principles and data processing in video-based microrheology | 3.2

Video-based microrheology uses a video microscope to record the magnified images of tracer particles. In a second step the position of these particles is determined and the analysis is done according to the principles described in the previous section. The advantage of video-based microrheology is its technical simplicity. In contrast to microrheology with optical or magnetic tweezers one just needs a microscope in order to image the sample. Furthermore, one is independent of a sensitive detection path as needed for interferometric detection typically used with optical traps. Strongly scattering, thick samples with optical inhomogeneities disturb the detection or make it impossible. Moreover, the calibration of the position signal is easy. One can directly deduce it by measuring the magnification of the microscope and pixel distance on the camera chip.

Position tracking | 3.2.1

For video-based microrheology one needs to determine the position of the tracer particles and link the position trajectories in the different frames to a trajectory. In this work a feature finding and tracking algorithm is used which was kindly provided by Maria Kilfoil and her group. It is implemented as a Matlab code (MathWorks, Natick, MA, USA) and was first applied and described in [28].

The algorithms are based on the work of Crocker and Grier [29]: Features of interest are recognized by identifying all pixels above a user-defined threshold. Then a mask of a certain radius w is centered onto these possible candidates (x^p, y^p), $p = 1 \cdots N$, N: number of particles, to determine the center of mass, i.e. the first moment of the intensity distribution within this mask:

$$\begin{pmatrix} \epsilon_x \\ \epsilon_x \end{pmatrix} = \frac{1}{m_0} \sum_{i^2+j^2 \leq w^2} \begin{pmatrix} i \\ j \end{pmatrix} \cdot \text{Intensity}(x + i, y + j)$$

$$\text{with total intensity:} \ \ m_0 = \sum_{i^2+j^2 \leq w^2} \text{Intensity}$$

That way the center of mass $(x_0, y_0) = (x + \epsilon_x, y + \epsilon_y)$ can be determined for each particle (see fig. 3.3). Possible candidates can be rejected if they do not fall into a specified parameter window regarding minimum and mean intensity, eccentricity and second moment of intensity.

In the following step locations are linked into trajectories by finding the most probable set of connections between particles in two consecutive frames.
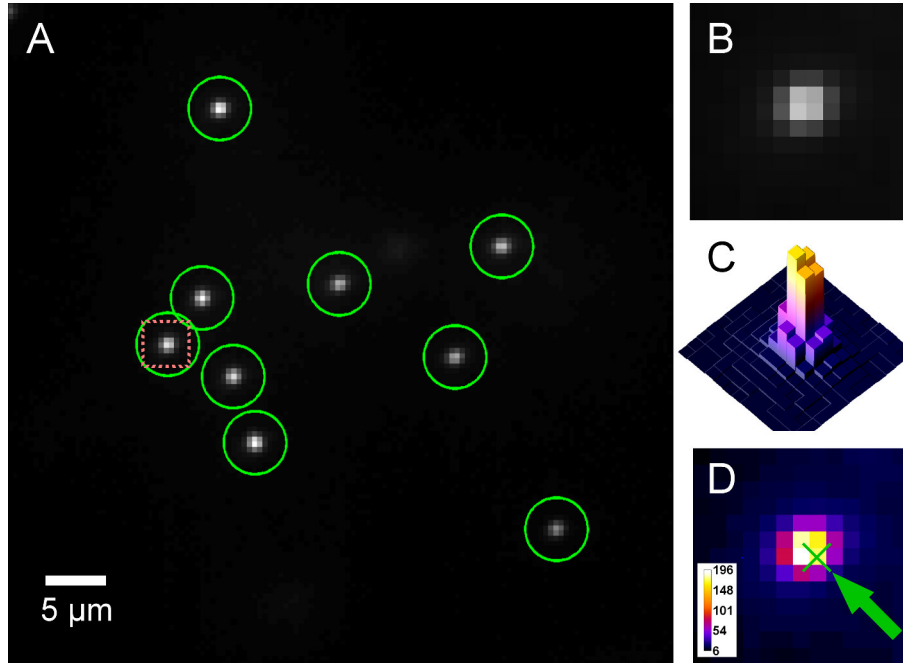
Figure 3.3: **Feature finding algorithm and centroid estimator applied on fluorescing bead images**
(A) Image of fluorescing beads with green circles indicating the objects are recognized by the feature finding algorithm. **(B)** Magnified image of the bead marked by the dotted box in the left image. **(C)** 3D intensity map of the indicated bead. **(D)** Image of the indicated bead (with a 'fire' LUT) and its estimated center shown by the cross and arrow.

The probability for a Brownian particle diffusing a distance of δ during time τ is $P(\delta|\tau) = 1/(4\pi D\tau) \cdot \exp(-\delta^2/4D\tau)$ with D the particle's diffusion constant. Thus, for N non-interacting particles the probability $P(\{\delta_i\}|\tau) = P(\delta|\tau)^N$ has to be maximized:

$$\text{maximize } P(\{\delta_i\}|\tau) = \left(\frac{1}{4\pi D\tau}\right)^N exp\left(-\sum_{i=1}^{N}\frac{\delta_i^2}{4D\tau}\right) \quad \Rightarrow \quad \text{minimize } \sum_{i=1}^{N}\delta_i^2$$

Additionally a maximum possible displacement, a minimum trajectory length and a maximum number of frames where particles are not visible can be specified for reducing computational effort and further discrimination of useful trajectories. Figure 3.4 shows the result of the tracking algorithm for two control samples recorded at different frame rates.

A custom-written Matlab script lists detection gaps and suggests a better set of feature finding parameters[3]. A list of custom-written Matlab scripts and their short descriptions for the purpose of video-based microrheology and particularly this work can be found in the appendix.

The bead trajectories were then extracted by a custom-written Matlab script[4] from the feature finding and tracking algorithms of the Kilfoil group in order to analyze them in the way described in section 3.1.3[5].

---

[3]See Matlab function description for *'find_detection_gaps'* in the appendix.

[4]See Matlab function description for *'VMR_analysis'* in the appendix.

[5]There is a second way to extract mechanical material properties of the particle's surrounding medium out of their position trajectories. This way was introduced by Mason and Weitz [30] and is implemented in the Kilfoil algorithm.
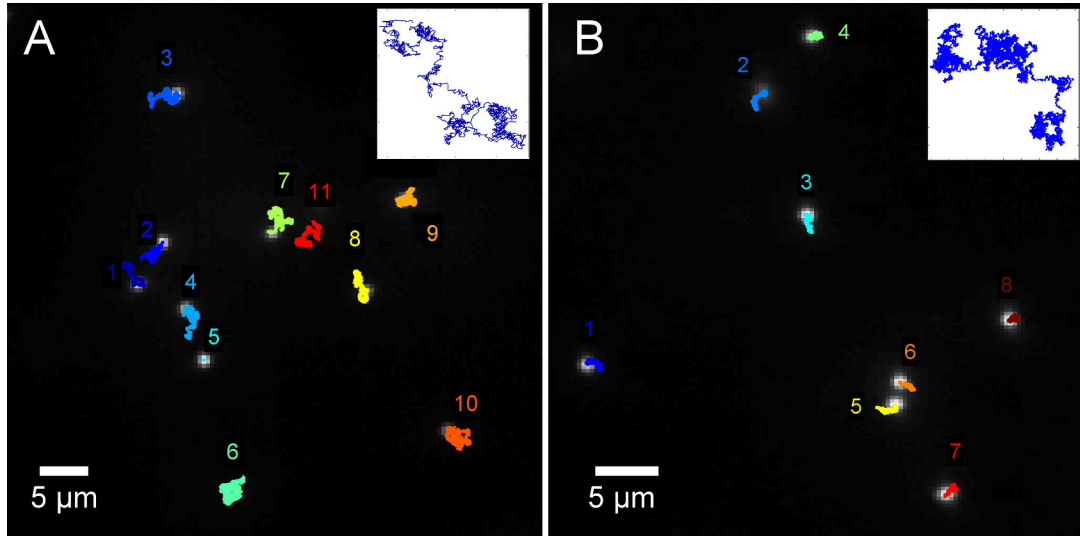
Figure 3.4: Position trajectories of fluorescing microspheres
(A) Motion trajectories of the fluorescing beads shown in figure 3.3 determined by the tracking routine described in the text. Frames were recorded at a rate of 20 Hz for 118 seconds. Inset: Trajectory of bead 1 with a box size of 1390 nm. **(B)** Motion trajectories of fluorescent beads imaged with the high-speed camera at a frame rate of 8 kHz for 23 seconds. Inset: Magnified trajectory of bead 1 with a box size of 2868 nm. Both samples were 1 μm beads dispersed in a glycerol/ water mixture (70 % glycerol).

## Calculation and processing of the power spectral density | 3.2.2

The calculation of the power spectral density of the particle's position trajectories is based on methods described in the book *Numerical recipes in C* by W. Press [24] and the report *Signals and Noise in Micromechanical Measurements* [25] and was implemented by F. Zoergiebel as a part of a collection of Matlab scripts called *Microrheology Toolbox* (detailed description in [31]).

Calculation of the power spectral density

In order to apply the fluctuation dissipation theorem (equation 3.1) the power spectral density (PSD) needs to be calculated. According to the Wiener Khinchin theorem the PSD is the Fourier transform of the autocorrelation function. For this work the PSD= $|x(f)|^2$ was calculated directly by multiplying the discrete Fourier transforms of the signal [25]:

$$|x(f)|^2 = \frac{1}{T} \, x(f) \cdot x^*(f_k) \qquad \text{with} \qquad x(f_k) = \sum_{l=1}^{N} x_k \, exp\,(2\pi i/Nkl)$$

where N is the number of data points and T the measurement time. The Fourier transforms were calculated by the standard Matlab Fast Fourier Transform function. Beforehand a 'tukey' window function was multiplied with the signal to minimize artifacts caused by a finite measuring time on a non-stationary signal. Figure 3.5
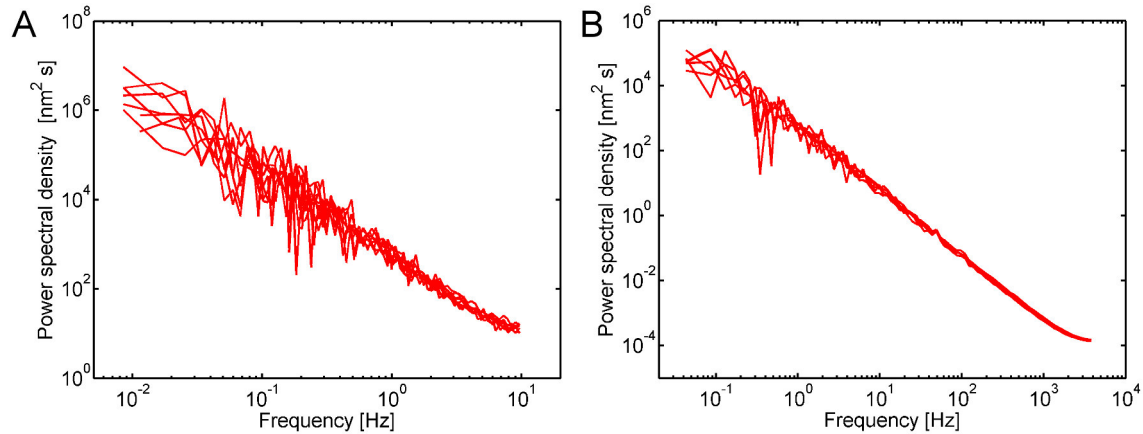
Figure 3.5: Exemplary power spectral densities of a freely diffusing microsphere
(A) PSD calculated from the trajectories shown in figure 3.4 A. **(B)** PSD calculated from the trajectories shown in figure 3.4 B. All curves were logarithmically binned with 100 bins.

shows exemplary PSD which were logarithmically binned [6] and measured in a control sample.

For measuring two particle correlation spectra $|x(f)|^2$ becomes

$$C_{a,b} = 1/T \cdot x^a(f) \cdot \left(x^b(f)\right)^*$$

(3.4)

with a and b indicating signals of the two different particles.

Artifacts of shot noise and mechanical noise

Video-based microrheology turned out to be very sensitive to two main noise sources: The first noise source is shot noise. As can be seen in figure 2.5 the signal intensity of a fluorescent bead decreases linearly with frame rate, i.e. exposure time. Measurements were typically taken at 8 or 16 kHz. Due to the discrete nature of photons the arrival and recognition of a photon on the camera chip becomes a stochastic process following Poisson statistics. At too low light intensities the randomness of where and when a photon arrives becomes large compared to the average number of photons. This effect causes apparent random fluctuations of the particle which exceed the actual signal of the real position fluctuations and add to the noise floor. Since the PSDs of the particle fluctuations in this work follow power laws with a negative exponent, these effect can only be seen at the high-frequency edge of the sampled range. Figure 3.6 illustrates the effect of a too weak illumination intensity making the PSD run into a plateau-like off-leveling. The same effect can also be caused by defocusing. The amount of light which is collected by an objective lens strongly depends on the distance of the particle to the focal plane. Hence, the signal of defocused particles also suffers on shot noise.

The second noise source is mechanical noise. As soon as it causes relative fluctuations of the probe particles to the detection system mechanical noise will become

---

[6]See figure 3.10 for further explanation.
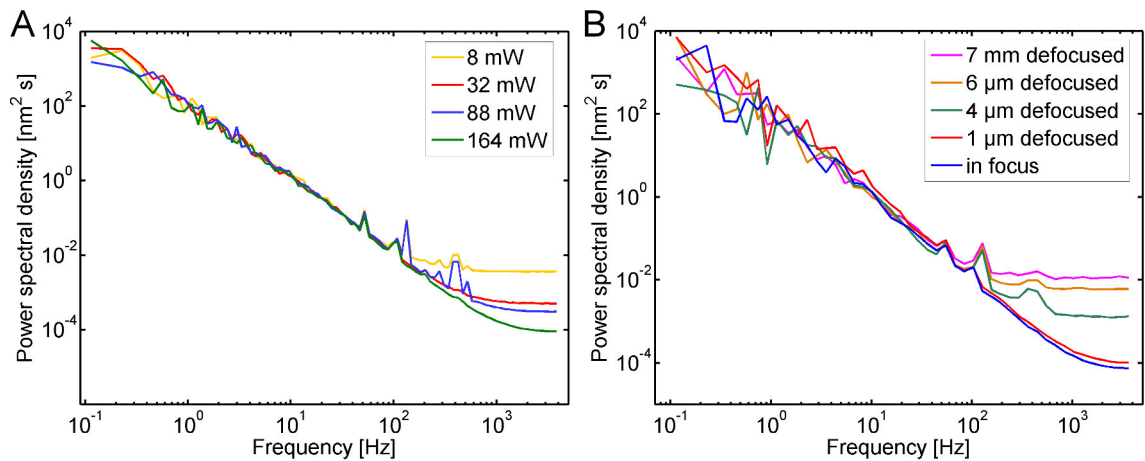
Figure 3.6: **Effect of different excitation intensities and defocusing on the power spectral density**
Power spectral density curves and its off-leveling behavior for **(A)** different excitation intensities (at the sample plane) and **(B)** different distances of the particles to the focal plane. Both samples were 1 μm beads dispersed in a glycerol/ water mixture (90 % glycerol).
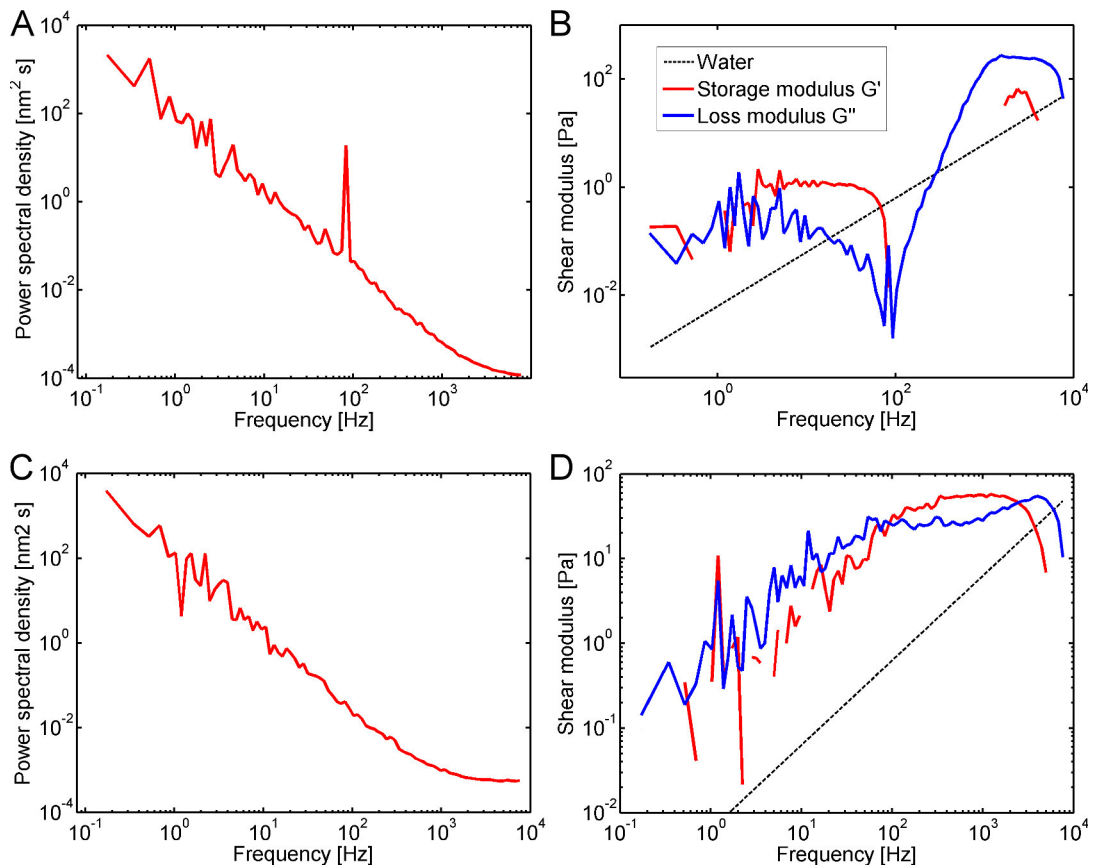
Figure 3.7: **Effect of noise on the power spectral density and the corresponding shear module curves**
**(A)** PSD curve exhibiting a peak at 100 Hz due to mechanical vibration. **(B)** Corresponding shear modulus exhibiting artifacts due to the noise peak. **(C)** PSD curve exhibiting an off-leveling at frequencies higher than 2000 Hz due to shot noise. **D** Corresponding shear modulus shows artifacts due to the off-leveling behavior of the PSD curve.

visible in the PSD. Figure 3.7 shows two kinds of noises being visible in the PSD and illustrates their effect on the obtained shear modulus.

Since the whole setup is mounted on a damped optical table perturbations caused by building/ ground vibrations can be neglected. Cooling fans and the water cooling system of the electronic equipment turned out to be the dominant noise sources. For the measurements the water cooling system and all camera fans were switched off. By that most of the noise sources could be eliminated. Nevertheless, there were still some noise peaks from time to time present probably caused by the computer cooling fan which was transmitted by the signal cables to the optical table.

Correction for noise artifacts

In order to avoid artifacts of noise described in the previous section propagating into the measured shear moduli the PSD curves were manually processed. Figure 3.8 shows the two processing steps which were optionally applied to the PSD curves: Firstly, distinct noise peaks were filtered, by interpolating a manually defined region which includes the noise peak. The interpolation was done by fitting a power law function to the data points in a certain range around the interpolation area. Since the fitting procedure is based on a χ^2 minimization approach, the data first had to be linearly averaged over blocks of a certain number of data points. This ensures by the central limit theorem a Gaussian data distribution at a certain small frequency band [32]. In general PSD data follow a logarithmic distribution.
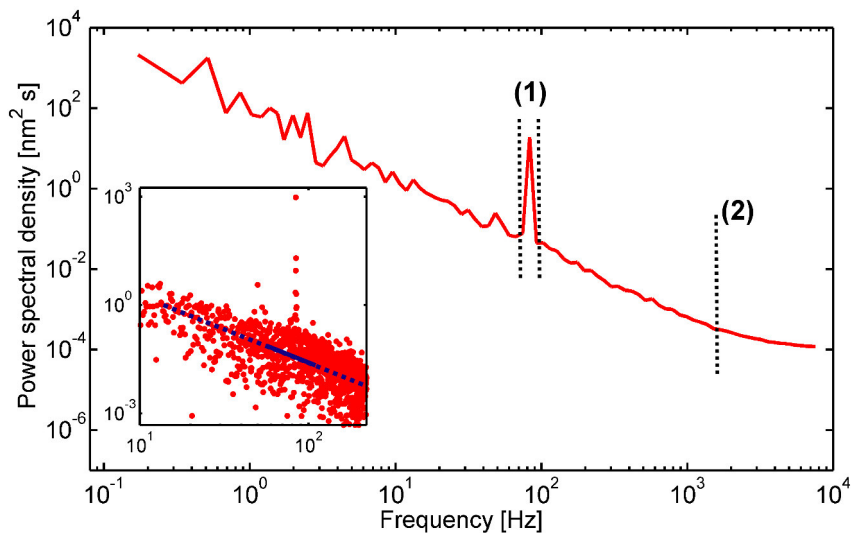
Figure 3.8: Processing of the power spectral density curves
The graph shows a power spectral density curve exhibiting a noise peak and an off-leveling of the signal at high frequencies. The dashed lines indicate where the curve was interpolated (1) and truncated (2). The inset displays a part of the same curve with a hundred times higher number of bins in order to show the distinct character of the noise peak. Data was interpolated by fitting a power law curve in the vicinity of the peak (solid blue line).

Secondly, the curves were truncated at the high-frequency end if an off-leveling behavior became visible.

As introduced in section 3.1.3 the calculation of the shear modulus is based on the work by Schnurr et al. [27] and was numerically implemented by Felix Zörgiebel [31].

Calculation of the shear modulus

As a first step the fluctuation dissipation theorem (see equation 3.1) is applied in order to obtain the shear modulus from the PSD of the probe particle's position fluctuations. Numerically this is a simple vector multiplication. In a second step
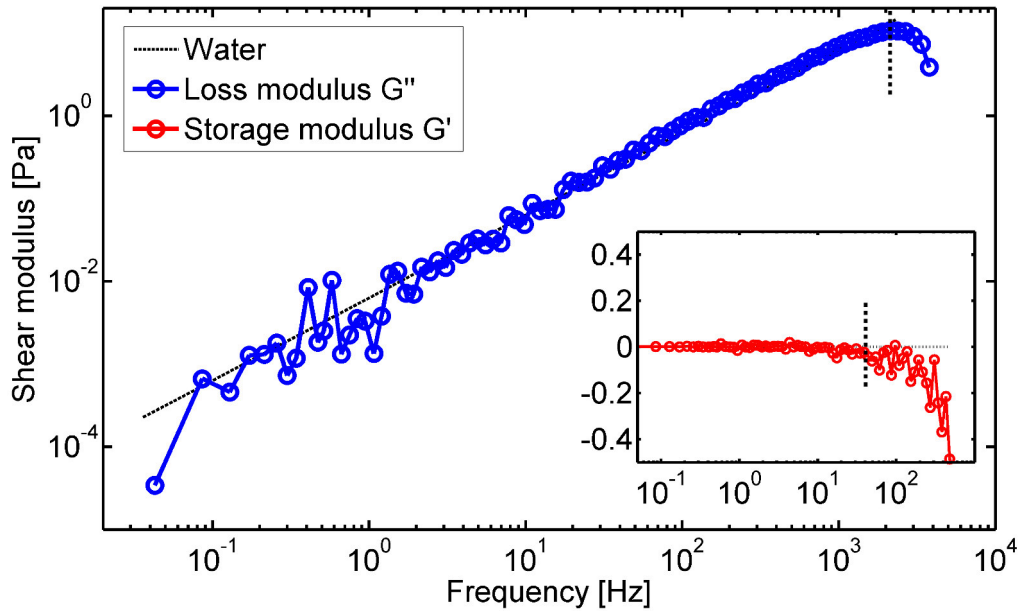
Figure 3.9: Exemplary shear modulus curve of a freely diffusing bead
The graph shows the viscous loss modulus and the elastic storage modulus (inset) of a freely diffusing bead in water. The dashed lines indicate a typical cutoff position where a truncation is performed manually to account for the artifact of a dropping module caused by the Kramers-Kronig integration (as described in the text).

the complex response function $\chi(\omega)$ is completed by deducing its real part from its imaginary part by a Kramers-Kronig relation (see equation 3.2). Numerically this calculation is performed by the convolution method[7]

---

[7]Any causal function $\chi(t)$ can be constructed by $\chi(t) = sign(t) \times \chi_{odd}(t) + \chi_{odd}(t)$. $\chi_{odd}(t)$ is the odd part of χ. The first summand is the even part of χ, therefore its Fourier transform will be real whereas $\mathcal{F}[\chi_{odd}(t)] = Im(\chi)$ will be purely imaginary. Thus, it is $Re(\chi(\omega)) = \mathcal{F}[sign(t) \times \mathcal{F}^{-1}[\chi''(\omega)]]$. Per definition $\chi''(\omega)$ is real and odd. So the second factor becomes a sine transform. The whole expression in brackets is even and real, hence $\mathcal{F}[...]$ becomes a cosine transform. We finally obtain $Re(\chi(\omega)) = \frac{2}{\pi} \int dx \, cos(2\pi x\omega) \int d\omega' \, sin(-2\pi x\omega') \, \chi''(\omega)$ which is the continuous form of the expression in the main text.

$$Re\left(\chi_l\right) = \frac{2}{n+1} \sum_{p,q,k} C_{lp}{\cdot}D_{pq}{\cdot}S_{qk}{\cdot}Im\left(\chi_k\right) \qquad \text{with} \qquad D_{kl} = \begin{cases} 0 & \text{for} & k=0 \\ \delta_{kl} & & \text{otherwise} \end{cases}$$

where C_{lp} and S_{qk} are the cosine and sine transform matrix, respectively. The finite integration range in the Kramers-Kronig relation leads to deviations at the edges of the response function curves (see [27] for details). These deviations propagate as an artifact into the shear modulus curves (see fig. 3.9). That is why shear moduli were truncated manually at the indicated dashed lines for averaging and displaying it. The transition from the response function to the shear modulus is done by the generalized Stokes Einstein equation (see equation 3.3). This leads to the elastic shear modulus $G'(\omega)$ and the viscous shear modulus $G''(\omega)$:

$$G'(\omega) = \frac{1}{6\pi R}\frac{\chi'(\omega)}{\chi'(\omega)^2 + \chi''(\omega)^2} \quad \text{and} \quad G''(\omega) = \frac{1}{6\pi R}\frac{-\chi''(\omega)}{\chi'(\omega)^2 + \chi''(\omega)^2}$$

Averaging shear module curves

For analyzing and displaying data it is favorable to average shear moduli of different experiments together and display the average over logarithmically spaced frequencies. In video-based microrheology particles can diffuse out of focus. Thus, the
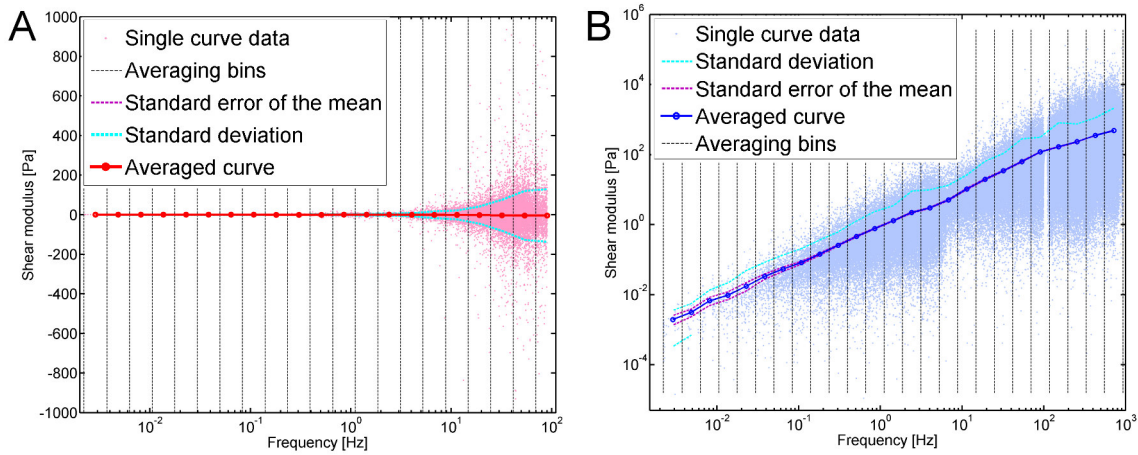
Figure 3.10: Averaging shear moduli curves
(A) Point cloud of many single storage moduli with its average curve obtained by logarithmical binning. Dashed lines show standard deviation (SD) and standard error of the mean (SEM). **(B)** Point cloud of many single loss moduli with its average curve obtained by logarithmical binning. Dashed lines show SD and SEM. Curves were recorded in a water/ glycerol mixture where the elastic modulus is expected to be zero.

number of data points, and hence the frequency spacing and lower frequency bound of the shear moduli differ. The truncation procedure described above leads to varying upper frequency bounds of the shear moduli.

Thus, the most robust way to bin the data is to set up the following frequency grid for averaging (Matlab code)[8]:

```
FreqGrid=
exp(log(MinFreq):((log(MaxFreq)-log(MinFreq))/Nlog):log(MaxFreq))
```

with the smallest occurring frequency of the dataset `MinFreq`, the largest occurring frequency in the dataset `MaxFreq` and the number of bins `Nlog`. Figure 3.10 shows an example of many shear modulus curves being averaged over the indicated frequency grid.

---

[8]See Matlab function description *'average_G1PMR'* in the appendix.

3.3 | **Control measurement**

By this work video-based microrheology was introduced to our lab. In order to confirm the proper functioning of this method a control experiment was performed.

3.3.1 | **Surface attached microspheres**

In order to quantify tracking performance, fluorescent particles, as used in later experiments, were immobilized on a surface by drying a drop of particle solution followed by covering it with an agarose gel. Subsequent tracking reveals the RMS
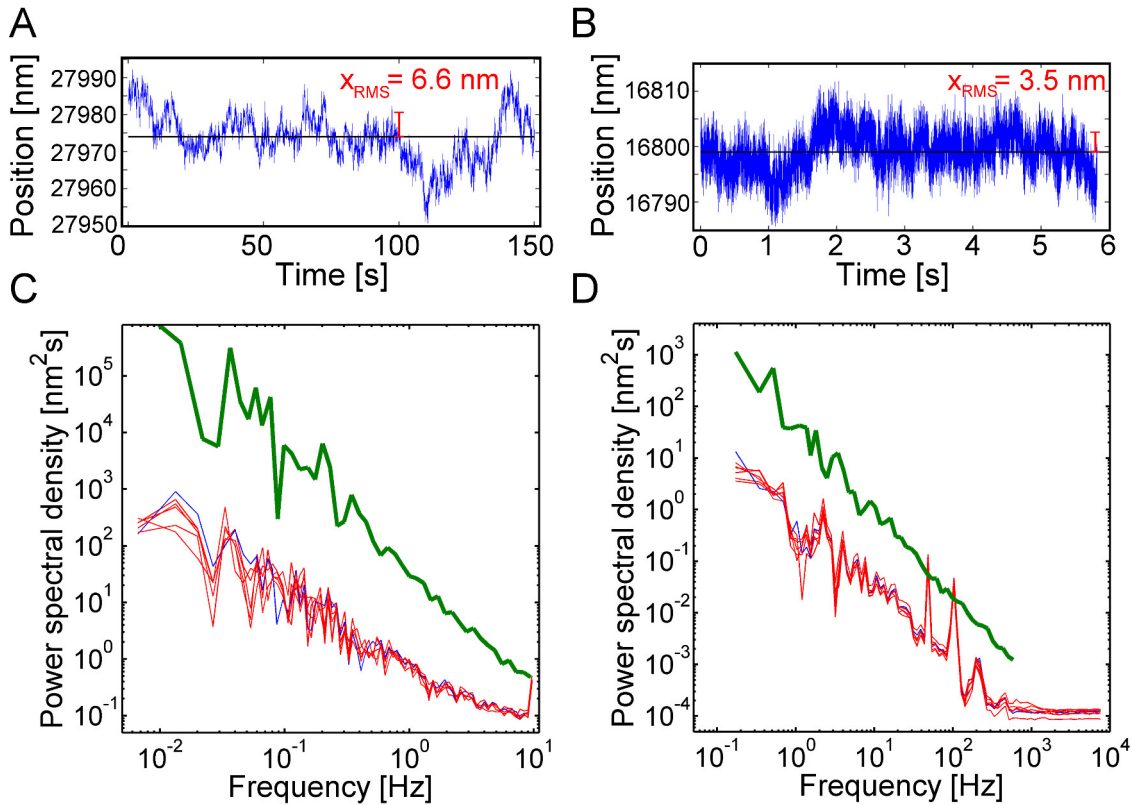
Figure 3.11: Tracked position and power spectral densities for surface-attached beads
(A) and **(B)** display the tracked position of a bead over time attached to the surface and embedded in a 2 % agarose gel, recorded at 20 Hz and 16 kHz, respectively. The RMS noise is shown in red and is 6.6 nm and 3.5 nm, respectively, for these datasets. **(C)** and **(D)** show power spectral densities of beads recorded at 20 Hz and 16 kHz, respectively. The blue curves correspond to the trajectories in the upper graphs. The green curve shows an exemplary dataset measured within the nuclear layer of a *Drosophila* embryo.

noise $\varepsilon = \sqrt{\langle x^2 \rangle - \langle x \rangle^2}$, i.e. tracking accuracy (see fig. 3.11). An average over seven beads gives RMS values of 11.9 nm $\pm$ 1.8 nm for the low-speed channel and 3.7 nm $\pm$ 0.1 nm for the high-speed channel (mean $\pm$ SEM). The corresponding PSDs show the noise floor of the system which is about three to four orders of magnitude below a typical signal taken inside a *Drosophila* embryo (see fig. 4.8).

To proof that the described video-based microrheology analysis gives the right re-
sults the viscosity of a well-characterized Newtonian fluid was measured, a glycerol
water mixture. A freely diffusing bead in a purely viscous fluid obeys the simple
Langevin equation $\gamma dx/dt = \zeta(t)$ (see also equation 2.1) which leads to a PSD
$S(f) = k_B T/(\gamma \pi^2 f^2)$. This explains the power law behavior with a slope of -2 of
a freely diffusing bead in a viscous fluid. For a simple shear flow the stress strain
relation is

$$\sigma(t) = \eta \dot{\epsilon} \qquad \Leftrightarrow \qquad G(\omega) = i\omega \eta$$

where η is the dynamic viscosity. Thus, we expect a linear scaling of the viscous
loss modulus $Im\left(G(f)\right) = 2\pi \eta f$ with frequency.

By mixing water with glycerol with different volume fractions one obtains a New-
tonian viscous fluid with varying viscosity. The viscosity of such a mixture depends
non-linearly on glycerol concentration and was empirically determined in [33]. By
this the viscous modulus was calculated for three different solutions: 90 % glycerol,
70 % glycerol and 0 % glycerol, i.e. pure water. These three control samples were
measured with the video-based microrheology method described in the previous sec-
tion. The samples containing glycerol were additionally measured with a cone plate
rheometer (MCR 501 Rheometer, Anton Paar, Graz, Austria). Figure 3.12 shows
the results of this control measurement.

The first graphs show the single bead data and its averaged curve. The array
of single bead curves gives an estimate of the dynamic measuring accuracy. Qual-
itatively one can see that for low frequencies the curves scatter more around the
average. That makes sense since for higher frequencies more oscillations were sam-
pled. Besides the tracking accuracy the actual bead size deviating from the average
diameter introduce some error. The microsphere stock solution always has a poly
disperse size distribution.

The rheometer could measure the rather soft sample only in the frequency range
of 0.1 to 20 Hz (90 % glycerol) and 0.1 to 4 Hz (70 % glycerol). For comparison
with the microrheology experiment the rheometer data was fit with a power law and
interpolated to an extended frequency range. Figure 3.12 G shows the comparison
of the microrheology measurement with the rheometer data and the theoretical pre-
dictions. For each sample one can see a good agreement of all three curves in terms
of magnitude of the viscous shear modulus as well as its scaling with frequency to
the power of one. As expected the elastic modulus scatters around zero (panels A,
C ,E).
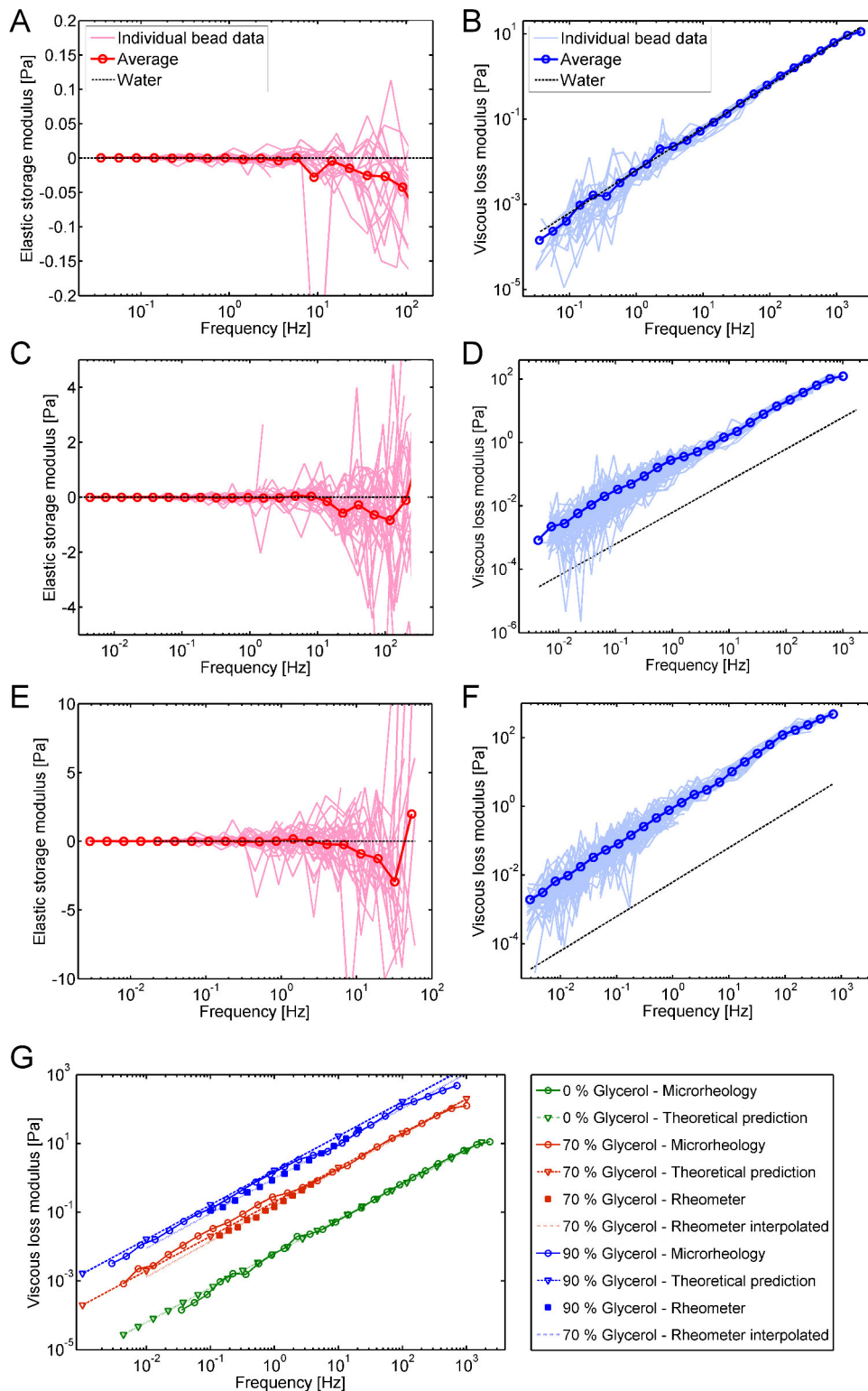
Figure 3.12: Shear moduli of beads in a water/glycerol mixtures
(A) The elastic storage moduli of several beads dispersed in pure water (0 % glycerol) and its average curve. The dashed line shows the theoretical prediction for water. **(B)** Viscous loss modulus for the 0 % glycerol sample. **(C)** and **(D)** Storage and loss modulus for a glycerol/water mixture of 70/30. **(E)** and **(F)** Storage and loss modulus for a glycerol/water mixture of 90/10. **(G)** Average loss moduli of the upper graphs for different glycerol/water mixtures (circles). The triangle curves are theoretical predictions for the respective glycerol/water mixtures as described in the text. The square symbols show measurements on the same samples with a rheometer. The dashed lines show an interpolation of the rheometer data.

High-speed video microrheology inside syncytial *Drosophila* embryos | 4

In early development, *Drosophila melanogaster* embryos form a syncytium, i.e. multiplying nuclei are not yet separated by cell membranes, but are interconnected by cytoskeletal polymer networks consisting of actin and microtubules. This distribution of filaments makes the syncytial embryo an interesting system to study the mechanical properties of in-vivo networks. Particularly because the interior of the embryo is comparably easy to access and long-range measurements can be performed. In the syncytial stage, nuclei and cytoskeleton form a 2D cortical layer. These developing embryos presents a striking example of complex biological self-organization and dynamic formation of patterns and structure. To probe the mechanical properties and dynamics of this self-organizing "pre-tissue", shear moduli were measured within the living embryo by high-speed video microrheology.

Introduction to early *Drosophila melanogaster* embryos | 4.1

Drosophila melanogaster is a well-established model system to study embryonal development, since it is transparent, rapidly developing and has still a small number of cells. It is of particular interest to understand how tissue grows and maintains a well structured pattern during this development.

In its early developmental stages the embryos develop as a syncytium, i.e. nuclear division happens without cytokinesis inside a common cytoplasm. After the 9th nuclear division cycle most of the nuclei migrate from the interior of the embryo to the cortex and form a two dimensional layer which shows a hexagonal structure, just like many epithelial tissues [8, 9, 34]. The center of the embryo consist of an ellipsoidal kernel of yolk, containing yolk granules and vitellophages. After migration the syncytial stage lasts for another four nuclear divisions which occur in a wave-like manner starting at the poles of the embryo and traveling through it [9]. Each of these divisions disturb the hexagonal pattern and after each division the pattern is reestablished by a self-organized process before the cellularization finally separates the nuclei into individual cells [35]. The cortical layer of nuclei exhibits a symmetric pattern even without the contribution of surface tension according to cellular surfaces and can thus be considered as a simple 'pre-tissue'. It grows under confinement to a plane and to the constant area of the tough egg shell. Inside the two-dimensional layer the nuclei are not yet separated by any membrane but interact

via an embedding cytoskeleton consisting largely of microtubules and actin. There are no intermediate filaments in Drosophila. Actin builds up a cortical layer and forms actin caps which are located between the nuclei and the egg membrane (see fig. 4.1 and 4.2).
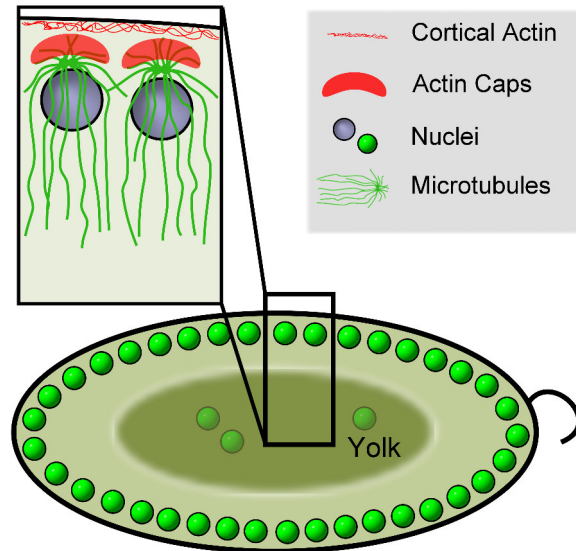

Figure 4.1: Schematic drawing of the embryo
Schematic drawing of the syncytial blastoderm. The nuclei form a cortical ellipsoidal layer. The inset shows the cortical organization of nuclei, microtubules and f-actin.

Microtubules, originating from the centrosomes form basket-like structures which enclose the nuclei. Astral microtubules point from the centrosomes towards the cortex and overlap with astral microtubules of neighboring nuclei [36–41]. Former studies have shown that the nuclei do not directly structure the cytoskeletal networks whereas the centrosomes seem to be the main organizers of the networks [42]. During mitosis the microtubules transform to mitotic spindles and actin accumulates at the metaphase furrows which separate the spindles [43].

The nuclear layer shows large-scale collective dynamics, for example density waves traveling through the layer during synchronized mitosis. Recent studies modeled the mitotic waves and showed that the characteristics of metasynchronous division of nuclei can only be explained assuming a mechanically transmitted communication between the nuclei. The authors stated a clear need of absolute numbers regarding the viscoelastic properties of the medium surrounding the nuclei [44].

Another work investigating the dynamic ordering of the nuclei has shown that mechanical interactions of the nuclei are necessary to obtain the observed pattern formation, pointing out that microtubules and actin play a key role in passive as well as active positioning. Furthermore, it has been shown that the disarrangement in the nuclear layer stems primarily from the active elongation of the mitotic spindle [45]. Other sources of active force generation in interphase were suggested, for example the action of kinesin-5 motors between overlapping microtubules, a direct active interaction of astral microtubules with nuclei or an active interaction of microtubules with the actin caps by dynein-dynactin complexes [46, 47].
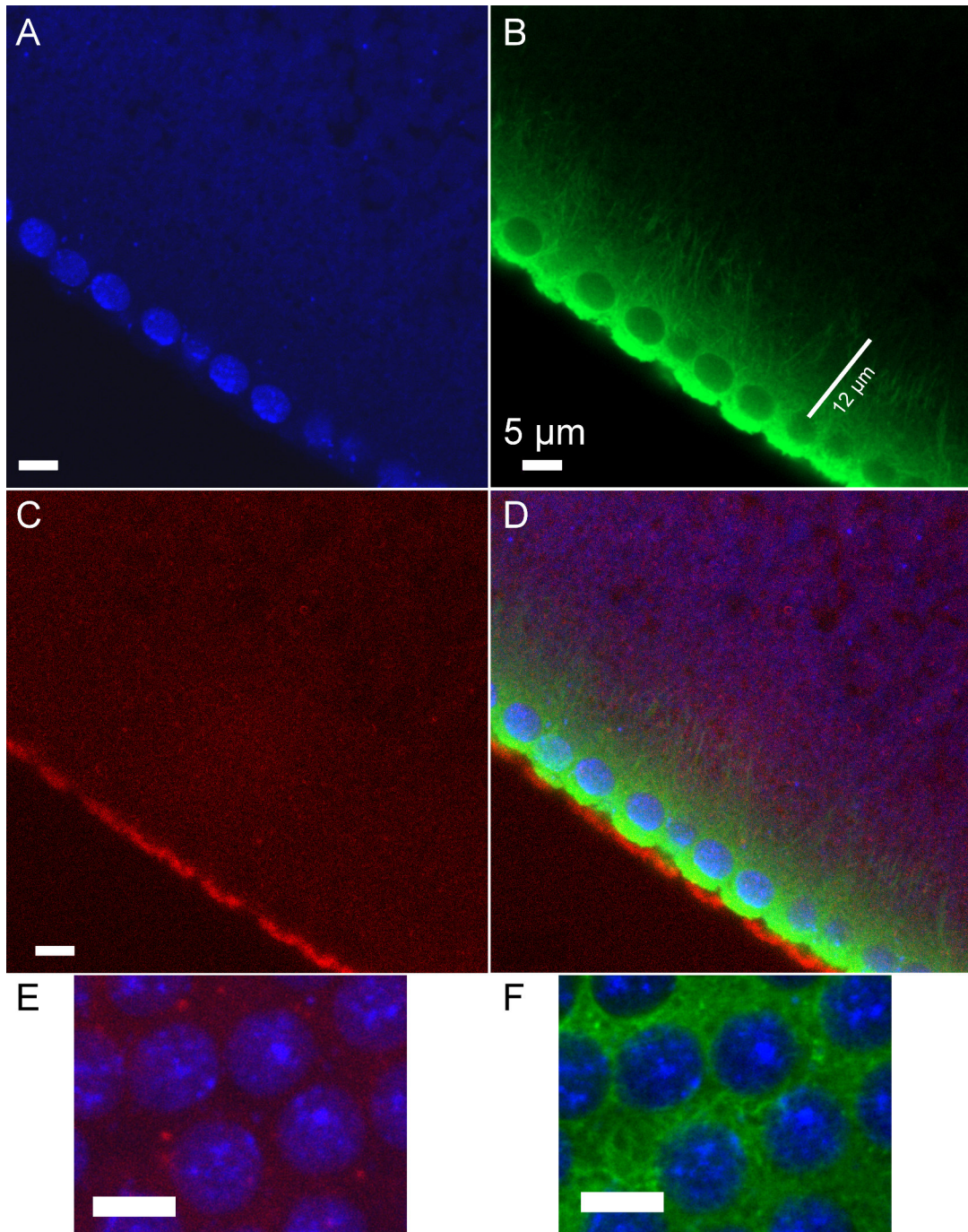
Figure 4.2: **Confocal images of the cytoskeletal distribution inside early Drosophila embryos**

Confocal fluorescence images of fixed embryos showing nuclei **(A)**, microtubules **(B)**, actin **(C)** and the merged channel **(D)**. Images were taken ~ 22 μm above the coverslip and show a view onto the edge of the embryo. Microtubules form a dense network between nuclear layer and cortex. From the nuclear layer towards the yolk the microtubule network becomes thinner so that single filaments can be resolved. From the nuclear layer microtubules reach $\sim 12 \mu m$ deep into the interior of the embryo. **(E)** Distribution of nuclei and microtubules within the nuclear layer. **(F)** Distribution of nuclei and actin within the nuclear layer. There is no actin present within the nuclear layer, whereas microtubules form a network between the nuclei. Chemically fixed and stained embryos[1] were imaged with a confocal microscope (SP5, Leica Microsystems, Wetzlar, Germany).
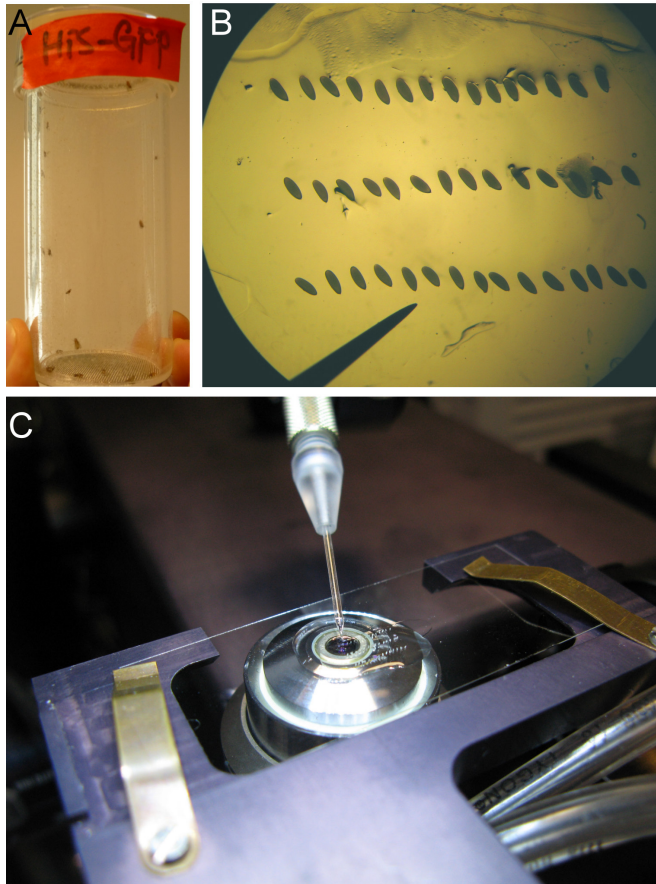
[1]For details regarding the immunostaining preparation procedure see section *Lab protocols and methods* in the appendix.

In order to obtain *Drosophila* embryos, flies were grown in a plastic cage (figure 4.3 A), fed with standard baker's yeast. Petri dishes containing a mixture of agar and apple juice were used to collect the embryos. Developing embryos were dechorionated by washing them with standard bleach and then aligned under a stereo microscope (see fig. 4.3 B) and glued to a coverslip. After dessication and covering with oil, 1 μm diameter, carboxylated, crimson fluorescent beads were pressure-injected with a standard micro-injector using custom-pulled capillaries (see fig. 4.3 C). Beads were injected into the embryo before the formation of the nuclear layer perpendicularly to the long axis straight down towards the substrate approximately 3-6 μm above the surface of the coverslip (see fig. 4.4 A). Imaging was performed after the nuclear layer had formed. Different genetically modified fly strains were used expressing different fluorescing structures: Nuclei, microtubules or actin. Optionally, chemical agents were injected at the posterior end of the syncytial embryo: Colcemid, latrunculin A and rho kinase inhibitor Y-27632. For the vertical injection custom pulled injection needles with a long, uniform and steady tapper (see fig. 4.4 B) opened at the tip by breakage were used to disturb the embryo as less as possible. For the horizontal injection of chemical agents sharp needles with tiny tips (see fig. 4.4 C) had to be used to prick the second hole into the embryo membrane without squeezing its interior out of the first hole.

Imaging in the *Drosophila* embryo had to be done in epi-illumination since the yolk in the center of the embryo strongly scatters light. For the same reason, we could not use a standard optical tweezers-based microrheology approach with interferometric displacement detection through the sample. A disadvantage of video microrheology is the limited bandwidth, with frame rates of 50/60 Hz when using standard cameras. We extended bandwidth to kHz using a high-speed camera. Embryos were imaged

Figure 4.3: Rearing, alignment and injection of fly embryos
(A) Picture of a fly cage where embryos can be collected at an agar plate at the top of the tube. (B) Alignment of the embryos under a stereo microscope in order to perform easy and fast injections later on. (C) Horizontal 'in-situ' injection right at the place where subsequent imaging is done.

with the custom-built microscope described in section 2.1: Excitation sources were a 561 nm laser, a 532 nm laser and a 489 nm laser. By inserting an additional mirror the low magnification channel could be used for the injection procedure (see fig. 4.5).

Epi-fluorescence images were taken with the Nikon objective. The Cairn image splitter was used to image beads and nuclei onto different regions of the low-speed camera. By a dichroic mirror beads could alternatively be imaged onto the Photron high-speed camera (see fig. 4.6 A). With this setup, beads and nuclei could be observed simultaneously at slow video rates (200 ms exposure) in order to identify spots of interest inside the embryo, to determine and document the developmental stage of the embryo by observing the nuclei, and to measure lateral distances between beads and nuclei. We measured normal distances (to the cortex) between the nuclear layer and the beads by means of the feedback-controlled piezo element. Fluorescent images of fluctuating beads were then recorded with the high-speed camera, optionally followed by a recording with the low-speed camera. By that an extended frequency range could be probed (see fig. 4.6 B). For the high-speed imaging a region of 128 x 160 pixel was recorded at frame rates of 8, 16 or 20 kHz over 2 to 6 seconds. For these short periods, the sample was exposed to the 561 nm laser with peak power densities of 6 kW/cm^2 = 60 mW/$4\mu m^2$. The camera cooling fan was switched off to reduce noise.

Figure 4.4: Injection geometry and injection needles
(A) Schematic drawing of the injection geometry. Beads were injected in a vertical manner with a needle with a long and thin tapper **(B)**. Drugs were injected at the posterior end of the embryo with a beestinger like needle **(C)**.

After each recording, the camera had to cool down for five minutes, which limited the possible number of recordings over a certain time period, e.g. during a nuclear division cycle. The recordings at low speed were performed at a frame rate of 20 Hz by choosing a region of interest of 256 x 256 pixel and performing 2 x 2 pixel binning. We recorded image series of typically 1000 to 3000 frames. The sample was illuminated with the 489 nm laser and the 532 nm laser for imaging at normal video rates. Peak power densities here were 25 W/cm^2 at 532 nm, and 62 W/cm^2 at 489 nm in the sample plane.

Figure 4.5: 'In-situ' injection of fly embryos
(A) Picture of the micro injector head at the sample holder and objective. **(B)** Low-magnification beam path for injection detected by a simple video camera. **(C)** Image of the injection needle (cone-shaped shadows) perpendicularly touching the coverslip (at a yellow marker point). **(D)** Injection needle inside an embryo.
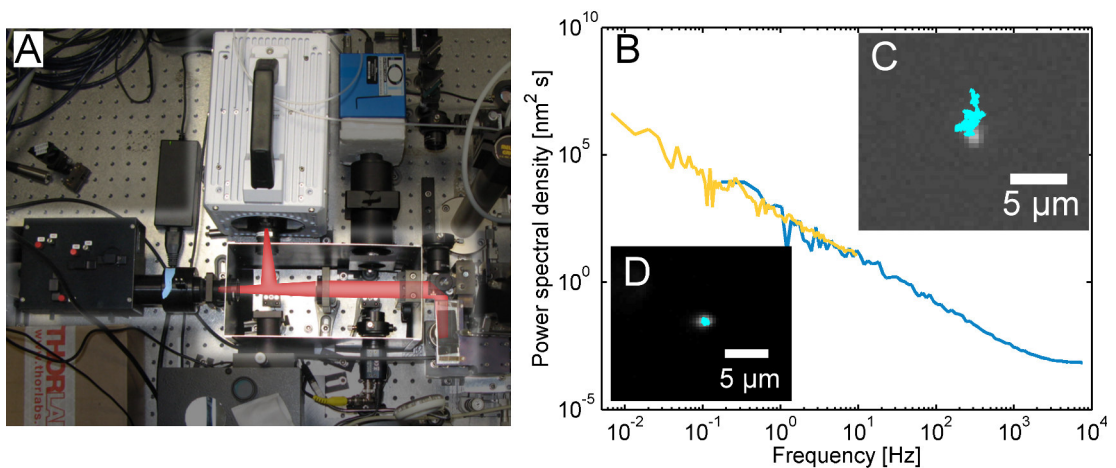
Figure 4.6: Combined high-speed/ low-speed detection
(A) Detection beam path for a combined high-speed/low-speed recording. Beam is split by a switchable mirror and imaged onto a high-speed camera (white) and onto the image splitter (black box) of a low-speed camera. **(B)** Power spectral densities of the same bead inside the embryo, recorded with the low-speed camera (orange curve) and the high-speed camera (blue curve). **(C)** and **(D)** Images and position trajectories of the same bead recorded with the low-speed and the high-speed camera, respectively.

Perturbations and artifacts

To minimally perturb the regions of the embryo that we planned to probe and to target the sites of interest as precisely as possible, we settled on an injection geometry perpendicular to the coverslip (see fig. 4.4). An injection into the central yolk did not lead to the desired result of beads being spread inside the whole embryo, since the diffusion length of the microspheres are small there. However, the vertical injection has a side effect which has to be mentioned here. In order to allow an
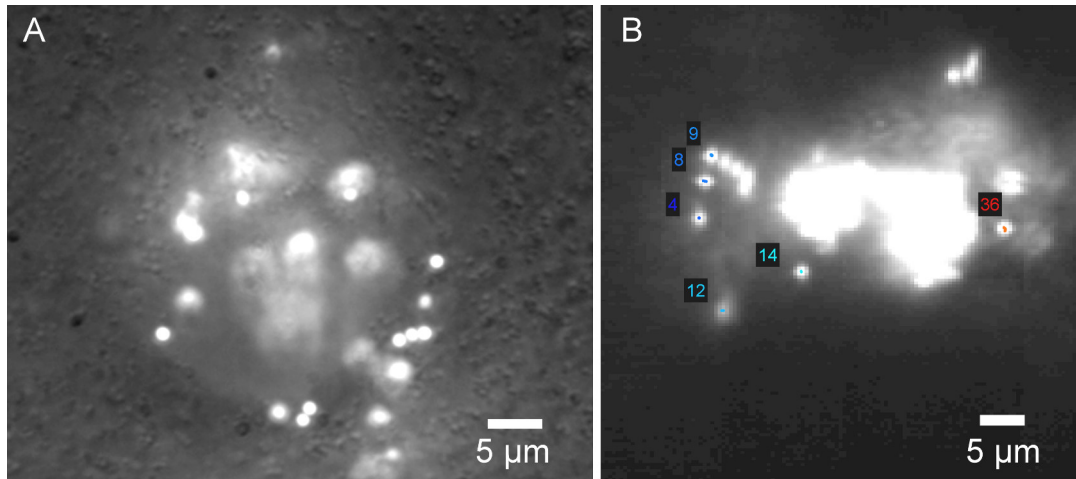
Figure 4.7: Perturbation of the embryo by microinjection and bead agglomeration
(A) The image shows an 'injection channel' formed by the penetration of the injection needle through the embryo. In the shown case the needle touched the coverslip and partly destroyed the cortical membrane which makes the 'injection channel' more visible. **(B)** Fluorescence image of beads inside the embryo which agglomerated after injection.

unhindered flow of beads into the embryo during injection, i.e. that beads do not jam in the needle, the opening has to be sufficiently large. The outer circumference of the injection tip is estimated to be around 10 μm. Thus, the tip of an injection capillary is likely to interfere or at least temporarily strongly perturb the cytoplasm near the path of insertion. Figure 4.7 A shows a situation, where a large needle hit the surface of the coverslip and thus touched and destroyed the membrane of the embryo. Though this is an extreme scenario, it reveals the problem. The injection produces kind of a 'tunnel' which right after injection is filled with a mixture of beads, water and yolk. In favor of measuring the unperturbed embryo's interior the injection was carried out before the cortical migration of the nuclei took place (approximately half an hour to an hour after the egg was laid by the fly). This was advantageous because it supported a further spreading of the bead inside the embryo, away from the injection site. Nevertheless, the 'injection tunnel' was often observed to persist till the end of the experiment. A second point to be mentioned is the fact that beads agglomerated from time to time in the embryo or were injected as clumps (though pretreated by ultrasonication). Figure 4.7 B displays this situation with a bright spot of agglomerated beads in the center. As soon as one has the situation of two beads attached to each other the model assumption introduced for microrheology does not hold anymore. Therefore, only individual beads that were far enough away from the 'injection tunnel' were further analyzed.

Microrheology inside the nuclear layer | 4.3

As a first approach we targeted at probing the nuclear layer. This layer has a thickness of about 5 μm and, in interphase, consists of the nuclei itself, a microtubule network and the centrosomes associated to it (see fig. 4.1 and 4.2). Figure 4.8 shows
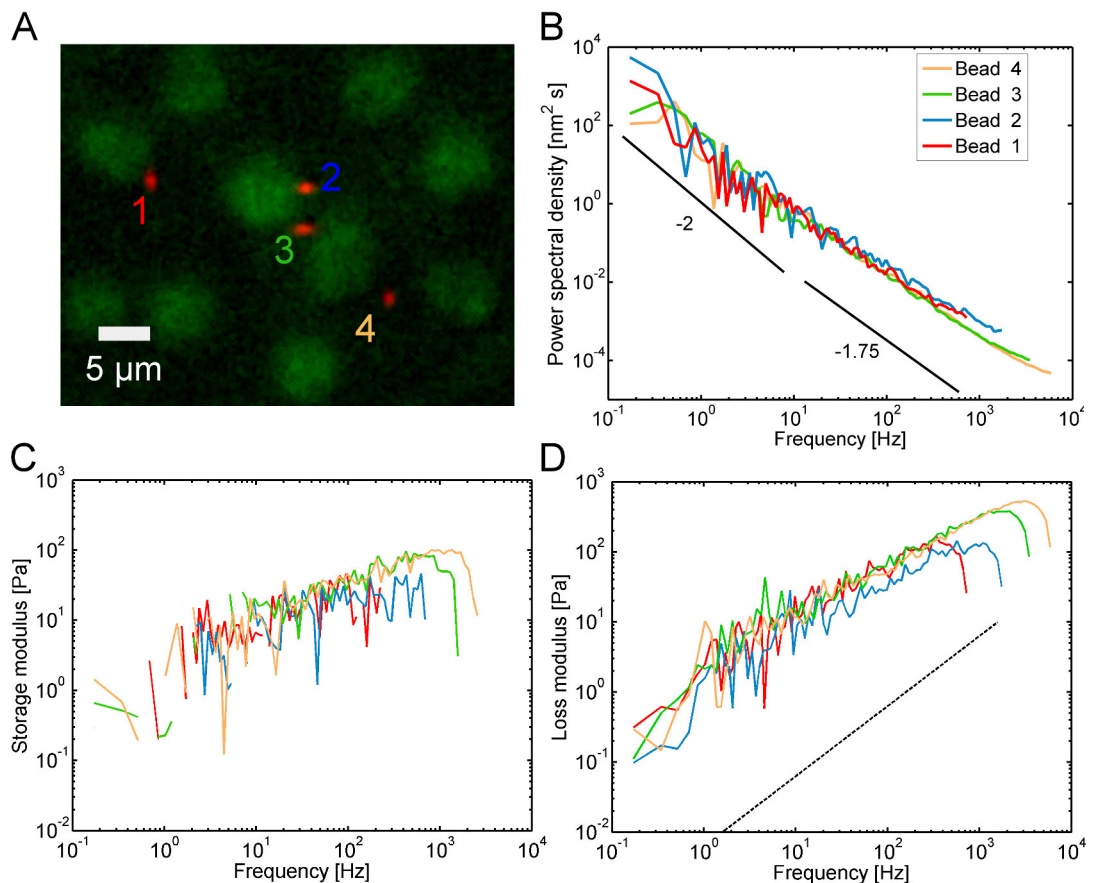
Figure 4.8: Exemplary microrheology data from within the nuclear layer
(A) A typical fluorescence image of fluorescent beads (red) dispersed within the nuclear layer (green). **(B)** Power spectral densities of all four beads shown in the fluorescence image. Slopes are drawn for comparison. **(C)** and **(D)** Storage and loss modulus of the beads shown in (A). Dashed line indicates the viscosity of water.

a typical dataset recorded from probe particles located within the nuclear layer. Panel A is a merged fluorescence image of fluorescent beads in red and nuclei in green taken by means of the image splitter/ low-speed camera combination. The beads are spread within the nuclear layer and located within different nuclear compartments. Figure 4.8 shows the corresponding color-coded PSDs of the beads shown in A. Though located at different positions the four beads give very consistent results with variations below the noise level (see also section 4.5 for further discussion). Power law decay curves with logarithmic slopes of -2 and -1.75 are drawn for comparison. The first one is typical for Brownian motion in a viscous liquid (see section 3.3.2), whereas latter one can be seen for a particle's motion in a viscoelastic environment [48].

4.4 | **Microrheology in different layers of the embryo**

The cytoplasm of the *Drosophila* embryo is a dense solution of biomacromolecules [49], but the fraction of structural cytoskeletal components varies within the embryo. Actin and microtubules are more concentrated in between and near the nuclei (see
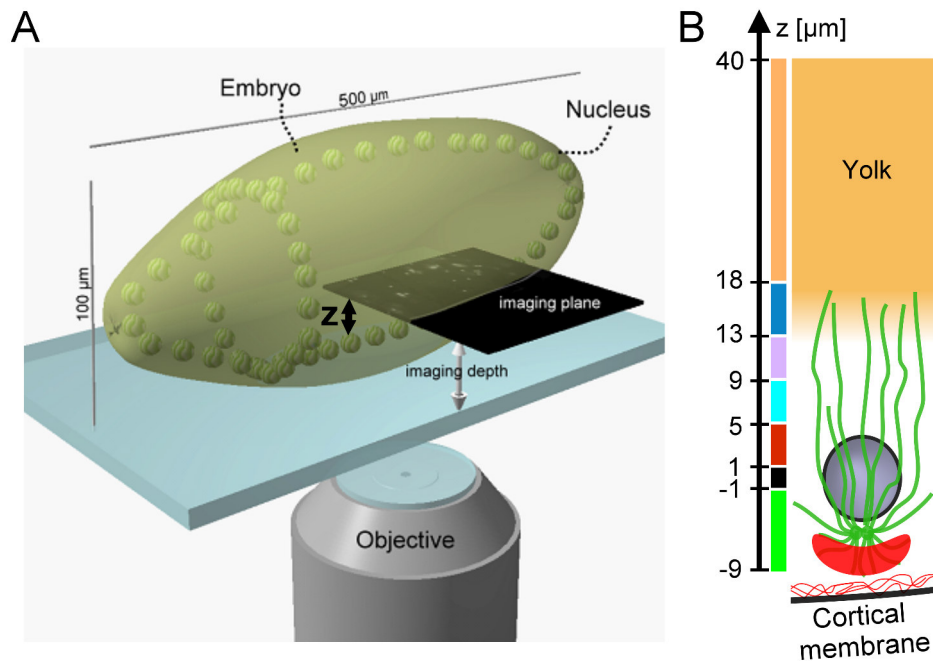
Figure 4.9: Illustration of the different measured layers within the embryo
(A) 3D model of a syncytial fly embryo. Nuclei indicate the cortical layer. The measuring parameter z is defined as the distance between the imaging plane and the center of the nuclear layer. **(B)** Schematic drawing of one nuclear compartment along the z axis. The color-coded bars show the sections in which measurements were taken and averaged.

fig. 4.2). We therefore measured the viscoelastic moduli in different layers of the embryo. During injection beads were typically positioned along the whole 'injection tunnel' and were then incorporated or diffused laterally from there further into the embryo. The nuclear layer is an important part for the arrangement of cytoskeletal filaments and it can be genetically labeled. That is why we chose it as a reference plain (see fig. 4.9). This plane was determined by imaging it at the highest contrast and the largest circumference of the nuclei, i.e. at their equatorial plane, with a precision of $\pm 1 \mu m$. The embryo is oriented with its long axis parallel to the substrate and we define the parameter z as the distance along the optical axis of the microscope between the probe particle and the nuclear layer, with positive z towards the yolk of the embryo. This distance was measured by means of the high-precision piezo-positioner. In the preparation step the embryos were glued to the coverslip, hence the nuclear layer was flat in these regions. Data was taken only in this part of the embryo. The data obtained that way was then sorted into different sections according to their distance to the nuclear layer (see fig. 4.9).
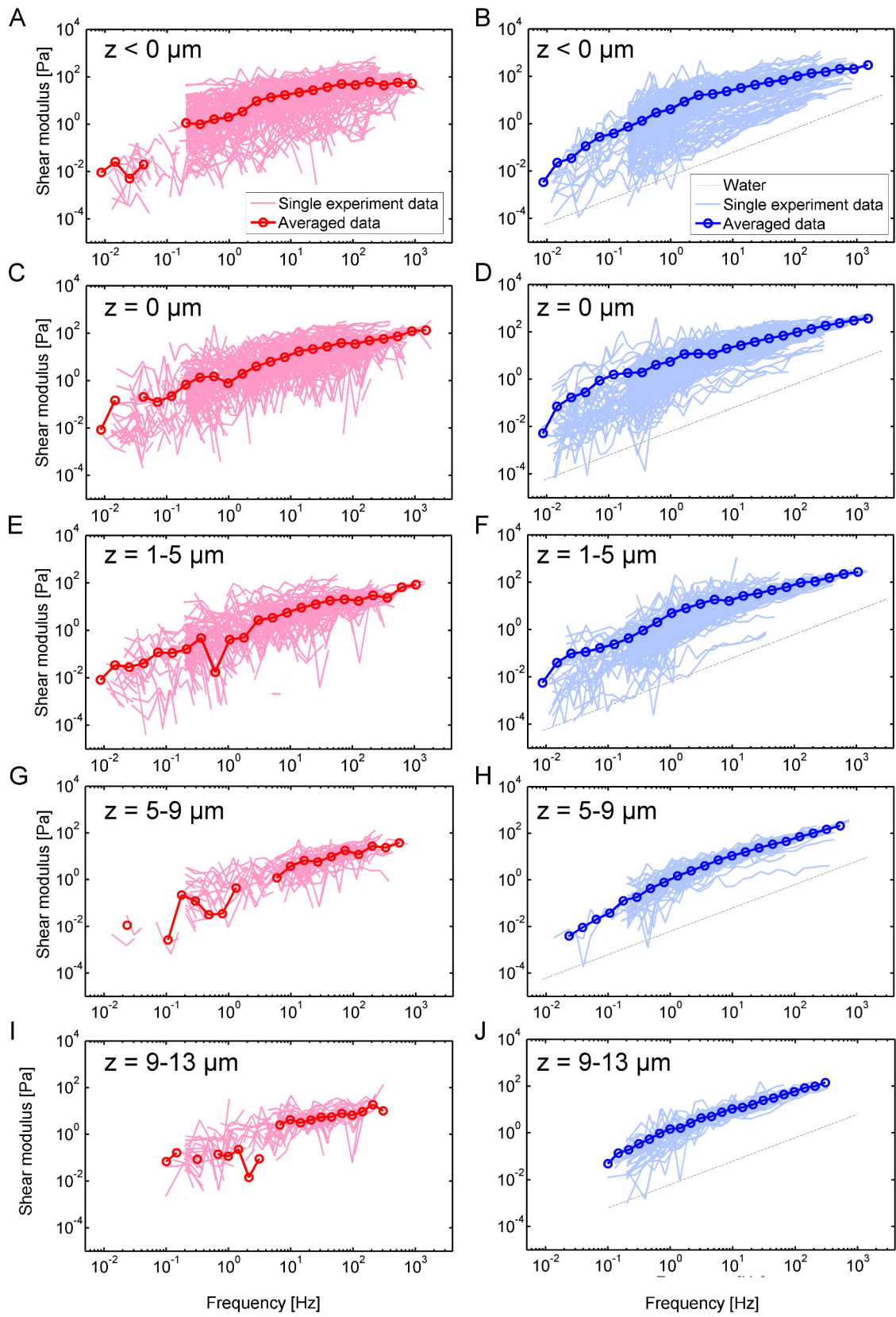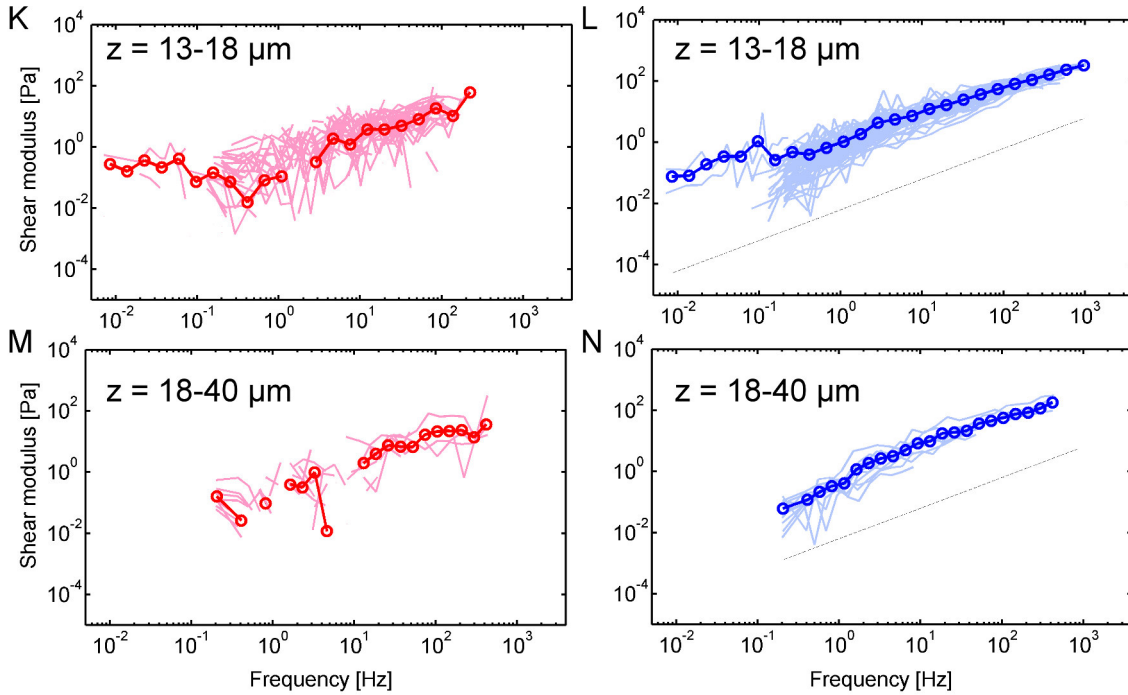
Figure 4.10: Arrays of shear moduli curves measured at different layers
Left: Arrays of elastic storage moduli over frequency measured at different distances z to the nuclear layer. Right: Arrays of viscous loss moduli over frequency measured at different distances z to the nuclear layer. Each measured bead gives a single shear moduli curve. Logarithmically binned averages are taken over all of the shown curves.

Figure 4.10 displays the elastic storage modulus and the viscous loss modulus over frequency measured at the different sections along the optical axis. The solid thick lines are averages of the shaded curves corresponding to individual beads. This presentation shows the spreading of curves, thus an estimate for the standard error and gives an impression of the broadness and variation of the distribution of shear moduli. The elastic modulus was more noisy, both because of its low amplitude and the way it needs to be calculated via a Kramers-Kronig integral. Missing parts of the curve are due to negative values which are not shown on the logarithmic scale. Using the combination of a high-speed and conventional camera, we could measure the shear moduli over five decades of frequency and up to the kHz range.

In every probed section of the embryo the loss modulus $G''(f)$ exceeds the storage modulus $G'(f)$, thus the viscous response of the cytoplasm dominates the elastic response (see fig. 4.11).

$G''(f)$ showed approximate power law dependence on frequency at frequencies above ~10 Hz. Power-law slopes were clearly smaller than one, which is indicative of a viscoelastic material and consistent with the measured $G'(f)$ of similar amplitude. For comparison, slopes of 1/2 and 3/4 are drawn in figure 4.12, 1/2 being the expected exponent for Rouse dynamics of flexible polymers, e.g. DNA networks [50, 51] and 3/4 expected for networks of semi-flexible filaments, for instance entangled actin networks [27, 52–55]. At lower frequencies, curves bent towards slopes closer to 1, reflecting more viscous fluid-like response. The elastic modulus $G'(f)$ shows a power-law slope between 1 and 3/4 in the relatively noisy low-frequency range and appears to approach an elastic plateau at high frequencies between 100 and 1000 Hz. This behavior is different from what is seen in normal, non-embryonic cells [56]
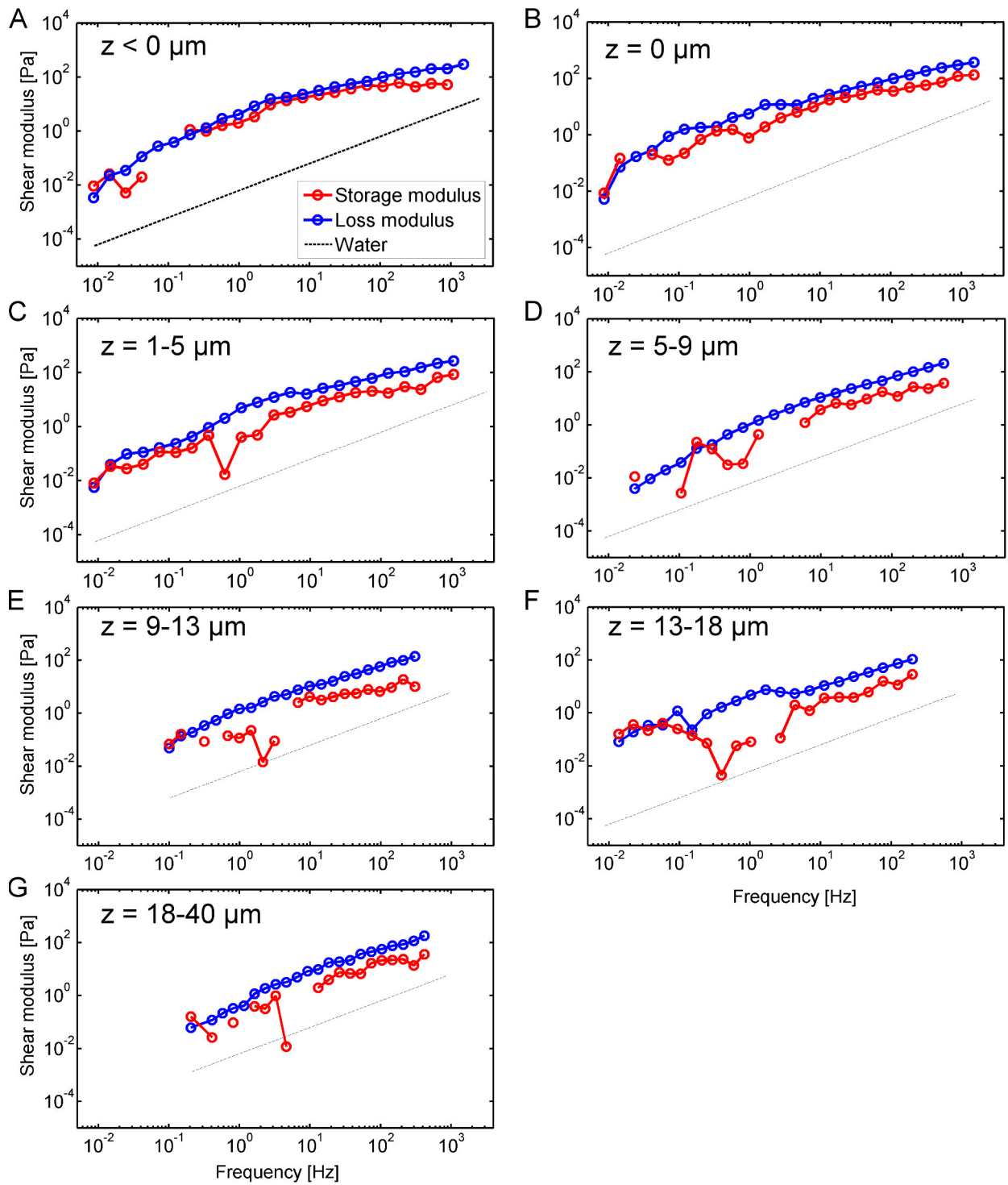
Figure 4.11: Comparison of the storage and loss moduli
(A) - **(G)** Average curves of the storage (red) and loss (blue) moduli measured at different distances z to the nuclear layer.

or in entangled or crosslinked in-vitro actin networks [55, 57]. It is more comparable to the response of dilute weakly entangled solutions of a filamentous virus [48]. These solutions were found to behave viscoelastic for high frequencies, according to internal dynamics of the filaments. Below a certain concentrations the filaments do not overlap sufficiently enough anymore to be entangled and the low frequency response is dominated by the diffusive behavior of rigid rods. We therefore conclude that the parts of the embryo we could access with our 1 μm probe beads possess mainly loosely entangled cytoskeletal networks.
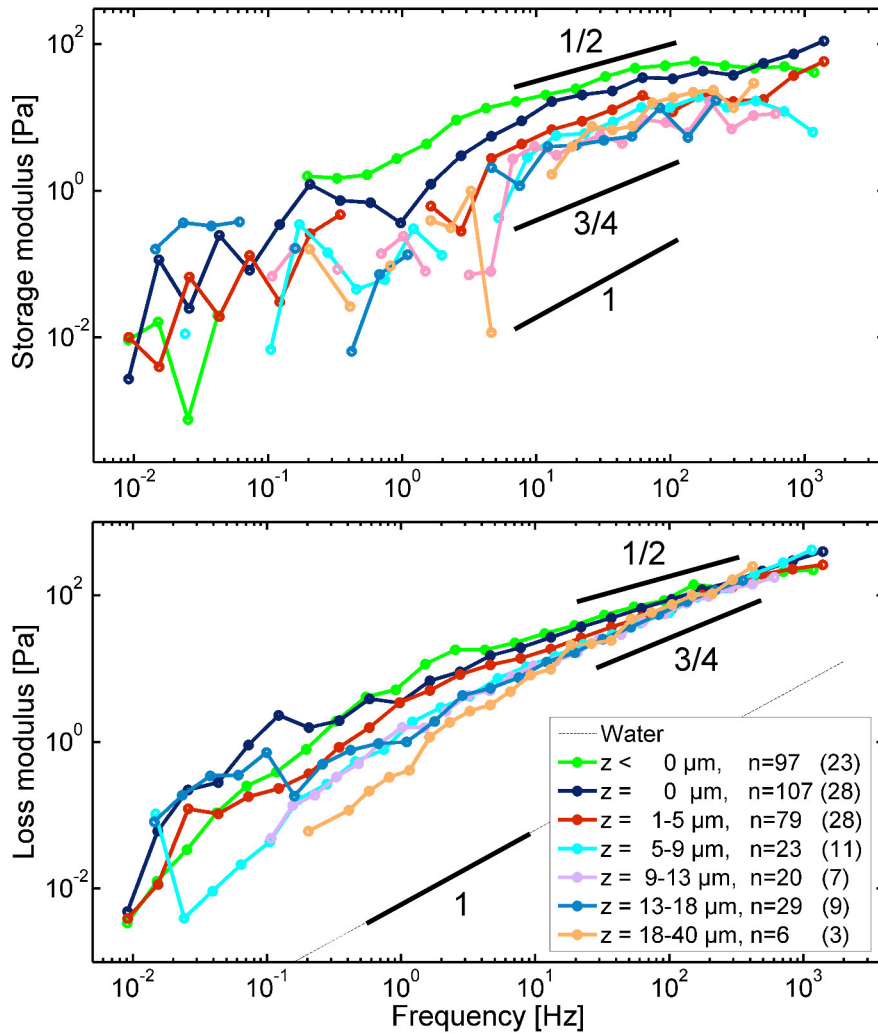
Figure 4.12: Shear moduli measured at different layers
Averaged storage moduli (upper graph) and loss moduli (lower graph) measured at different distances z to the nuclear layer. Different slopes are shown for comparison. Given n indicate the number of beads (embryos) taken into account.

While the response was predominantly viscous in all the layers of the embryos that we probed, there was a gradient of the moduli from the yolk towards the cortex. Figure 4.13 shows absolute values of G' and G'' at different distances from the nu-
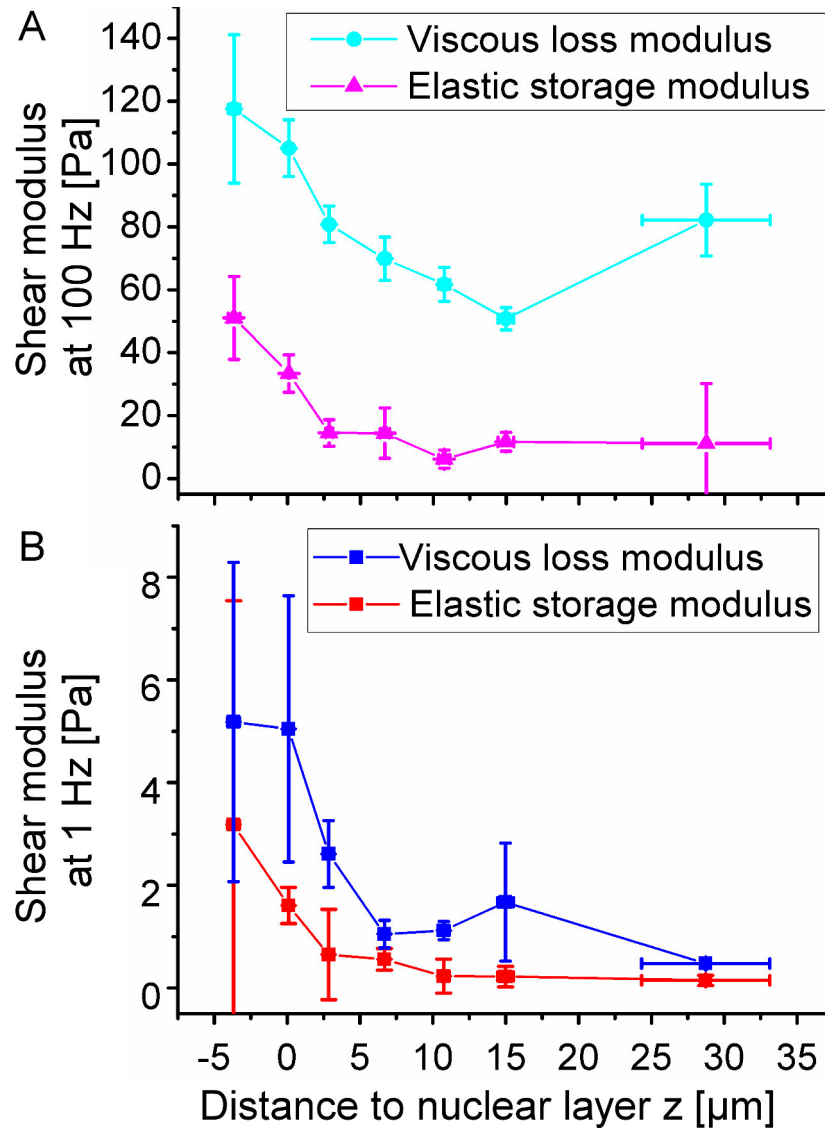
Figure 4.13: **Absolute values of the shear modulus at 1 Hz and 100 Hz**
Elastic and viscous modulus at 100 Hz **(A)** and 1 Hz **(B)** for different distances to the nuclear layer z. Values were determined by fitting the loglog curves in figure 4.12 with a 2nd order polynom to account for the observed bending. The shown error bars are the SEM for the measured distances z (x-error) and the SEM for the measured shear modulus where the variance from embryo to embryo was taken into account (y-error).

clear layer at 100 Hz and 1 Hz (the values were averaged over a window of 1 Hz). G' and G'' increased when approaching the cortex from the interior of the embryo. We found the distance between cortex and nuclear layer to be about 8-11 μm. Note that G' and G'' stayed almost constant in the range of z = 5 - 40 μm and only started to increase when further approaching the embryo's external shell. The mean

values for the storage and loss moduli at intermediate distances (5 - 40 μm) to the nuclear layer were $G'(1 \text{ Hz}) = 0.29 \pm 0.14$ Pa and $G''(1 \text{ Hz}) = 1.08 \pm 0.04$ Pa. This makes the interior of the embryo three orders of magnitudes more viscous than water which is comparable to what was found in the cytoplasm of embryonic cells in *Caenorhabditis elegans* [58] and in oocytes of *Astropecten aranciacus* starfishs [59] but about fifty times more viscous than Xenopus egg cytoplasmic extracts [60]. With our experimental approach we are able to probe our samples up to the kHz regime. This is advantageous because fluctuations caused by active force generators like motor proteins happen on timescales in the order of milliseconds. In fact non-equilibrium fluctuations are only expected to have an effect below a certain frequency, which was found to be around 10 Hz (further discussion see section 4.10). Figure 4.13 shows absolute values of the shear modulus at two frequencies, 1 Hz and 100 Hz. Latter one is clearly above the frequency limit where non-equilibrium fluctuations are expected and it shows the same trend of increasing moduli from the yolk to the cortex.

4.4.2 High-frequency power law slopes of the shear modulus

Looking at the array of shear moduli (see fig. 4.12) one can see that the curves follow a power law between ~5 Hz and their high-frequency cutoff. In the low frequency region they bend to lower values and deviate from this behavior.
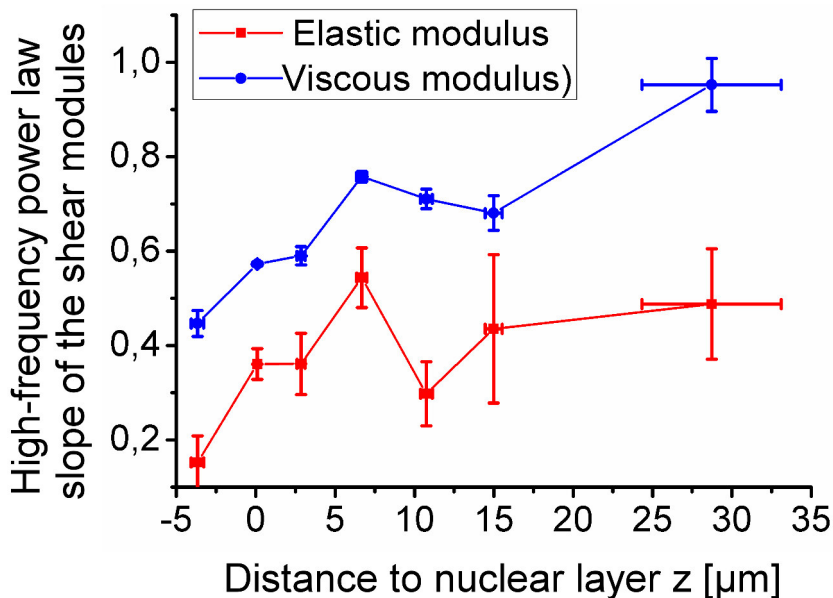
Figure 4.14: High-frequency power law slopes measured at different layers
Power law slopes of storage and loss modulus measured at different distances z to the nuclear layer. The values were obtained by fitting the curves in figure 4.12 in the frequency range above 10 Hz.

The high-frequency behavior of the curves was quantified by fitting with a power law function to extract the power law slopes for the different regions of the embryo.

The results are plotted in figure 4.14 showing the slope of the elastic modulus to stay almost constant after an initial increase whereas the viscous modulus curve slopes increase from the cortex into the yolk. Latter ones reach a slope of 1 deep inside the yolk, hinting at a viscous response there, and stay below one in the rest of the embryo implying a viscoelastic response. For small z the slope seems to become even smaller than 3/4. A power law slope of the shear modulus of 1/2 is not only seen in flexible networks but also in elastic, crosslinked networks of semiflexible filaments where motor proteins put the single filaments under tension [54, 61, 62].

Data variance | 4.5

Figure 4.10 shows all raw, single-bead data and its averaged curves for the shear modulus in different sections of the embryo. It is interesting to compare the spreading of the curves, i.e. the standard deviation (SD) within one embryo and between different embryos. The power spectral density curves were integrated in a frequency
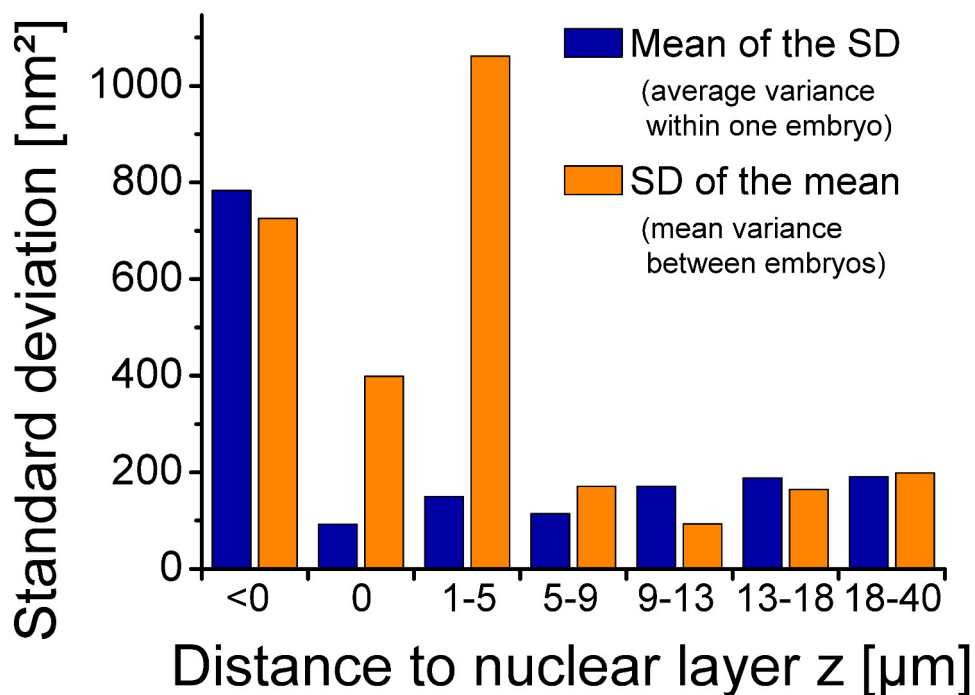
Figure 4.15: Variance of position PSDs between embryos and within one embryo
Variation of probe position fluctuations in different layers. An estimate of probe position variance was obtained by integrating the position PSD in the window between 5 and 300 Hz. Then the variance (SD) of these values was calculated for every embryo separately and averaged together. This gives a measure for the data variance within an embryo ('Mean of the SD'). Secondly the position variance was averaged for each embryo. Then the variance (SD) of these values was calculated which is a measure for the data variance between different embryos ('SD of the mean').

window of 5 to 300 Hz which gives the variance in that range and thus is a measure for the particle's fluctuation magnitude. Firstly, I calculated the SD for those values

of bead fluctuation measured within each embryo and then averaged these values from all embryos. This is a scale for the mean data variance within the embryo, in a strict sense, it is the mean spatial variance of the bead fluctuation within the imaging plane. Secondly, I averaged the position variance of all particles within one embryo to then calculate the SD of all these averaged values, which gives the data variance between the different embryos. This calculation was done for all measured sections and its results are displayed in figure 4.15.

The average variance within an embryo stays almost constant in the range from $z = 0$ μm to $z = 18...40$ μm, but strongly increases below the nuclear layer. In section 4.3 I stated a low spatial variance of the PSD and shear moduli within the nuclear layer and this is further supported here: The mean spatial variance (blue) of the power spectral density within the nuclear layer is the lowest compared to all other parts of the embryo. Compared to the value within the nuclear layer the value below the nuclear layer is almost eight times higher, indicating a significantly higher spatial homogeneity of stiffness inside the nuclear layer. That is a reasonable finding since the region below the nuclear layer contains the centrosomes (in interphase) with the astral microtubules and the microtubules which form the baskets (see fig. 4.1). This is in stark contrast to the microtubules in the nuclear layer, where they seem to be rather oriented perpendicularly to this layer forming a more homogeneous network (see fig. 4.2).

The variance between embryos (orange) has a more or less constant value in the region of $z = 5...40\mu m$ and increases around the nuclear layer. Here, a larger structural variation between embryos compared to other regions seems to be present. Even more, at $z = 1...5$ μm the variance from embryo to embryo is the highest of the whole embryo and clearly exceeds the lateral variance (blue) by a factor of seven. In general it seems that the region around the nuclear layer has a larger structural variation from embryo to embryo compared to other regions. That means that the magnitude of particle fluctuations vary much stronger from embryo to embryo than from one spot of the embryo to another spot in the imaging plane.

Finally one has to keep one critical point in mind: Figure 4.15 displays averages over the denoted sections along the z-axis. If there was a strong gradient of stiffness along this axis the variance within an embryo would seem larger than it actually is.

Drug interference experiments | 4.6

To test the contribution of actin and microtubules to the measured shear moduli, we performed drug interference experiments. We injected latrunculin A and colcemid to disrupt actin filaments and microtubules, respectively. Embryos that expressed fluorescently labeled tubulin and utrophin, an F-actin-binding protein, served as controls to confirm successful depolymerization. Figure 4.16 shows images of actin caps (green) and microtubules around the centrosomes (red) right after drug injection (which is equivalent to the untreated case) and some time after it. The images show the cytoskeletal structures vanishing over a time period of ~270 seconds for actin and ~250 seconds for microtubules. Microrheology measurements were per-
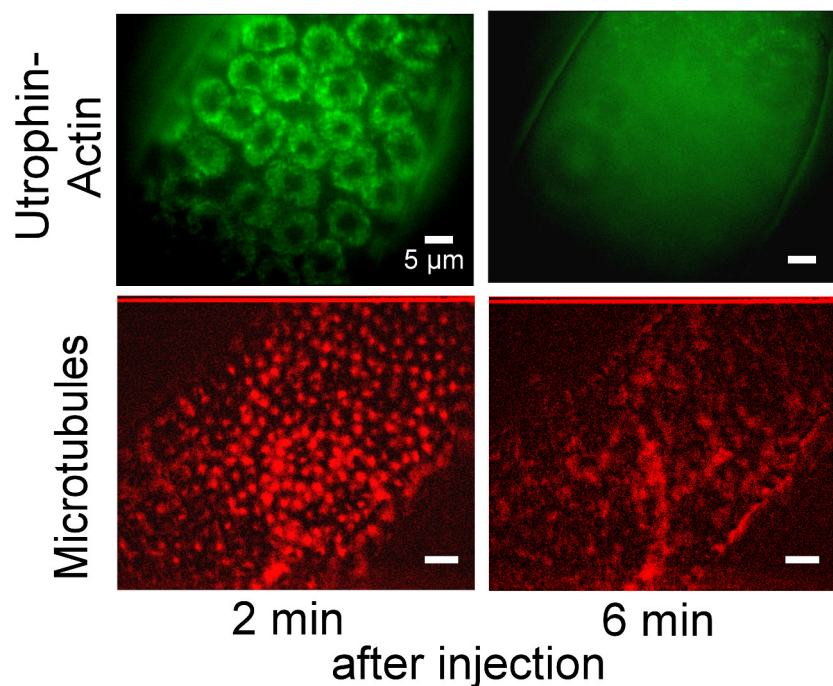
Figure 4.16: **Proof of depolymerizing actin and microtubule structures**
Fluorescence images of actin caps (green) and microtubules (red) two and six minutes after drug injection. Actin structures are visible due to the GFP-labled utrophin which is an actin-binding protein. Microtubules are labeled with mcherry. The visible structures are the centrosomes where microtubule density is high. The movie snapshots were taken 2 minutes after drug injection showing unperturbed cytoskeletal structures which depolymerized over the following four minutes.

formed before and after injection (~5 min after injection). Probe beads were located in different layers. In about half of the colcemid-treated embryos, we saw increased fluctuations of the probe particles leading to decreased moduli. The generally relatively small effects are consistent with the fact that the response was dominantly viscous to begin with, corresponding to at best a loose cytoskeletal filament network. To quantify the effect of the chemicals, the variance of bead position was calculated by integrating the PSDs over a frequency window from 5 to 300 Hz (see fig. 4.17). The mean ratios of bead-position variance after and before drug injection averaged over all measured beads are shown in figure 4.18. Treatment with colcemid increased position variance in the selected frequency band about 3 fold whereas the addition of latrunculin did not produce a significant effect.
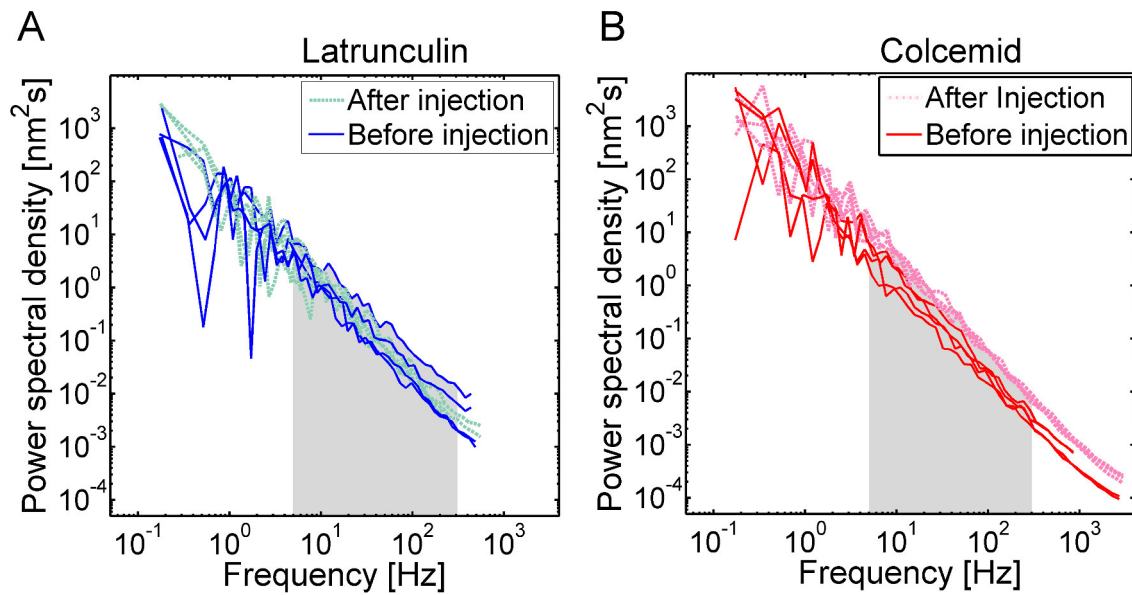
Figure 4.17: Drug interference analysis - PSD integration
Position PSDs from drug interference experiments. (A) PSDs before and after the injection of latrunculin A to disrupt the actin cytoskeleton. (B) PSD before and after colcemid injection to disrupt the microtubule cytoskeleton. Position fluctuations remained unchanged after latrunculin injection and slightly increased after colcemid injection. Measurements were taken at $z = 8.7 \pm 0.7 \ \mu m$ and $z = 6.1 \pm 1.4 \ \mu m$ mean $\pm$ SEM), respectively, during interphase. The gray shaded area shows the frequency range over which the PSDs were integrated (5-300 Hz) to obtain a measure for the position variance.
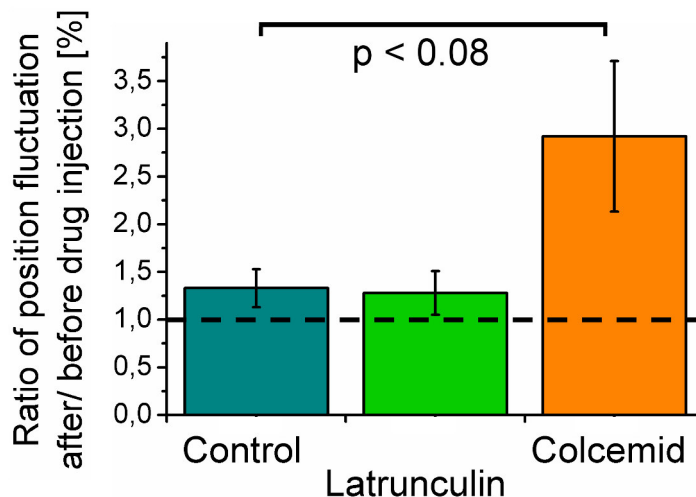
Figure 4.18: Effect of drug injection
The graph shows the ratio of position fluctuation (obtained by PSD integration) after and before drug injection for latrunculin, colcemid and water (as a control). $N_{latrunculin} = 18$ embryos, $N_{Colcemid} = 11$ embryos and $N_{water} = 15$ embryos. Particles were widely spread inside the embryo ($z_{colcemid} = 0 \cdots 15 \ \mu m$; $z_{latrunculin} = -8 \cdots 40 \ \mu m$; $z_{water} = -2.3 \cdots 27.4 \ \mu m$). The depolymerization of microtubules makes the interior of the embryos significantly softer whereas the injection of latrunculin only has a minor effect.

These findings are in good agreement with the distribution of cytoskeletal filaments in the embryo. The confocal control images of fixed embryos in interphase (see fig. 4.2) show a dense cloud of microtubules around the nuclear layer, which thins out rapidly towards the interior of the embryo, such that individual filaments or bundles can be optically resolved. F-actin was solely concentrated close to the cortex and inside the actin caps but could not be seen in the interior of the embryo or inside the nuclear layer. The micron-sized probe beads we used did not readily enter the dense network of the actin caps or the cortical actin.

Motor inhibition

To further test for non-equilibrium contributions to the measured fluctuations we inhibited motor activity pharmacologically. Since in Drosophila myosin is insensitive to blebbistatin we injected the rho kinase inhibitor Y-27632 to inactivate non-muscle myosin II motor proteins [40]. Just like before we integrated the power spectral density, but in the range of 0.3 to 300 Hz to quantify the effect of drug injection.
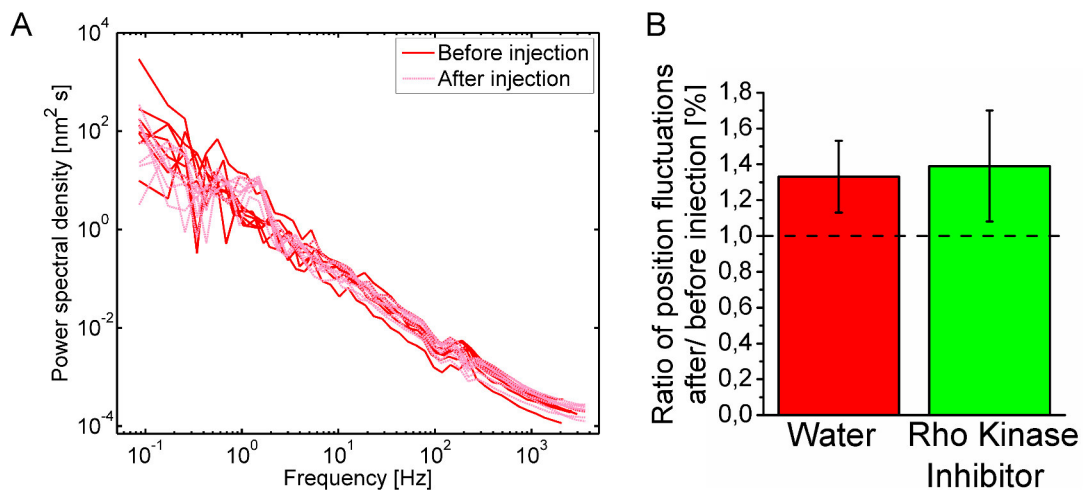
Figure 4.19: Effect of myosin motor inhibition
(A) Exemplary PSD dataset for injection of rho kinase inhibitor: A set of PSD recorded from microspheres localized close to the cortex ($z = -11$ μm). Curves show no significant difference of the particle's motion (in shape and magnitude) before and after myosin motor inhibition. **(B)** Ratio of position fluctuations (obtained by PSD integration) after (N=85 beads) and before (N=65 beads) injection of rho kinase inhibitor and water. $N_{RKI} = 15$ embryos. Particles were widely spread inside the embryo ($z_{RKI} = -9 \cdots 32$ μm).

We did not find a significant difference of the drug-treated embryo compared to the control experiment when only water was injected (see fig. 4.19). This finding further supports our passive microrheology approach.

4.7 Shear moduli measured at different times during the nuclear division cycle

After mapping spatial changes of the shear modulus inside the embryo we performed measurements at different points in time. Therefore, we tracked fluctuations through nuclear division cycles. During the coordinated and synchronized nuclear division periods the cytoskeletal structures in the nuclear layer change quite dramatically, with the microtubule network rearranging to form the mitotic spindle and actin caps extending further down into the embryo separating neighboring nuclei [36].
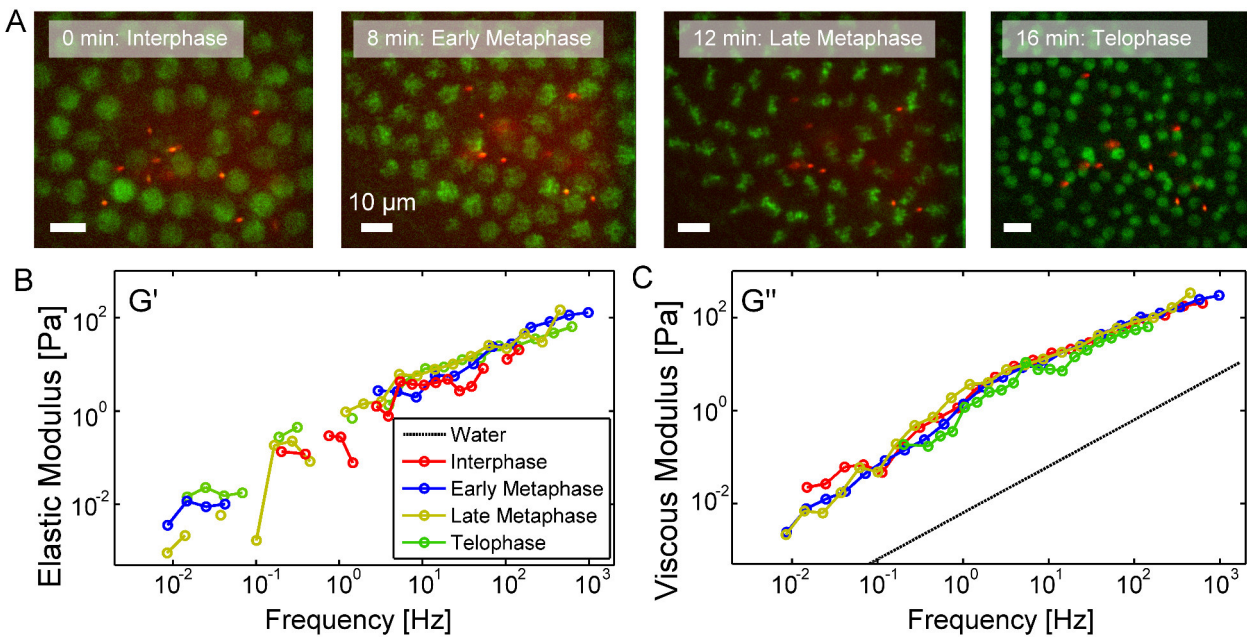
Figure 4.20: Snapshots and shear moduli measured over the nuclear division cycle
(A) Sequence of fluorescence images of the nuclear layer with dispersed beads at different stages of the nuclear division cycle. First image was taken in interphase, second image shows early metaphase when DNA starts to condense and the nuclei appear to have an irregular shape. Third image corresponds to late metaphase, right before nuclear division and the last image shows the nuclear layer during telophase/ early interphase after nuclear division when the corresponding daughter nuclei still have a positional correlation. **(B)** Elastic storage moduli for the different developmental stages shown above. The curves are averages over six beads. Negative values are not shown in the double logarithmic scale. **(C)** Viscous loss moduli over frequency at the different time points indicated above.

We first calculated apparent shear moduli over a nuclear division cycle, assuming predominantly thermal driving forces. Figure 4.20 A displays a representative series of fluorescence images taken over a period of 16 minutes. Beads remained embedded in the nuclear layer from interphase, early metaphase, late metaphase to telophase/ early interphase again. We typically observed that the probe beads were pushed out or possibly diffused out of the nuclear layer after mitosis so that measurements over more than one division cycle could only rarely be taken.
Within the accuracy of the measurements, $G'(f)$ and $G''(f)$ show no obvious variation (see fig. 4.20 B and C). To prove that this is not just an effect due to averaging over many beads, individual particles were tracked.
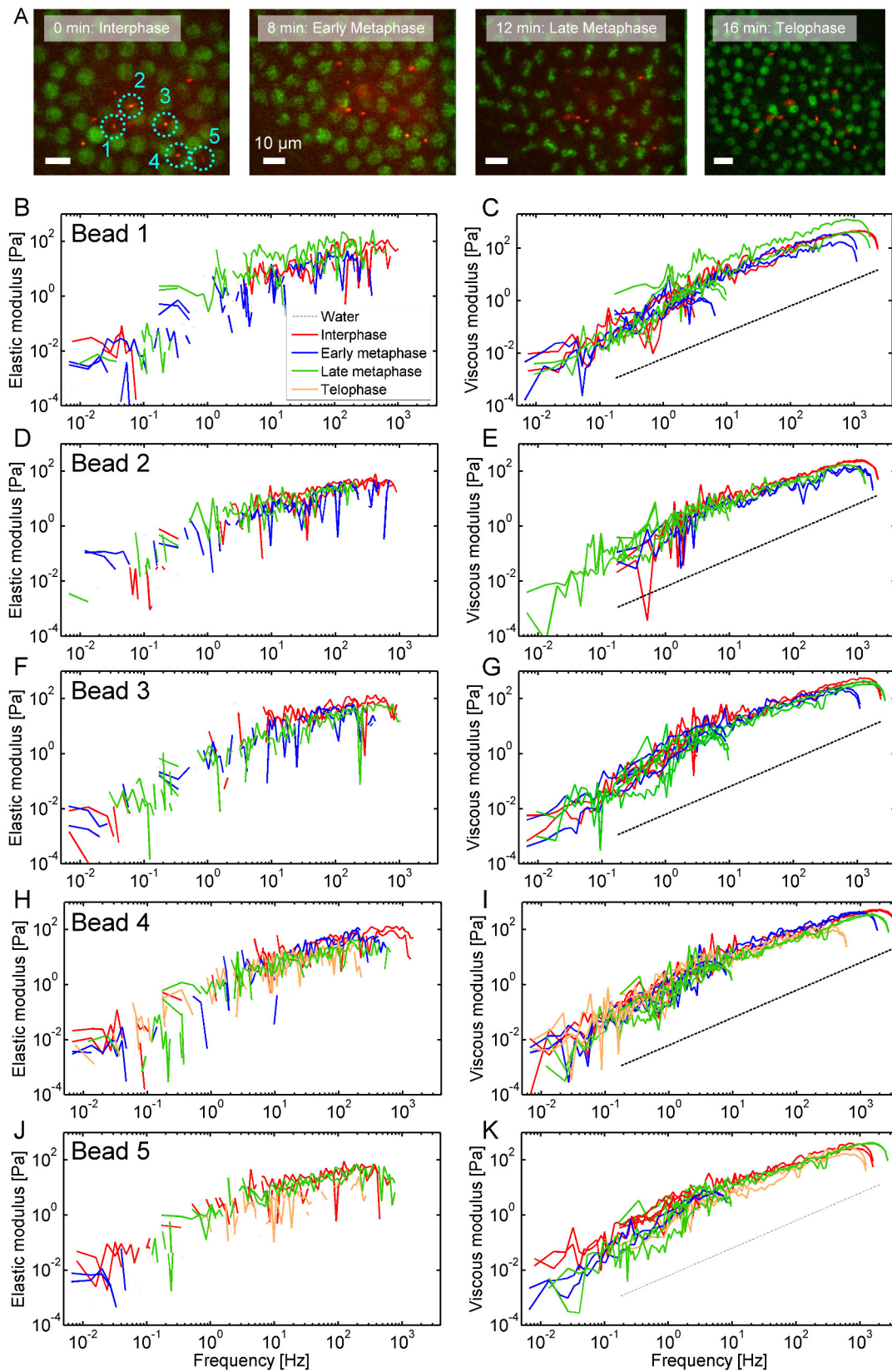
Figure 4.21: An array of shear moduli measured by following single particles over time
(A) Image series showing beads within the nuclear layer (see also figure 4.20). Five beads were tracked individually through the depicted nuclear division cycle. **(B)** - **(K)** The graphs show elastic and loss moduli for the five beads at different nuclear division stages. Each graph shows the measurement in x and y direction as well as high-speed and low-speed data if present. Colors code for the different time points. Data is logarithmically binned. In the double logarithmic plot only positive values are shown.

The results are shown in figure 4.21 at a higher number of bins to not miss finer details. Even then there are no clear differences within the measurement accuracy between the different stages of the nuclear cycle. This result makes it very likely that fluctuations in the frequency range evaluated were indeed mostly thermally driven. A possible explanation for this finding, in spite of obvious active motions in the nuclear layer during nuclear divisions, is that the active processes happen slowly, on a timescale of minutes, which would affect the low end of the frequency scale, where noise may have masked subtle changes.

Measurements at anaphase

We did, however, find some evidence for slow non-equilibrium motion in recordings taken during and right after anaphase, when the mitotic spindle pulls apart the chromosomes and a subsequent re-organizational process of the nuclei takes place.
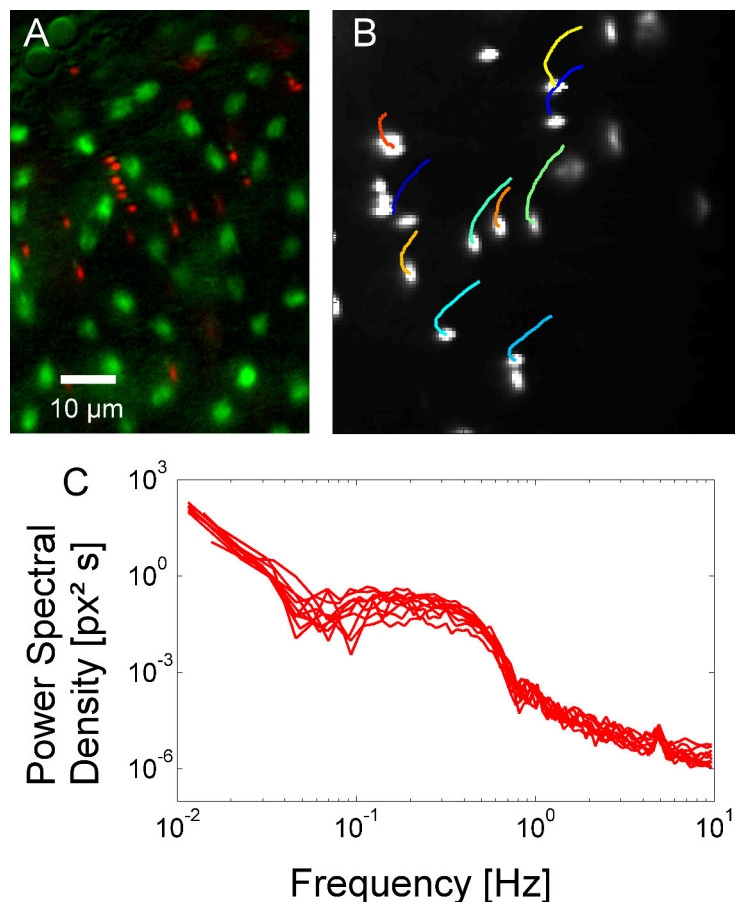
Figure 4.22: Motion trajectories and power spectral densities at anaphase
(A) Beads dispersed within the nuclear layer at anaphase. **(B)** Motion trajectories of the beads recorded over a time of 150 seconds. The particles move in a non-random and directed way. **(C)** Power spectral density curves of the shown beads. The curves show a deviation of the typically observed power law in the frequency range of 0.05 - 0.8 Hz.

Figure 4.22 A shows fluorescent beads dispersed within the nuclear layer at anaphase. Panel B displays the position trajectories of the probe particles. Already

by eye one can see the non-thermal, directed characteristics of their motion leading to a PSD with a clear deviation of the expected power law decay in the frequency range between 0.05 - 0.8 Hz.

Measurements below and above the nuclear layer

Just like inside the nuclear layer shear moduli were measured at different time points along the nuclear division cycle above and below the cortical layer of nuclei. Figure 4.23 A shows fluorescent images of the nuclear layer right after the time points when the microrheology measurements were done. The recordings were taken over one and a half nuclear division cycles ranging from interphase no. 12 to interphase 13 until the following anaphase.
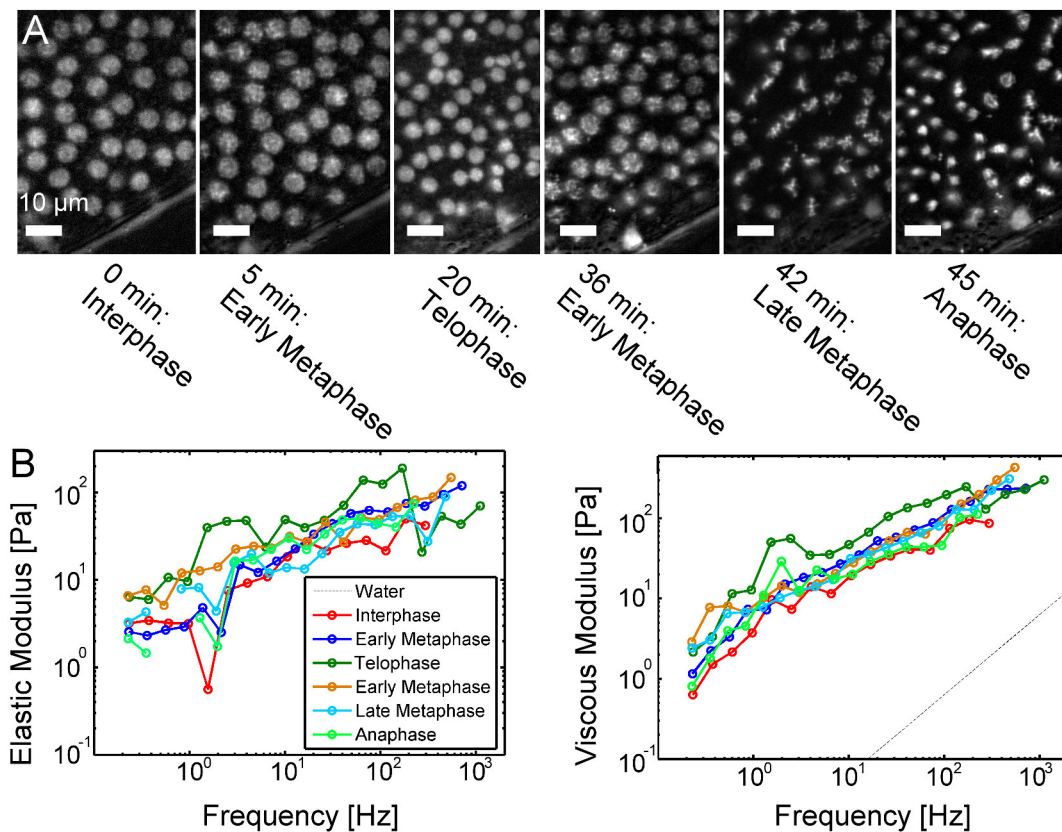
Figure 4.23: **Temporal variation of the complex shear modulus below the nuclear layer during a nuclear division cycle**
(A) Series of images taken at different stages over the nuclear division cycle. The time points and developmental stages of the division cycle are indicated. **(B)** Storage moduli (left) and the loss moduli (right) measured right before the time points shown in (A). The distance of the probe beads to the nuclear layer was storage moduli (left) and the loss moduli (right) measured right before the time points shown in (A). The distance of the probe beads to the nuclear layer was $z = -3.3 \pm 1.0 \ \mu m$ (mean $\pm$ SD).

The shear moduli in this measurement exhibit a larger variation than in the measurements taken within the nuclear layer but no clear trends can be stated. Again, an exception might be the recording taken at telophase where both, elastic
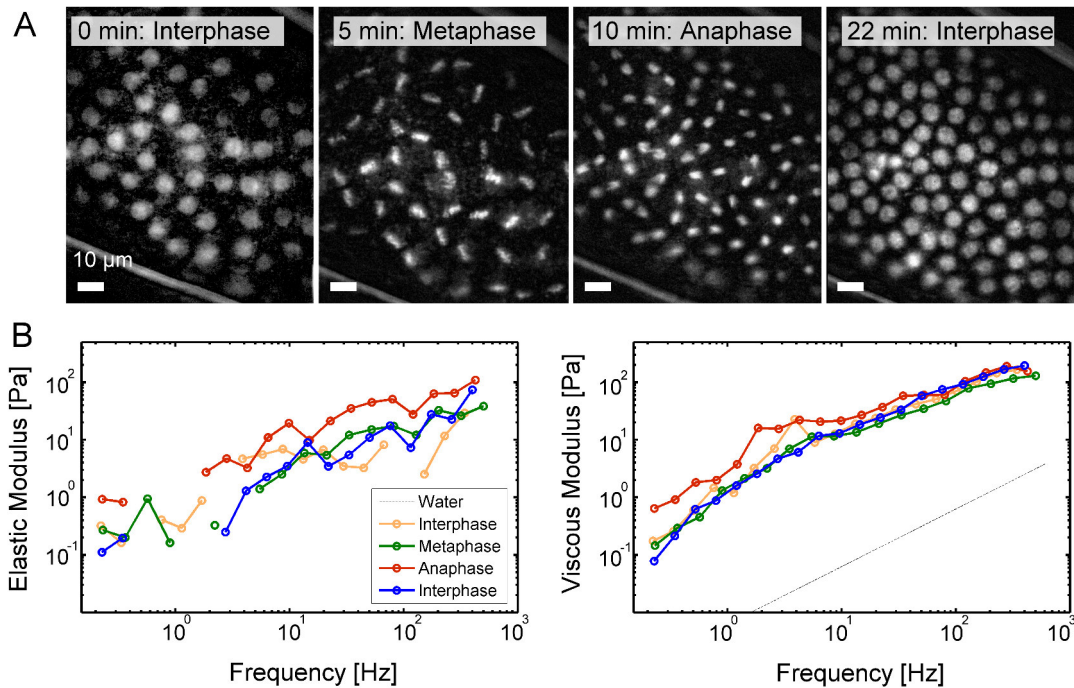
Figure 4.24: Temporal variation of the complex shear modulus above the nuclear layer during a nuclear division cycle
(A) Series of images showing the nuclear layer taken at different stages during the nuclear division cycle. Relative times and nuclear division stages are indicated. **(B)** Storage moduli (left) and loss moduli (right) measured right before the time points shown in (A). The distance of the beads to the nuclear layer was $z = 2.0 \pm 1.8 \ \mu m$ (mean $\pm$ SD).

and viscous modulus slightly exceed the curves taken at other division stages. The variation of the storage modulus is more pronounced than the variation of the loss moduli.

In figure 4.24 one can see the results of the same kind of measurement above the nuclear layer following the particle's motion over a nuclear division cycle which lasts 22 minutes. The moduli show no unambiguous temporal variation, except for a weak trend towards an increased viscous modulus around anaphase.

The low variation between the different stages includes no clearly measurable changes of the shear modulus from one interphase to next interphase, not inside the nuclear layer nor above or below it.

So far all data presented here was obtained by tracking single beads. To control if active motions did not already form a measurable part of the probe fluctuations, we looked for anti-correlations in the fluctuations of pairs of probe beads.
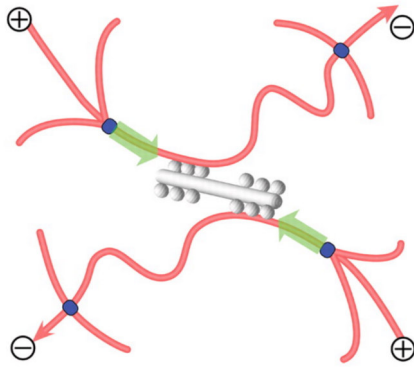
Figure 4.25: Schematic of an acto-myosin network
There are motor proteins like the depicted myosin minifilament which are able to exert forces within a network by pulling at two filaments. This force generation according to a force dipole can lead to anticorrelated motion of probe particles which are embedded in the surrounding network. Source: [61]

In this method of cross-correlation analysis the coordinate systems of the two beads are rotated in order to obtain the parts of motion which are along the connection axis and perpendicular to it. The cross-correlation spectrum of particle A with particle B is the Fourier transform of the cross-correlated signal

$$C_{\parallel}^{AB} = \int \left\langle u_{\parallel}^A(0) u_{\parallel}^B(t) \right\rangle \; exp\left(i\omega t\right) \; dt.$$

According to equation 3.4 we calculated this cross-correlated parallel PSD by multiplying the Fourier transforms of the single bead motions parallel to the connection axis with each other. In equilibrium the motion of two particles are positively correlated [63–65]. In a biological system out of equilibrium motor proteins can act as force dipoles in a crosslinked network (see fig. 4.25). In-vitro studies on actomyosin networks have stated anticorrelated motion of probe particle pairs due to this non-equilibrium activity [61]. Figure 4.26 shows exemplary curves and the results of the two-particle analysis from the data recorded in the embryo: Panels A and B show the Fourier transform of the cross-correlated motion along the connection axis of two particles over frequency ('cross-correlated parallel PSD'). The exemplary curve is logarithmically binned in frequency and corresponds to a positively correlated motion since its values are mainly positive. This dataset was recorded inside the embryo at interphase below the nuclear layer $z = -3.5 \; \mu m$. The interparticle distance was $d = 5.6 \; \mu m$. The curve follows a power law with a slope of -2. The blue curve in panel B shows the positive values of the cross-correlation PSD, whereas the red curve shows the negative values corresponding to a correlated and anticorrelated motion, respectively. The anticorrelated motions are not shown in the upper graph due to the logarithmic scale. Figure 4.26 C and D show the same type of graph but for a dataset exhibiting uncorrelated motion. The data points in the semilogarithmic plot scatter around zero. The interparticle distance is $d = 4.8 \; \mu m$. Data was recorded below the nuclear layer $z = -4 \; \mu m$.

In order to quantitatively distinguish signals with positive, negative or no correlation the number of positive and negative values of the cross-correlated parallel PSD was determined by counting them in the frequency range of 0.1 - 300 Hz.
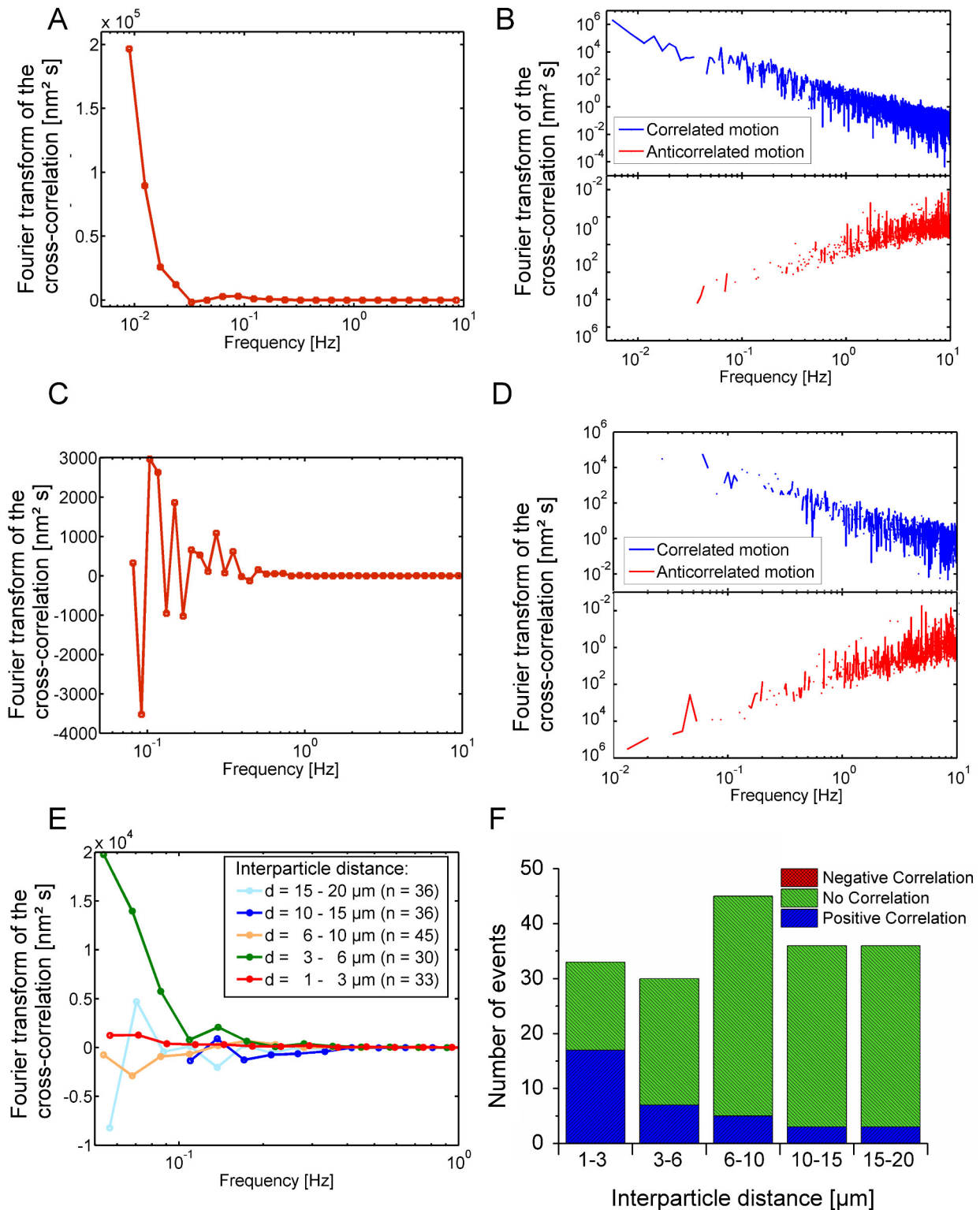
Figure 4.26: Exemplary two-particle correlations at different interparticle distances
(A) An exemplary cross-correlated parallel PSD of a positively correlated motion in a semilogarithmic plot. **(B)** Same dataset as in (A) in a double logarithmical plot without any binning. **(C)** The cross-correlated motion spectrum of an exemplary dataset in a semilogarithmic plot shows uncorrelated motion: the data points scatter around zero. **(D)** Same dataset in a double logarithmic plot shows positive (blue) and negative (red) values. **(E)** Averaged curves of the cross-correlated motion spectrum for different interparticle distances (n: number of curves taken into account). **(F)** For each curve at a certain interparticle distance of the cross-correlated PSD the number of positive and negative data points was counted. If at least 70% of the points were positive (negative) the curve was classified as positively (negatively) correlated.

If these numbers made up more than 70% of the total numbers of data points, the signal was taken to be correlated or anticorrelated, respectively. Figure 4.26 F displays the result of this evaluation for different interparticle distances. Just like it was found in actomyosin networks the positively correlated events occur most often at small distances and its number decay with interparticle distance. In contrast to Mizuno *et al.* [61] we did not see any negative correlation at any interparticle distance.

Figure 4.26 E shows averaged cross-correlation spectra at a certain interparticle distance. For the distances $1 - 3$ μm and $3 - 6$ μm a positive correlation is visible, the rest of the curves exhibits an uncorrelated behavior. The magnitude of the correlation spectrum reflects the material properties probed between the beads. Anti-correlated motion would have been a sign for non-equilibrium activity. This sign is lacking here, supporting the picture of dominantly passive mechanics in the targeted frequency window.

4.9 | **Control experiments**

Control experiments were performed to check if and how much inherent tracking noise or surface interactions of the probe with the surrounding medium might have influenced presented measurements.

Static and dynamic errors

To estimate the noise inherent in our measurements we injected beads into the embryo as usual but then chemically fixed embryos with formaldehyde in order to immobilize and record them at comparable conditions like in the experiments in living embryos. Figure 4.27 shows the results of position tracking accuracy (B) and position PSD (A).
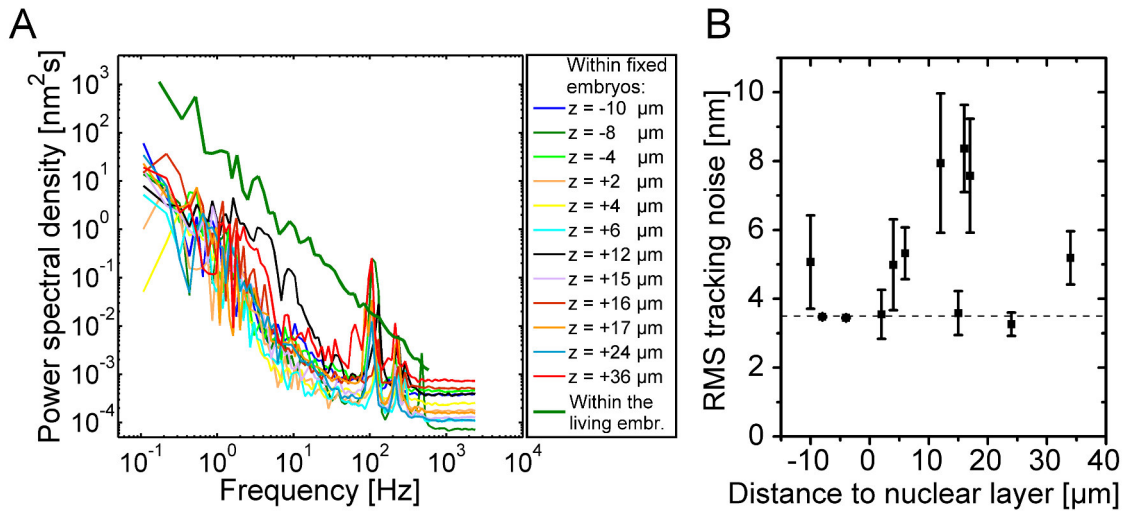
Figure 4.27: Noise floor and tracking accuracy within the embryo
(A) Position PSDs for beads at different distances z to the nuclear layer measured within fixed embryos. **(B)** RMS tracking noise measured inside the embryo for different distances to the nuclear layer. Embryos were fixed after bead injection and imaged at a sampling rate of 16 kHz. Dashed line shows the tracking accuracy for surface-attached beads (see fig. 3.11. Error bars: SEM of several beads recorded in the same plane.

Compared to surface-attached beads (dashed line, fig. 4.27 B), the tracking accuracy becomes slightly worse. We did not see a dependency of the tracking accuracy on the distance to the nuclear layer. The variation of the noise might be due to variation of signal-to-noise ratios with out of focus signals.
In general the power spectral density of a particle's motion measured with video microscopy contains two kinds of errors [66]:

$$C(\omega) = \left\langle |\bar{x}^*|^2 (\omega, \sigma) \right\rangle = sinc(\omega\sigma/2)^2 \times \left\langle |x^*|^2 (\omega) \right\rangle + \left\langle |\bar{\chi}^*|^2 (\omega) \right\rangle$$

$C(\omega)$ is the measured PSD and $\left\langle |x^*|^2 (\omega) \right\rangle$ is the true PSD (the bar and star indicate measurement average and Fourier transform, respectively). The finite exposure time σ in video-based microrheology causes a 'dynamic' error which leads to the sinc factor in the equation above. For our measurements, the exposure time is equal to the frame interval. The dynamic error becomes relevant at high frequencies. Due to our truncation of the PSD (see fig. 3.8) and the shear modulus (see fig. 3.9) I discard these high frequency parts. For the measurements presented in this thesis the maximum displayed frequency is approximately 1400 Hz. With a shutter time of 12.5 ms, the value of the sinc function at this frequency is greater than 0.9, i.e. the error is less than 10 %. The optical resolution of the setup in conjunction with the finite photon counting rate causes a random fluctuation χ of the position signal, which is also called 'static' error. Its value $\left\langle |\bar{\chi}^*|^2 (\omega) \right\rangle$ is estimated by the PSD noise floor at high frequencies shown in (A). Over a wide frequency range, the overall noise floor has values about two orders of magnitude below the actual rheological data measured within a living embryo (thick, green curve). The variance between particles within one section, even in the same embryo, (see fig. 4.10) far exceeds these two error sources, hence they are not further considered.

Bead passivation

To ensure that no surface interactions between probe particles and their surrounding influenced our measurements we performed control experiments with passivated beads. Therefore, the same tracer particles, but in a different color , were passivated by covalently binding PEG (Poly(ethylene glycol) methyl ether amine) chains to the surface following a protocol described in [67]. Green fluorescent beads were passivated with PEG whereas red fluorescent microspheres remained untreated, i.e. with a COOH functionalization.
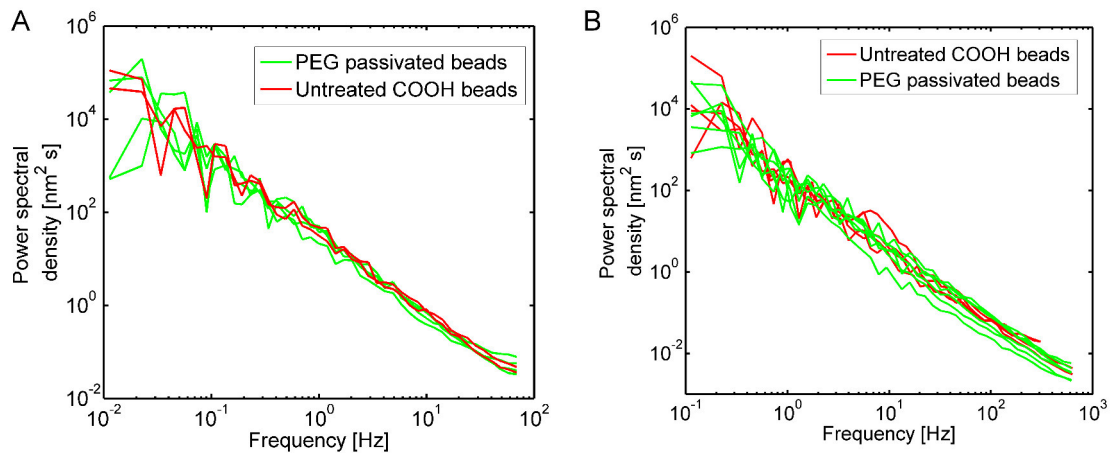
Figure 4.28: Comparison of position PSDs of passivated and untreated probes
(A) (A) Position PSDs recorded from PEG passivated and carboxylated beads distributed within the nuclear layer ($z = 0$ μm), at a sampling rate of 1500 Hz. **(B)** A set of PSD curves measured inside the yolk ($z = 16$ μm), sampling frequency 1500 Hz. Both exemplary data sets show no clear deviation of particle fluctuations between untreated and passivated beads.

Passivation of beads was confirmed by observing a fluorescent BSA absorption of less than 10 % compared to the untreated case. Then both kind of probes were injected into the same embryo. That way differences in particle fluctuations could be measured and directly compared within the same plane inside the same embryo. Figure 4.28 shows a set of exemplary curves for passivated and untreated probes. We quantified their fluctuations by integrating the PSD in the range of 25-300 Hz just like described in the previous sections. Beads were taken to be localized in one section if their distance along the optical axis was smaller than 5 μm. In-plane inhomogeneities were neglected. We imaged beads in the region of $z = -2.3 \cdots 27.4 \ \mu m$ and found only a marginal difference between the fluctuations of the two kind of probes: An average over all measured beads ($N_{PEG} = 29$, $N_{COOH} = 30$) within 16 embryos showed that the passivated probes fluctuated only 18 % $\pm$ 11 % more (mean $\pm$ SEM) than the untreated microspheres. That means that our formerly used untreated beads gave valid results, which might only weakly were influenced by effects due to chemical/electrostatical surface interactions.

<div align="right">

Summary and discussion | 4.10

</div>

Several approaches have been used to measure the mechanical properties of cells. Probing the response of adherent cells from the outside [68, 69] typically results in elastic moduli in the kPa range, reflecting the elastic behavior of the dense actin network of the cortex [70, 71]. Some experiments have addressed the elastic response of suspended rounded cells [72, 73] to external forces, showing relatively low stiffness, likely to still be dominated by the actin cortex. Only a few studies have directly addressed the mesoscale viscoelasticity of intracellular networks and the cytosol [2, 56, 58, 74–77].

Oocytes and early embryos are likely to not be comparable to cells in later stages of development in any case, due to their typically large size and differing internal structure. Reported measurements of the viscoelastic properties of the cytoplasm of cells in early C. elegans embryos found viscosity values similar to the ones we measured in Drosophila, while intracellular elasticity was found to be negligible [58]. Interestingly, measured diffusion constants of small molecules in syncytial Drosophila embryos [78] led to an estimate of microscopic viscosity of ~4 mPa s much lower than our measurements of mesoscopic viscosity. Here, we show that microtubules rather than actin filaments contribute to the viscoelastic response of the embryonal cytoplasm in the Drosophila embryos, more strongly near the cortex where the microtubule concentration can be seen to steeply increase.

In order to obtain shear moduli from fluctuation data, the fluctuation-dissipation theorem has to hold. In the approach presented in this chapter we assumed that the measured probe bead fluctuations were thermally driven. But depending on cell geometry, non-equilibrium fluctuations caused by active force generators can greatly complicate the interpretation. They will exert forces to the probe particles leading to fluctuations, which add to thermal fluctuations, violate the fluctuation dissipation theorem [75, 76] and propagate into the obtained shear modulus. The typical behavior of the motor protein's activity (namely a slow build up of tension with a subsequent sudden release) can change the spectral characteristics of a particle's motion in an elastic confinement and can, for example drive fluctuations that look very similar to thermal motions in a viscous medium [14, 79, 80]. Studies have shown, though, that non-equilibrium fluctuations tend to dominate in cells in a frequency range below 10 Hz [14, 61, 81]. Since we also tracked probe beads at higher frequencies, where the fluctuations will be purely passive, it is likely that we did not mistake active for thermal fluctuations. Furthermore, the approximate assumption of thermally driven fluctuations may still be valid, since the lack of a strong elastic cytoskeleton also means that motors cannot generate and transmit forces very efficiently. This is supported by the lack of anticorrelated motion of bead pairs which we found for all measured interparticle distances and by the lacking effect of myosin inhibition.

Moreover, this point of view can be fleshed out by the low variation of the shear modulus during the nuclear division cycle indicating the active processes happen slowly and are too weak to be measurable with our approach. The only non-equilibrium ac-

tivity we could state happened during separation of daughter nuclei in anaphase. It might be that an enhanced non-equilibrium activity can be found within the region close to the cortex, where actin dominates the cytoskeleton. With the experimental conditions introduced here we were most likely not able to enter the fine actin mesh-work with our beads of 1 μm diameter. It might be an interesting project for the future to address these actin-rich regions with smaller beads or extended rheological probes like carbon nanotubes [14]. Another follow up investigation on the work presented here could be the use of an active microrheology approach and combine it with the passive microrheology method we used in order to determine non-equilibrium fluctuations [61]. Since the yolk in the center of the embryo strongly scatters light normally used active microrheology techniques which depend on an interferometric detection through the embryo won't be possible. One would need to install, for instance, a back-scattered light detection [82] or synchronize the high-speed camera with beam steering optics (e.g. an acustooptical deflector) to sinusoidally move an optical trap [83, 84].

Another possible caveat regarding the values we obtained for the shear moduli is that one-particle microrheology can both under- and overestimate shear moduli in the presence of semiflexible filaments due to depletion and local non-affinity effects [57, 85]. Furthermore, chemical or electrostatic surface interactions can alter the absolute measured values of the shear modulus leading to a deviation compared to bulk values measured by (macro-) rheometers. However, our control experiments with PEG passivated beads show effects due to absorption and binding to molecules to be negligible. Regardless these considerations the scaling behavior of the frequency dependent shear modulus is independent of these effects. The established method to avoid steric and surface interaction problems is two-particle microrheology [55, 63, 65, 85]. But since two-particle microrheology is much noisier it involves extensive ensemble- and time averaging. Many datasets have to be averaged to get some smooth enough, i.e. meaningful curves. Averaging is favorably done on the raw data level (i.e. after cross-correlation) to prevent noise propagation through the analysis steps. The magnitude of the cross-correlated signal depends on the distance with 1/r making it necessary to average many particle pairs at the same distance. That is why this approach is not feasible in the rather inhomogeneous and rapidly developing embryos.

Carbon nanotubes as fluorescent probes inside syncytial *Drosophila* embryos | 5

In 1991 carbon nanotubes (CNT) were discovered by chance with an electron microscope in a sample which had been exposed to an arc discharge between carbon electrodes [86]. Soon after the discovery of multi-walled carbon nanotubes, single-walled nanotubes (which I will speak about in the following) were found. In the recent years their outstanding mechanical and electrical properties [87, 88] have drawn much attention. Single-walled carbon nanotubes attracted interest in the fields of biophysics and life sciences when they were found to have an intrinsic fluorescence [89]. This property made them a potential candidate for use as fluorescent markers. Basic principles regarding this application will be discussed in the following.

Optical properties of carbon nanotubes | 5.1

Carbon nanotubes can be thought of as a rolled up graphene sheet (see fig. 5.1 A). According to the roll-up vector $\vec{C_h}$, a CNT has a certain lattice structure, called chirality, and a certain diameter on the order of a nanometer. $\vec{C_h}$ is expressed in multiples of the basis vectors of the lattice $\vec{a_1}$ and $\vec{a_2}$. Hence, each class of nanotubes is named by a pair of integers. The remarkable optical properties of CNTs can be understood on the basis of the properties of graphene, which is a semi-metal, i.e. at the Fermi level conduction and valence bands touch only at one point (see fig. 5.1 B). Due to the finite diameter of the tube the translation invariance of the lattice does not hold anymore and the electronic wave vector perpendicular to the tube axis becomes discrete $k_\perp = i \cdot 2\pi/L$ with L is the circumference and $i = 1, 2, .., N$. In order to calculate the density of states, one cuts the electronic band structure of graphene along these lines (called *zone-folding*, see fig. 5.1 C). Diameter and chirality of $k_\perp$ determine distance and orientation of the lines with respect to the Brillouin zone. If the point K is included in these sub-bands the CNT will be metallic (in one third of the cases) and otherwise semiconducting. The density of states exhibits Van-Hove singularities [90] due to extrema in the band structure (see fig. 5.1 D). Energy absorption can lead to the formation of an exciton in these bands [91, 92] and some recombination paths are radiative. The most studied transitions are the second optical transition E_{22} for excitation and the E_{11} transition for emission.
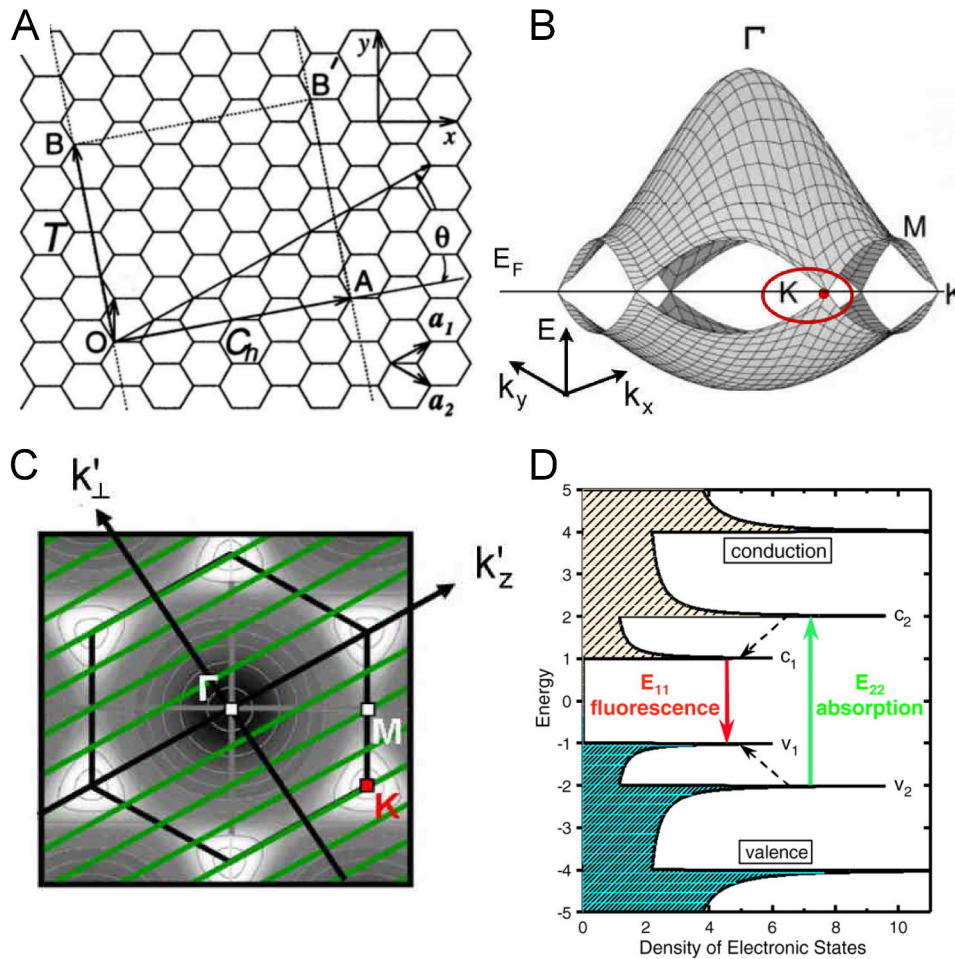
Figure 5.1: Electronical structure of carbon nanotubes
(A) A carbon nanotube can be thought of as a rolled up graphene sheet. By connecting the points A and O as well as B and B' one obtains a self-contained tube with its axes along the translation vector $\vec{T}$. The vector $\vec{C_h}$ is called a chiral vector and determines the chiral angle θ and the diameter of the tube. Source: [93] **(B)** 2D dispersion relation of graphene. Valence and conduction band touch at the Fermi energy only at the points K. Source: [94] **(C)** Projection of the valence band in the Brillouin zone. The green lines indicate the density of states for a carbon nanotube due to its finite diameter. Source: [94] **(D)** The density of states exhibits Van-Hove singularities. Some of the transitions between these singularities are radiative leading to fluorescence. Source: [95]

In 2002 O'Conell *et al.* [89] showed that CNTs do exhibit an ability to fluoresce. According to their chirality CNTs differ in their absorption and emission spectra (see fig. 5.2). CNTs have a large Stokes shift. They can be excited in the visible and near-infrared range and fluoresce in the near-infrared range of 900 nm - 1400 nm [96, 97]. This property makes them a particularly interesting fluorescent marker for biological studies since autofluorescence of biological tissue and cells is strongly decreased in this wavelength window [98]. So far many single-molecule *in vivo* tracking experiments have suffered from a bad signal-to-noise ratio caused by high background signal. Carbon nanotubes seem to be a promising solution to this. Besides their spectral advantages, they exhibit, in contrast to organic dyes or quantum dots, a lack of fluorescence intermittency and negligible photobleaching [91, 97, 99, 100]. This is a useful property for overcoming the short recording times of conventional fluorophores, due to blinking and bleaching which are typically on the

order of seconds. Moreover, CNTs absorb and emit along their tube axis [101, 102] which potentially allows for detection of the tube's orientation, too.
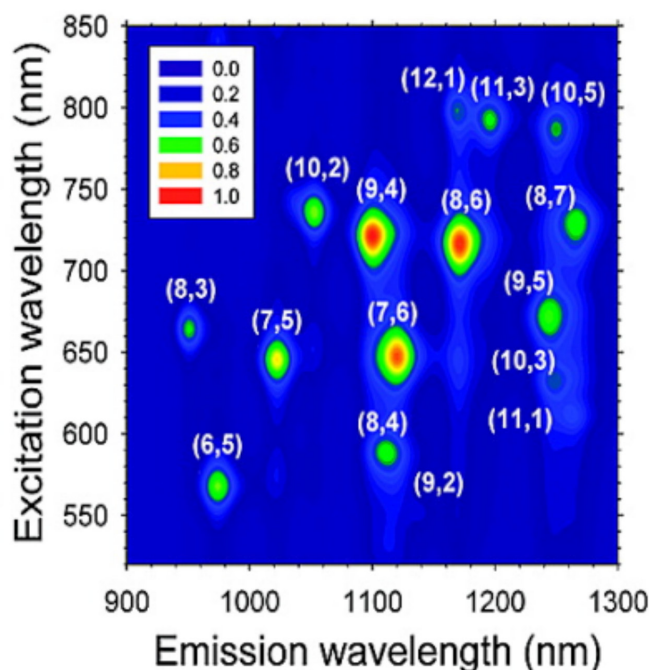
Figure 5.2: Photoluminescence map of carbon nanotubes
The 2D photoluminescence map shows the fluorescence intensity at varying excitation and emission wavelengths. The several distinct peaks correspond to carbon nanotubes with different chiralities determined by a pair of integers (m,n). Single-walled carbon nanotubes were suspended with SDBS (see text). source: [97]

Photoluminescence of CNTs is based on the formation and annihilation of an exciton. Decay rates are fast, which leads to short lifetimes in the order of 100 ps [103]. Thus, high illumination intensities can be used to further increase the fluorescence signal of the particles. The excitonic diffusion length is ~90 nm which leads to a strongly diminished fluorescence for shorter CNTs [91, 104].
The carbon nanotubes used in this work ranged from 100 - 300 nm in length for the tracking experiments and up to a few microns for the CNTs characterization experiments. CNTs have a persistence length of 10 μm, and hence can be considered stiff rods for our experiments [105, 106].

# Solubilization and functionalization of carbon nanotubes | 5.2

An important step towards proving and detecting the intrinsic fluorescence of carbon nanotubes was the proper solubilization of individual tubes [89]. As in graphene, carbon atoms have an sp^2 hybridization in the carbon nanotubes. Besides the three σ bond in plane the fourth 2p orbital stick out of the plane and forms a delocalized

π electron system. The hydrophobic CNTs tend to form bundles where they interact with π-π interactions which leads to high Van-der-Waals energies per contact length. These CNT bundles were reported to be non-fluorescent, particularly, that metallic CNTs quench the fluorescence of semiconducting ones [89, 107]. CNTs are almost impossible to solubilize in conventional solvents. Finally a stable solution of CNTs in water was obtained by means of surfactants in combination with ultrasonic treatment [89]. Established surfactants are SDS, SDBS, or NaDOC, which form a micelle around the nanotube (see fig. 5.3). Alternative ways to disperse CNTs is
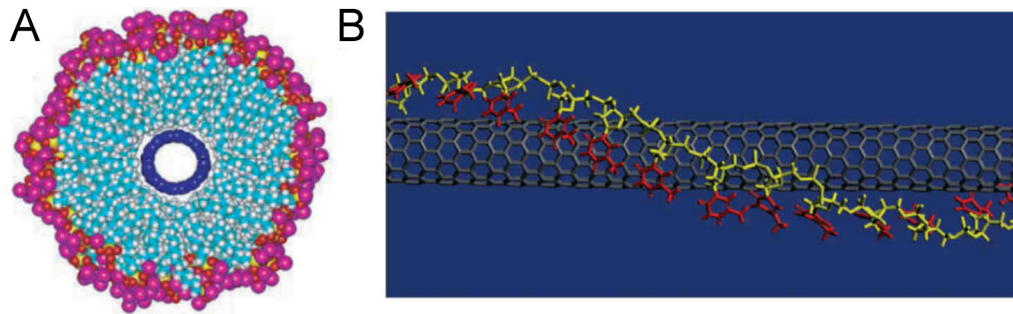
Figure 5.3: Solubilization strategies for carbon nanotubes
(A) A successful way to disperse individual carbon nanotubes in water is the use of a surfactant. The image shows a molecular dynamics simulation of amphiphilic SDS molecules which form a micelle around the hydrophobic carbon nanotube. [89] **(B)** Alternatively a CNTs can be solubilized by peptide chains or DNA fragments which adsorb onto the surface of the nanotube. The image shows a molecular dynamics simulation of a proposed DNA conformation wrapping around a carbon nanotube with its bases (red) in contact with the nanotube. [108]

to let peptide chains adsorb to their surface [97] or to wrap the tubes with single- or double-stranded DNA [108, 109]. Quantum efficiency strongly depends on the CNT surface coating, e.g SDBS-dispersed nanotubes have a quantum yield of about 10 %, whereas DNA-wrapped tubes only half a percent [110, 111]. Nevertheless, solubilization by DNA and peptides has the advantage of biocompatibility, thus, so far DNA-CNT complexes were used in *in vivo* experiments [14, 112, 113]. Peptide coated CNTs seem an interesting candidate for biocompatible probes with enhanced quantum yields [97, 114]. It is interesting to note that surface coatings have an effect on the spectral properties of CNTs. Moreover, the dielectric environment is able to shift the absorption and emission spectra of nanotubes. Another possible application in the life sciences arises from this phenomenon, namely using them as local chemical sensors [115, 116].

Functionalization with a Halotag®

Besides the afore mentioned demand for a long-term photostability, an *in vivo* fluorescent marker also must allow for intracellular targeting. While genetically encoded fluorescent proteins like GFP intrinsically have a specific target, the targeting of exogenous probes remains challenging [117, 118]. To overcome this challenge, the Halotag® system was developed. Halotag® is a 34 kDa monomeric protein tag which is genetically fused to the protein of interest. It has a structural binding pocket for a synthetically produced ligand. Upon binding, the Halotag® cleaves and

replaces carbon-halogen bonds in the Halotag® ligands (halogenated aliphatic hydrocarbons) to form a covalent bond [119]. The advantage of this approach lies in the exchangeability of the ligand. One Halotag® can be used for different ligands. Further advantages are that the bond between the Halotag® and ligand is rapidly formed under physiological conditions, it is highly specific, and irreversible. For
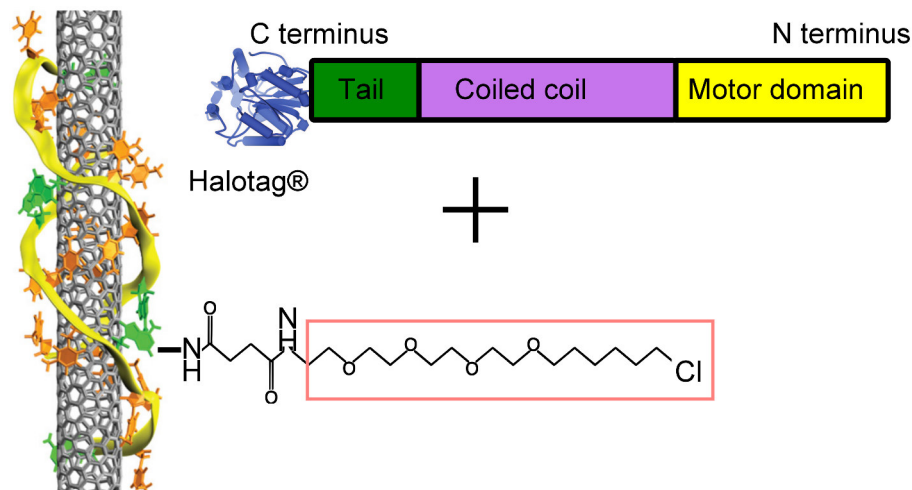
Figure 5.4: CNT-kinesin-5 targeting by a Halotag®
A Halotag® was genetically fused to the N terminus of the kinesin-5 Klp61F. The Halotag® ligand was attached to the amine group at the 5' end of the DNA which wraps the carbon nanotube. The red box highlights the binding part of the ligand. Adapted from [14, 119, 120]

our experiments the Halotag® was fused to kinesin-5 and expressed in *Drosophila* embryos. The ligand was coupled to the DNA-wrapped nanotubes. On this way motor proteins could efficiently be targeted with carbon nanotubes recently [14].

Experimental methods and materials | 5.3

The carbon nanotube raw material used in this work has kindly been provided by the Rice University, Texas. The CNTs were grown in the High Pressure Carbon Monoxide Reactor (HiPco) by exposing iron clusters to a flow of carbon monoxide at high pressures and temperatures (p(CO)=30 atm and T=1050 ℃) [121]. Under these conditions, CNTs of different lengths, diameters and chiralities assemble. Thus, the sample I used is a mixture of different chiralities of nanotubes with the main constituents being (6,5) nanotubes.

CNTs were imaged with the setup described in chapter 2. Both the Zeiss and Nikon objectives were used to image the sample onto the near-infrared sensitive InGaAs camera or spectrometer. The sample was excited with the 561 nm laser and the titanium-sapphire laser. Fluorescence light was filtered with a 900 nm long-pass filter.

Surfactant-coated CNTs were used for imaging, bleaching and spectroscopy experiments (for details see *Lab protocols, materials and methods* in the Appendix).

DNA-wrapped CNTs were used for tracking experiments inside *Drosophila* embryos.

Raw HiPco material was added to the DNA solution, sonicated on ice for two hours, centrifuged and filtered. Single-stranded DNA, namely d(T)30 oligonucleotides with an amine-terminated group on the 5' end were used for dispersion [108]. The Halotag® succinimidyl ester ligand (O4, Promega) was linked to the amine group of the CNT-ssDNA complex. For a detailed protocol of CNT-Halotag® ligand preparation see [14], *Supplementary materials*.

The Promega Halotag® was fused to the C terminus of the Clp61F motor protein (see fig. 5.4) and expressed in genetically modified *Drosophila* flies (for details see *Lab protocols, materials and methods* in the Appendix).

5.4 | **Carbon nanotubes as fluorescent probes**

I was able to observe and measure the intrinsic fluorescence of surfactant-dispersed CNTs with our preparation methods and imaging setup. Figure 5.5 shows many surface-attached CNTs dispersed with the surfactant SDBS. The inset shows a mag-
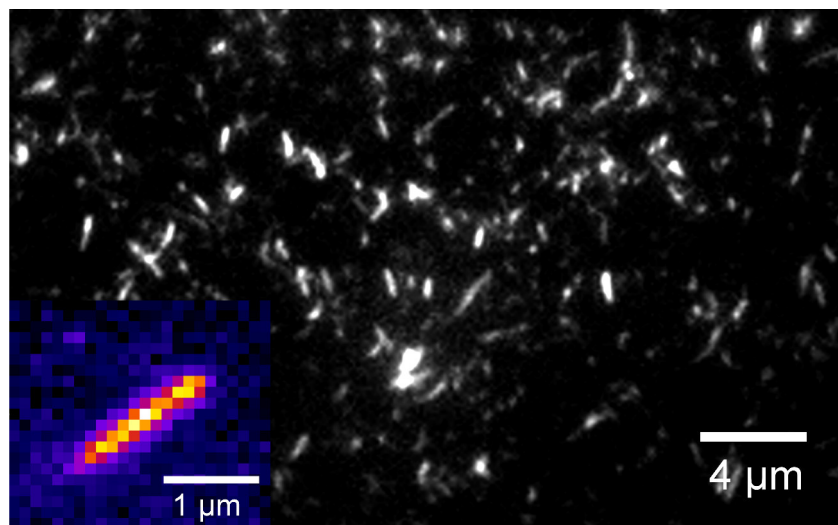
Figure 5.5: Fluorescing carbon nanotubes on a glass surface
Surface-attached fluorescing carbon nanotubes individually dispersed with the surfactant SDBS.
Inset: Magnified image of a carbon nanotube displayed with a fire LUT.

nified image of a typical CNT of a length of approximately 1.5 μm. At this length a CNT appears to be a stiff rod. Figure 5.6 shows a typical spectrum of an individual CNT attached to a quartz slide. Glass cover slides were replaced by quartz slides because of the high fluorescence background of glass in this wavelength range (see section 2.3). The CNT emission spectrum shows a distinct peak with a maximum at approximately 960 nm. All measured CNTs which fluoresced under illumination with the 561 nm laser or the titanium-sapphire laser exhibited emission spectra in this wavelength range with maxima lying between 950 nm and 1000 nm. This spectrum corresponds to (6,5) chirality nanotubes, as expected. When comparing the spectrum of CNTs attached to quartz and glass (see fig. 5.6 and 2.8) one sees not only a higher wavelength for the maximum of the emission spectrum but also

a broadening of the emission peak on glass. It is well-known that CNT spectra respond sensitively to changes in their dielectric environment. The broadening of the emission spectrum might be such a case.
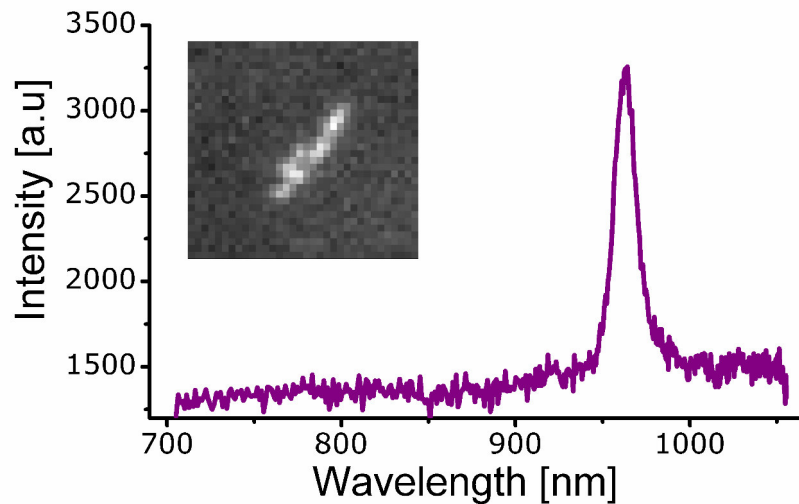
Figure 5.6: Fluorescence spectrum of a carbon nanotube
Fluorescence spectrum of a carbon nanotube attached to the surface of a quartz slide. The emission peaks at approximately 960 nm indicating a tube of (6,5) chirality. The inset shows the fluorescence image of the measured CNT.

In order to further characterize the fluorescent properties of CNTs, I measured their fluorescence intensity with respect to illumination power. Figure 5.7 displays the result of this measurement, showing that even at high powers of approximately 900 mW (corresponding to peak power densities of ~18.8 kW/cm^2) no saturation effects were visible.
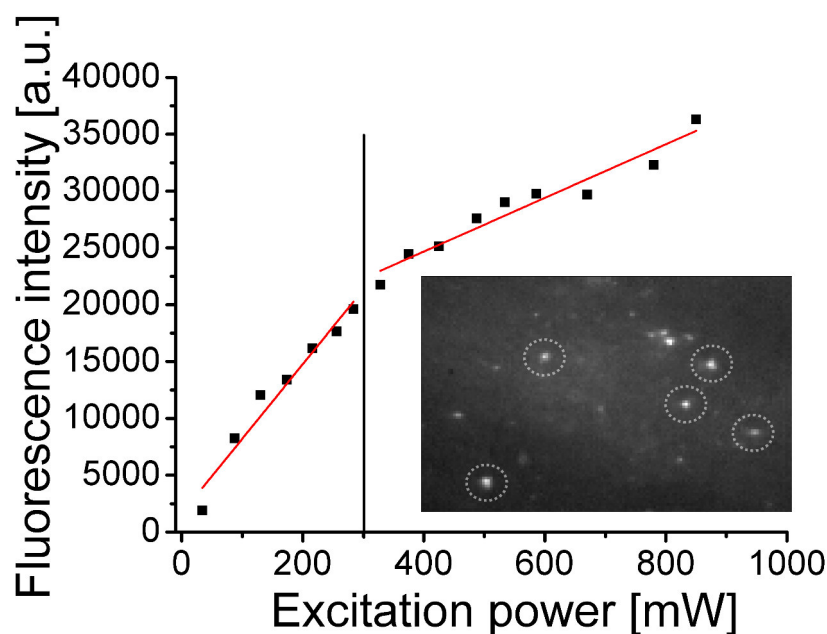
Figure 5.7: Relation of the emission and excitation intensity
Fluorescence intensity averaged over five CNTs (inset) for different excitation intensities. Up to an illumination power of 287 mW the 561 nm laser was used for excitation. Then the titanium-sapphire laser (wavelength: 789 nm) was used to additionally excited the CNTs (simultaneously).

The lack of saturation can be explained by the short lifetimes of the excited states, which make many fluorescent decays per time interval possible. The samples were exposed to the 561 nm laser up to an illumination power of 287 mW. Then the titanium-sapphire laser was used to additionally excite the CNTs. The black vertical line indicates the transition between the two scenarios. Linear fits within both regions exhibit different slopes due to different excitation probabilities of the nanotubes for wavelengths of 561 nm and 789 nm.
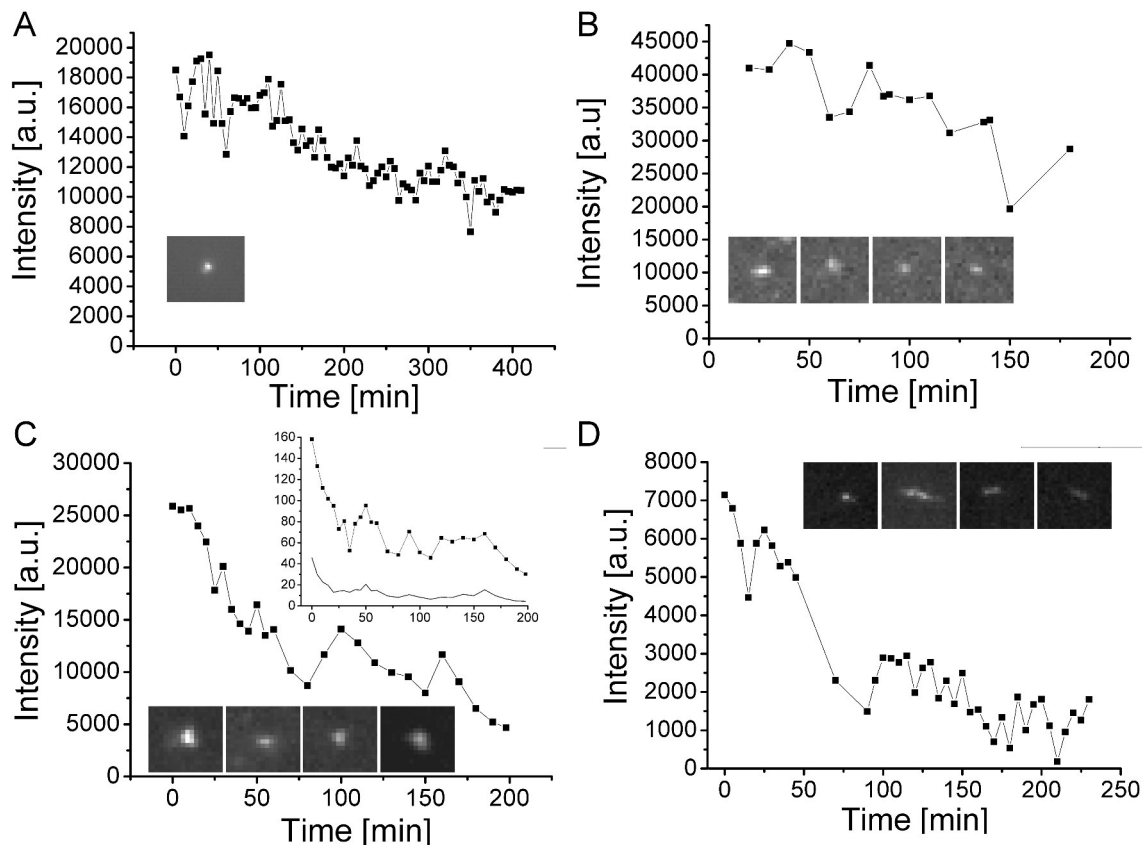
Figure 5.8: Bleaching behavior of carbon nanotubes
All curves show (background corrected) intensities of carbon nanotubes (insets: fluorescence images) over time under constant illumination. **(A)** SDBS-coated CNT embedded in an poly-acrylamide gel illuminated by the titanium-sapphire laser (emission wavelength 728 nm, illumination density 6.0 kW/cm^2) recorded with a Quantem EMCCD camera. **(B)** DNA-wrapped CNTs inside *Drosophila* embryos illuminated by the titanium-sapphire laser (emission wavelength 789 nm, illumination density 6.5 kW/cm^2) recorded with the Xeva InGaAs CMOS camera. **(C)** DNA-wrapped CNTs inside *Drosophila* embryos illuminated by the 561 nm laser (illumination density 6.2 kW/cm^2) recorded with the Xeva InGaAs CMOS camera. Upper inset: Maximum (uncorrected) intensity of nanotubes (solid squares) and surrounding background (solid line) averaged for the depicted CNTs. **(D)** NaDOC-coated CNTs embedded in an agarose gel illuminated by the 561 nm laser (illumination density 6.2 kW/cm^2) recorded with the Xeva InGaAs CMOS camera.

I illuminated CNTs for several hours to test their photo stability. In Figure 5.8 one sees four curves showing background-corrected intensity over time for four different experimental scenarios: I used different ways to disperse nanotubes (surfactants: SDBS and NaDOC or DNA strands), put them into different environments (embedded in a polyacrylamide gel or in an agarose gel or injected them into *Dro-*

sophila embryos), recorded their fluorescence with the Xeva near-infrared camera or a Quantem EMCCD camera (Quantem 512C, Roper Scientific) and illuminated them with the 561 nm laser or the titanium-sapphire laser. Embedding CNTs into aqueous gels has become a standard technique to provide an inert, immobilizing environment and has been used recently in optical measurements of single molecules [122, 123]. For the recordings inside fly embryos CNTs were injected. Some of them attached to immobile structures. So they could be measured under conditions close to an actual intracellular tracking experiment. Interestingly CNTs remained fluorescent even after four weeks of storing the sample.

The Xeva camera needs hours to cool down and equilibrate before an experiment. Though allowed this time to equilibrate, its sensitivity still changed over time, as visible in the background signal which is not constant over time (see upper inset of fig. 5.8 C). This is why two types of cameras were used, to make sure that this effect does not influence the results of the measurements. However, the message of the experiment remains: The curves in figure 5.8 reveal that a CNT's intensity attenuates over time. Findings from former studies [99], which stated no attenuation of intensity at all, could not be reproduced under my experimental conditions. Nevertheless, it looks like as if some of the curves would reach a plateau for longer times (A and B). The upper inset of figure 5.8 C shows the maximum intensity (averaged over the four depicted CNTs) of the nanotubes and the surrounding background. First of all it is obvious that the background fluorescence does not stay constant. Moreover, the fluorescence signal of the CNT persisted after three hours with values clearly above the background. To conclude, I found CNT's photostability not as high as stated in the literature but still highly photostable compared to organic dyes.

5.5 | Carbon nanotubes inside *Drosophila* embryos

In order to study the intracellular micromechanics of *Drosophila* embryos, we microinjected carbon nanotubes into early fruit fly embryos. As with injected beads, we found that carbon nanotubes did not spread widely inside the fly embryo but diffused rather slowly away from the point where they were injected. Thus, we chose the vertical injection geometry described in the previous chapter to place the CNTs close to the nuclear layer. They were injected into embryos expressing Halotag®-kinesin-5 and, as a control, into embryos with non-tagged motor proteins. The latter embryos expressed a fluorescent marker for the nuclei, whereas the first class of embryos did not. In this case the coverslip (identifiable by fluorescent particles in the glue) served as a reference plane for the Halotag® embryos. The histone-GFP expressing control embryos could be observed simultaneously with the NIR camera and in the green channel of the visible camera (see section 2.1). Here the nuclear layer served as a reference plane.
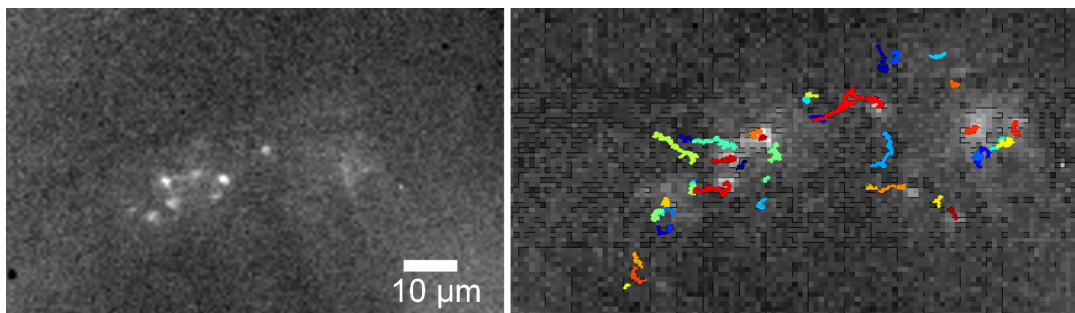
Figure 5.9: **Snapshots and motion trajectories of fluorescing carbon nanotubes inside fly embryos**
A fluorescence image of DNA-wrapped and Halotag®-functionalized carbon nanotubes inside *Drosophila* embryos (left) and their motion trajectories (right). CNTs were recorded 14 μm above the coverslip.

Figure 5.9 shows fluorescing CNTs inside an embryo. These recording were taken 14 μm above the surface of the coverslip. It shows the advantage of a CNT's near-infrared fluorescence: We can image them inside a living embryo with widefield microscopy. As in the chapters before, the position of fluorescing spots was determined by a center-of-mass estimator which turned out to be more robust than e.g. Gaussian fitting. The right panel of figure 5.9 shows motion trajectories of the particles which were obtained in this way.

Motion analysis of carbon nanotubes inside *Drosophila* embryos

In order to analyze the motion characteristics of CNTs, I calculated the mean square displacement (MSD) as a function of lag time for certain carbon nanotubes. Figure 5.10 displays three exemplary data sets recorded in control embryos and Halotag® motor-protein expressing embryos. The MSD curves of the first example (see fig. 5.10 B) follow a power law behavior with slopes of approximately one
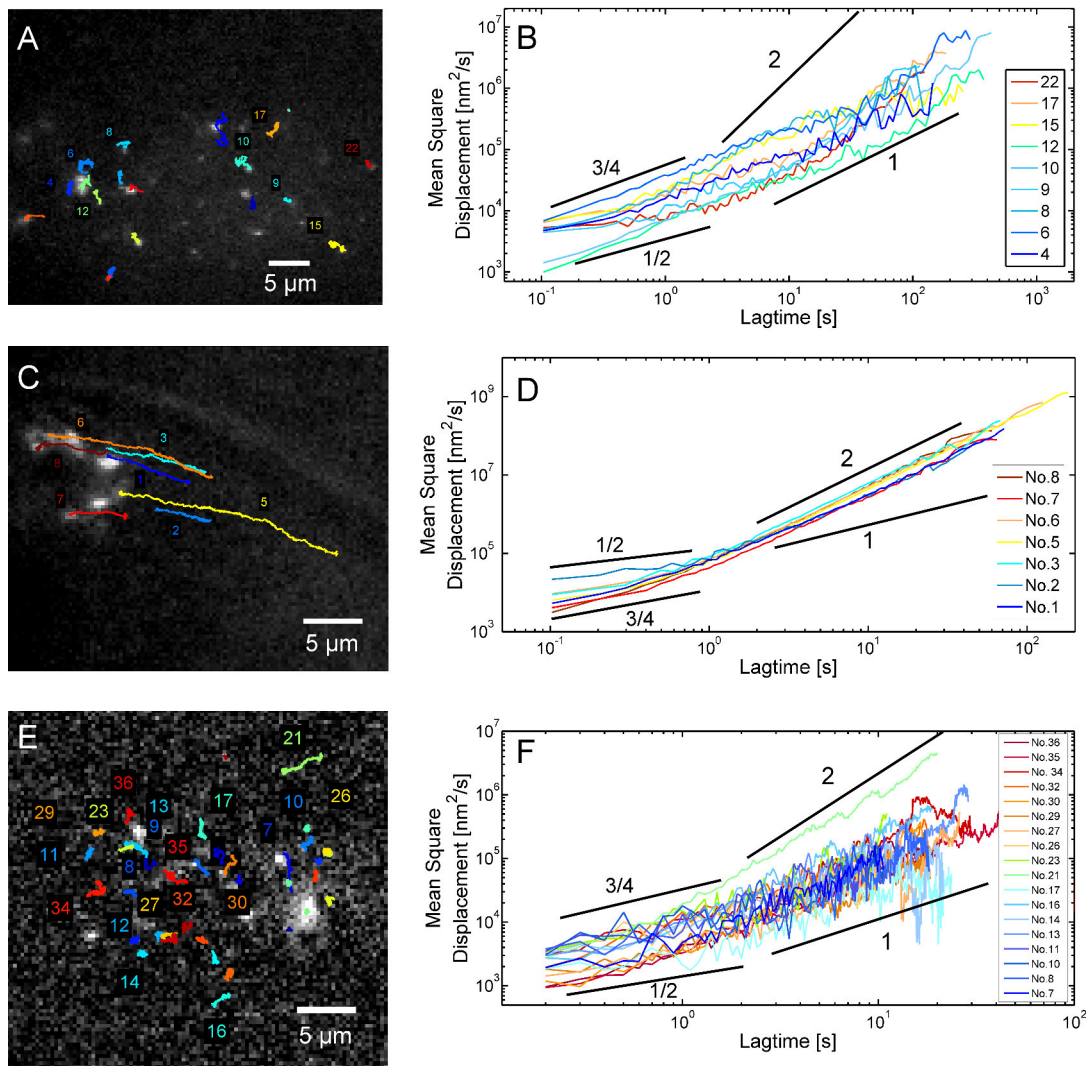
Figure 5.10: MSD analysis of injected carbon nanotubes
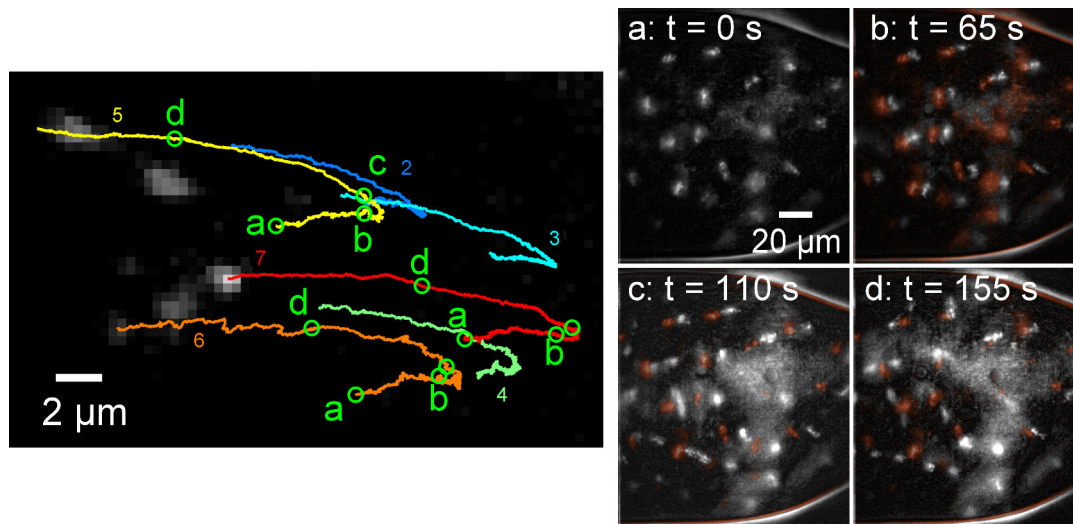**(A), (C), (E)** Fluorescence images of CNTs superimposed with their motion trajectories of the whole video. **(B), (D), (F)** Mean square displacement of certain CNTs shown in the left panels. Lines indicate different power law slopes. The upper and center panel shows data taken in control embryos inside the nuclear layer. The lower panel shows data taken in an embryo which expressed Halotag® motor proteins, recorded 11 μm above the coverslip, i.e. close to the nuclear layer.

and 3/4. This is expected for freely diffusing particles in a viscous fluid or in a viscoelastic fluid, respectively [124, 125].

The corresponding motion trajectories in panel A exhibit uncorrelated, i.e. not aligned movements of the CNTs. This is in stark contrast to the example shown in figure 5.10 C and D where trajectories are clearly aligned. The MSD curves correspond to a superdiffusive motion with a power law slope of two. This linear time dependence of motion can be seen in cases of directed motion, e.g. caused by transport processes of motor proteins but also in a drift caused by laminar flow [125, 126]. Since this data was taken in a control embryo and the motion trajectories are strongly correlated, the latter explanation seems more appropriate. These two examples demonstrate that different classes of motion, subdiffusive, diffusive and superdiffusive motion, are already present in the control sample. Interestingly, the

data shown in the center panel of figure 5.10 was taken at late interphase (at the onset of metaphase). I never observed this kind of pronounced flow in microrheology experiments using micrometer-sized beads as fluorescent probes, particularly not in interphase. Figure 5.11 focuses further on these kind of flow observations. The movement of CNTs and nuclei could be related to each other by simultaneously detecting them.

Figure 5.11: Carbon nanotubes recorded before, during and after nuclear division
Fluorescence image of CNTs dispersed in the nuclear layer of *Drosophila* embryos superimposed with their motion trajectories (left). **(a)** - **(d)** Snapshots of the nuclear layer before, during and after nuclear division (white). The first image (red) is superimposed on the latter ones to show nuclear movement over time. The four points in time (a)-(d) are marked at the motion trajectories by green circles.

The displayed data was taken in the same embryo like the one shown in figure 5.10 B, immediately afterwards. During this image series nuclear division took place. The panels (a)-(d) display fluorescence images of the nuclear layer at different times (white). The red features are the nuclei at $t = 0$ seconds superimposed on the later images in order to make their change of position visible. One can see the nuclei changing their shape (due to chromosome condensation) and forming mitotic spindles (c). By eye one can see the centers-of-mass of the nuclei, spindles, and daughter nuclei move with respect to their initial positions (red images), backwards and forwards. This motion can also be seen in the recordings of the CNTs (see left panel) which move backwards and forwards as well. The green circles on the motion trajectories indicate the points in time when the images of the nuclear layer (a)-(d) were taken. They serve as a time marker to show that the CNT's movement is correlated. In general flow can be, for instance, caused by leakage at the injection site. We here saw back and forth flows during nuclear division, which i.e. correspond to physiological relevant processes. This example is shown to illustrate how CNTs can potentially be used as stable fluorescent probes to study cytoplasmic flows in future.

Figure 5.10 E and F present data of CNTs injected into embryos expressing the HaloTagged motor proteins. In this example CNTs do not follow large-scale flows, their movement looks uncorrelated, but one of the trajectories seems less random (no. 21). The MSD of this trajectory show a directed motion for long lag times

following a power law behavior with a slope of 2, whereas the rest of the CNTs move only slightly superdiffusively with a slope close to one.

In order to further analyze this kind of directed motion, I measured displacement velocities for segments of 4 seconds and also plotted displacements over time, so-called kymographs. Figure 5.12 A shows track 21 from figure 5.10. Panel C displays the corresponding kymograph of the track which exhibits an extended period of directed movement, i.e. linear displacement in time with an estimated velocity of 326 nm/s. Panel B displays the velocity distribution of the segmented track (segment duration of 4 seconds) with a mean value of 385 nm/s. Other similar trajectories gave comparable numbers. Both velocity values clearly exceed what has been stated in literature: *In vitro* studies of *Drosophila's* kinesin-5 motors, Clp61F, measured velocities of the motor's motion relative to their underlying microtubules track of 11 nm/s [127].
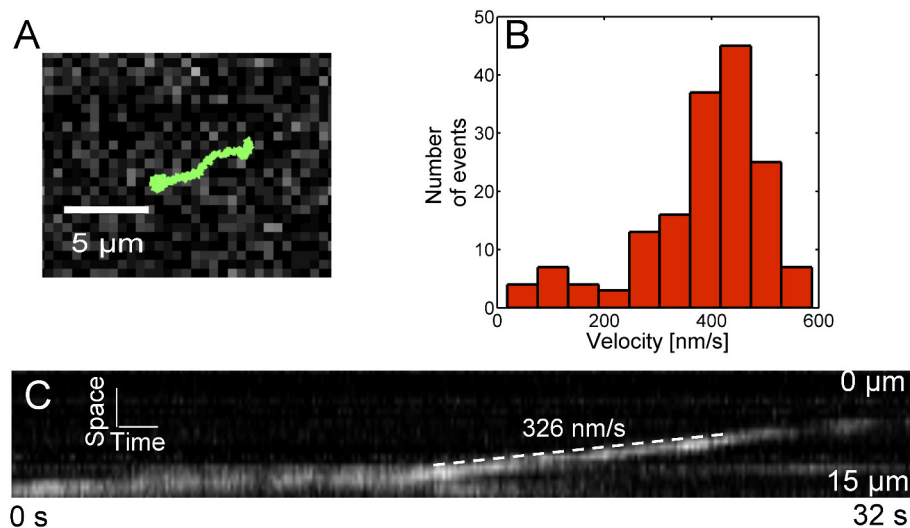
Figure 5.12: Velocity analysis of directed motion trajectories
(A) Trajectory no. 21 from figure 5.10 E. **(B)** 4 second segment velocity distribution with a mean speed of 385 ± 9 nm/s (mean ± SEM). **(C)** Kymograph for track no. 21. Dashed lines indicates a directed segment with the according speed.

Consequently, I conclude that the observed motion of track 21 (and other similar tracks) do not (exclusively) stem from the movement of kinesin-5 motors, though they are clearly non-diffusive and are unlikely to be caused by large-scale flows, as the cases shown in figure 5.10 C.

5.6 | **Summary and discussion**

Carbon nanotubes are promising fluorescent probes for long-term studies in cells and whole organisms. In summary, I was able to detect the intrinsic fluorescence of individually dispersed nanotubes. I measured the near-infrared emission spectrum of (6,5) tubes, the CNT predominantly being present in our sample, and confirmed that, most likely due to their short fluorescence lifetimes, high illumination intensities can be used to enhance the obtained signal. I determined the bleaching behavior of CNTs and found them to be less photostable under the tested experimental conditions than stated in the literature. This is surprising since most of the experimental conditions seem to be similar. Cognet *et al.* [91] found CNTs embedded in an agarose gel to fluoresce at a constant intensity over tens of minutes at illumination intensities of 100 W/cm². Heller *et al.* [99] measured DNA-wrapped CNTs at illumination intensities of 6.17 kW/cm² and found no change in emission intensity over ten hours. The authors did not mention how CNTs were immobilized and in which surroundings they were recorded. Only at illumination intensity densities about an order of magnitude higher than in my experiments researchers found that CNT exhibit a measurable bleaching behavior [128]. I performed experiments with CNTs illuminated at moderate power and attached to the surface of a cover slide, embedded in gels, and inside *Drosophila* embryos. Thus, it remains an open question where the attenuation of the CNT's intensity comes from. A possible explanation is an increased mobility/ reactivity of the CNT coating leading to dissociation from the nanotube. That might have partly led to a quenching of the fluorescence. Nevertheless, fluorescence remained visible after hours of high power illumination. This is comparable to what was found for quantum dots [129] and still exceeds typical lifetimes of organic fluorophores by orders of magnitudes. Thus, our sample will be appropriate for long time studies in biological environments.

I introduced DNA-wrapped (hence biocompatible) CNTs into early fly embryos by microinjection and tracked them several micrometers deep inside the whole living embryo with wide field microscopy. In control embryos I saw different classes of motion of CNTs: subdiffusive, diffusive and superdiffusive. The latter cases are very likely caused by large scale flows. Back and forth movements, as well as correlations of the CNT's movement with nuclear movement (which could be observed by simultaneously recording nuclear movements) indicate that the observed flows are not just flows due to leakage or drift but correspond to physiologically relevant processes. Following the methodology of our recent study on CNT tracking in spread cells [14], CNT were injected into genetically modified embryos which expressed kinesin-5 motor proteins with a Halotag® in order to attach CNTs to the molecular motors. In these embryos superdiffusive particle movements were recorded which were not caused by flows on the scale of several nuclear compartments (since close by particles exhibited diffusive behavior). Average velocities of these movements were in the range of 300-400 nm/s, about thirty times higher than expected for the targeted motor proteins [127]. A possible, but unlikely, explanation, on the one hand, is that CNT attachment to the motors failed and the observed motion is due to locally restricted fast flow fields. On the other hand, it might be that motors (and its at-

tached CNT) were bound to fast moving microtubules. In contrast to spread cells, microtubules have more free space to move and fewer anchoring points within the embryo. Furthermore, microtubules are molecular machines themselves, consuming chemical energy in the form of GTP to grow and they are known to restructure on large scales, e.g. during formation of the mitotic spindle [130, 131].

The experiments regarding CNT in fly embryos are preliminary, first steps on the way towards a better understanding of how single motor proteins act *in vivo*, on short timescales of milliseconds as well as long timescales on the order of minutes and hours. Moreover, it is of interest to investigate how the activity of single motors is spatially correlated. It is known that kinesin-5 agglomerates at the centrosomes. Hence, CNT tagged motors might function as stable and bright fluorescent markers to measure centrosome motion and its correlation at millisecond timescales in future projects.

Optical trapping of carbon nanotubes | 6

In 1970 Ashkin demonstrated that the motion of particles can be altered by optical forces. He proved this true for particles of micrometer size and for neutral atoms [132, 133]. This finding started two research fields, the cooling/ trapping of atoms (review see [134]) and the 3D trapping of micron-sized dielectric spheres by a single focused laser beam [135] (reviews of applications see [15, 16]).

For decades no research was reported on trapping particles at intermediate length scales. Svoboda and Block [136] were the first to successfully confine nanometer-sized particles twenty years ago. But only in the last decade, triggered by the accelerating advent of nanotechnology, has trapping of nanostructures been reported (review see [17]). Trapping forces based on electric dipole interaction energy scale with the particle volume [137], which makes it difficult to confine the motion of nano-objects. How trapping forces arise due to focused laser beams for objects much larger than the trapping wavelength are delineated in section 2.4. Trapping of atoms was accomplished by using enhanced optical responses near resonances. Both trapping in the nanometer range as well as resonance effects on trapping will be addressed in this chapter.

Optical trapping of particles in the Rayleigh regime | 6.1

Thorough calculations of trapping forces on small particles would need to solve the Maxwell equations with appropriate boundary conditions for a particle in a surrounding medium exposed to a trapping light field. But if the wavelength is greater than the size of the particle, the external electric field $\vec{E}$ can be assumed to be spatially constant along it, simplifying the calculation. From the total electromagnetic force on a charged particle $\vec{f_0} = q\left(\vec{E} + \vec{v} \times \vec{B}\right)$, with charge q, velocity $\vec{v}$, one can derive the force density[1] of a small volume element according to Rohrbach and Stelzer [138]

$$\vec{f}(\vec{r},t) = \left[\vec{P}(\vec{r},t) \cdot \nabla\right]\vec{E}_m + \frac{\partial \vec{P}(\vec{r},t)}{\partial t} \times \vec{B}_m(\vec{r},t)$$

where $\vec{E}_m$ and $\vec{B}_m$ are the electric and magnetic fields within the medium, respectively. $\vec{P} = \varepsilon_m \alpha \vec{E}$ is the dipole moment density assumed to be proportional to

---

[1]The simplest case is to assume a single dipole in vacuum. Then $\vec{f}$ and $\vec{P}$ are just force and dipole moment [137].

the incident field. $\varepsilon_m = n_m^2 \varepsilon_0$ is the permittivity of the medium and $\alpha = \alpha' + i\alpha''$ is the complex, frequency-dependent, first order polarizability (which is a scalar for a homogeneous and isotropic material). Using the vector identity $\left(\vec{E} \nabla \right) \vec{E} = \nabla \left(\vec{E}^2/2 \right) - \vec{E} \times \left(\nabla \times \vec{E} \right)$ and the Maxwell equation $\nabla \times \vec{E} = -\partial/\partial \vec{B}$ one obtains

$$\vec{f} = \frac{\alpha \varepsilon_m}{2} \nabla \left| \vec{E}_m \right|^2 + \alpha \varepsilon_0 \frac{\partial}{\partial t} \left(\vec{E}_m \times \vec{B}_m \right)$$

The first term corresponds to the gradient force and the second term to the scattering force $\vec{f} = \vec{f}_{grad} + \vec{f}_{scat}$. The second term is similar to the Poynting vector $\vec{S} = n_m \varepsilon_0 c^2 \left(\vec{E}_m \times \vec{B}_m \right)$ which describes energy transport of light and is related to the transfer of momentum density $\vec{m} = \vec{S}/c^2$. Thus, the second term can be interpreted as a force (which is the change of momentum) per volume element upon interaction with light [138], i.e. scattering (change of the direction of $\vec{S}$) or absorption (attenuation of $\vec{S}$). Thus, the scattering force averaged over one oscillation period of the electromagnetic field will be of the form

$$\left\langle \vec{f}_{scat} \right\rangle \propto (C_{absorption} + C_{scattering}) \cdot \left\langle \left| \vec{S} \right| \right\rangle$$

The time averaged gradient force[2] is

$$\left\langle \vec{f}_{grad} \right\rangle = \frac{\alpha' \varepsilon_m}{4} \nabla \left| \vec{E}_m \right|^2$$

The gradient force depends on the real part α' of the polarizability. The scattering force can further be determined as follows [140, 141]: A Hertz dipole radiates with an average power T of $\langle T \rangle = |\vec{p}|^2 \omega/(12\pi\varepsilon_0 c^3)$. The scattering cross section is the ratio of scattered to incident power. With $\vec{p} = \alpha \vec{E}$ one can obtain the actual scattering force from the upper equation. Furthermore, Poynting's theorem states that the power dissipated by a dipole is $\langle T \rangle = \omega/2 \cdot Im \left(\vec{p} \cdot \vec{E} \right)$. From that the absorption cross section can be calculated, too, and we obtain the three forces acting on the dipole

$$\left\langle \vec{F_{grad}} \right\rangle = \frac{\alpha' \varepsilon_m}{4} \nabla \left| \vec{E} \right|^2 \tag{6.1}$$

$$\left\langle \vec{F_{abs}} \right\rangle = \frac{n_m k}{\varepsilon_0 c} \alpha'' \left\langle \vec{S} \right\rangle \tag{6.2}$$

$$\left\langle \vec{F_{scat}} \right\rangle = \frac{n_m k^4}{6\pi \varepsilon_0^2} |\alpha|^2 \left\langle \vec{S} \right\rangle \tag{6.3}$$

One naively might assume the polarizability to be simply real for Rayleigh scattering. However it was found for non-absorbing spheres that the polarizability still has an imaginary part due to the radiation reaction of an oscillating dipole, causing a phase shift between $\vec{p}$ and $\vec{E}$ [139, 142–144]. One needs to model the microscopic response of a system to obtain meaningful estimates for the polarizability. A good starting point is the classical electron oscillator (CEO) model [144, 145]: An induced

---

[2]Time-averaging causes $\alpha/2 \rightarrow \alpha'/4$. See also [139].

dipole with oscillation frequency ω_0 is driven by an external electric field, m, q and $\vec{p} = q\vec{x}$ are the mass, charge and dipole moment of the dipole, respectively. The restoring force is assumed to be harmonic and a damping term accounts for radiation of power. The rate constant γ includes radiative and non-radiative decays. The systems obey the differential equation

$$\frac{d^2\vec{x}}{dt^2} + 2\gamma\frac{d\vec{x}}{dt} + \omega_0^2\vec{x} = \frac{q\vec{E}}{m}$$

In frequency space the polarizability is then

$$\alpha(\omega) = \frac{q^2}{m\varepsilon_0}\frac{\omega_0^2 - \omega^2 + 2i\gamma\omega}{(\omega_0^2 - \omega^2)^2 + 4\gamma^2\omega^2} \approx \frac{q^2}{2m\varepsilon_0\omega_0\gamma}\left[\frac{\gamma(\omega_0 - \omega)}{(\omega_0 - \omega)^2 + \gamma^2} + i\frac{\gamma^2}{(\omega_0 - \omega)^2 + \gamma^2}\right]$$
(6.4)

The last expression is valid for a weak damping ($\omega_0 >> \gamma$).

Now it is of interest to relate the microscopic polarizability α to macroscopic quantities like the susceptibility χ, which describes the relation between polarization density and electromagnetic field: $\vec{P} = \varepsilon_0\chi\vec{E}$. In a more general view it takes the role of a memory function, $\vec{P}(\vec{r}, t) = \varepsilon_0 \int_{-\infty}^{\infty}\chi(t - t')\vec{E}(\vec{r}, t')dt'$, similar to the mechanical response function described in section 3.1.3. Consequently, its real and imaginary part are also related by a Kramers-Kronig relation.

The susceptibility is closely related to other macroscopic quantities like the complex dielectric permittivity ε or the complex refractive index n by $\chi(\omega) = \varepsilon(\omega) - 1 = n(\omega)^2 - 1$. For a collection of non-interacting dipoles, the transition from microscopic to macroscopic parameters can be simply made by multiplying with a dipole density per unit volume N: $\vec{P} = N\alpha\vec{E}$, and so

$$\alpha = \varepsilon_0/N \cdot \chi = \varepsilon_0/N \cdot (\varepsilon - 1)$$

For a particle in solution the susceptibility of the surrounding medium also has to be taken into account, so $\chi_{total} = (\chi_{particle} - \chi_{medium})/(1 + \chi_{medium})$. In more complex systems, such as an amorphous or crystalline solid, dipoles interact with each other. Then the Clausius-Mossotti equation [145] has to be employed[3]

$$\alpha = \frac{3}{N\varepsilon}\left(\frac{\varepsilon_{particle}/\varepsilon_{medium} - 1}{\varepsilon_{particle}/\varepsilon_{medium} + 2}\right)$$
(6.5)

With this in hand, one is able to calculate forces on objects well below the wavelength if volume, dielectric constant and the electric field are known. Maxwell's equations in a medium lead to the wave equation $\nabla^2\vec{E} = c^{-2} \cdot \partial_t^2\vec{E}$. The polarization (density) is taken into account via a changed propagation velocity within the dielectric particle, $c = c_0/n(\omega) = c_0/\sqrt{1 + \chi(\omega)}$, with c_0 the speed of light in a vacuum and $n = n' + in''$ the complex, frequency dependent refractive index. The ansatz of a plane wave $\vec{E}(x, t) = \vec{E}_0 e^{-i(\omega t - kx)}$ leads to a relation between wavenumber $k = 2\pi/\lambda$ (in the medium) and radial frequency ω: $k = (n'(\omega) + in''(\omega))/c_0 \omega$. Beer's law for absorption helps to interpret $n(\omega)$:

$$I(\Delta x) = I_0 e^{-a\cdot\Delta x} = \left|\vec{E}_0 e^{-i(\omega t + n'\frac{\omega}{c_0}\cdot\Delta x)}\right|^2 \cdot e^{-2n''\frac{\omega}{c_0}\cdot\Delta x}$$

---

[3]Further corrections to this relation were suggested [143].

On the one hand, the wave travels with a changed phase velocity of n'/c_0 in the medium. This identifies n' as the (macroscopic) refractive index. On the other hand, the intensity will be attenuated according to the absorption coefficient a which is closely related to n'' by $a = 2n''k_0 = 2 \cdot k$.

Wavelength dependence of optical trapping forces

The basic idea of trapping particles near their resonance is that the conservative trapping force (equation 6.1) depends solely on the real part of the polarizability whereas dissipative forces (equations 6.2 and 6.3), which counteract a confinement of the particle, depend strongly on the imaginary part of the polarizability. Figure 6.1 A shows the real and imaginary part of the complex refractive index near an absorption resonance calculated with the CEO model (see equation 6.4 and [146]). By means of the Clausius-Mossotti equation the complex polarizability was then calculated (see fig. 6.1 B).
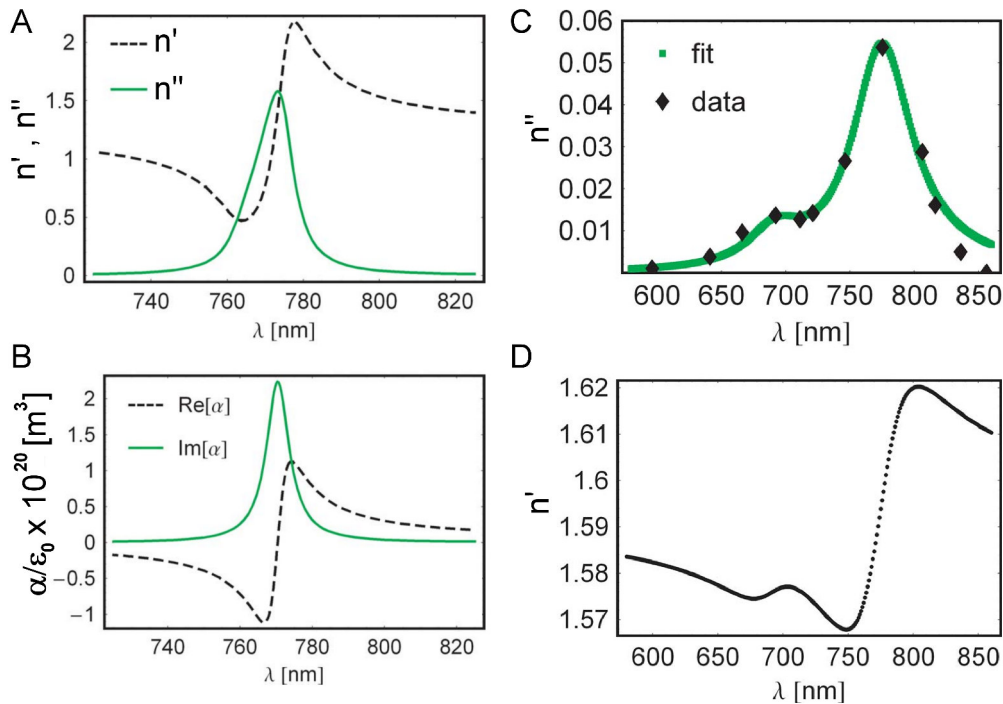

Figure 6.1: Dispersion and absorption of a particle
(A) Complex refractive index near a resonance obtained from the classical electron oscillator. **(B)** Complex polarizability near resonance obtained via the Clausius-Mossotti equation from (A). **(C)** Experimental data (taken by Duke Scientific Inc.) for the imaginary part of the refractive index of a 775 nm fluorescent bead, fit using the CEO model. **(D)** Corresponding real part of the refractive index from the CEO fit in (C). Source: [146]

Qualitatively one can see that the ratio of real and imaginary part of the polarizability increases when approaching the resonance absorption peak from the red-detuned side, which will lead to an increased trap stiffness. The imaginary part of the susceptibility is related to the optical absorption of a material. By a Kramers-Kronig relation its real part can then be calculated. This means that when the

absorption profile of a particle is known over a wide enough wavelength range the three forces exerted by the trapping field (see equations 6.1 - 6.3) can be calculated. Figure 6.1 C shows a fit of the imaginary part of the refractive index according to the CEO to experimental absorption data from a dye-doped polystyrene microsphere, done by Kendrick *et al.* [146]. The according real part of the refractive index is shown as well (6.1 D). The enhancement of trap stiffness was calculated to be approximately 35 %, which was experimentally confirmed.

The absorption spectrum of the CEO conforms to a Lorentzian line shape in the weak damping approximation (see equation 6.4), valid close to resonances. A collection of oscillators with slightly different resonant frequencies can have a Gaussian line shape. Agayan *et al.* [144] found modifications of this absorption profiles to meet the requirements for Kramers-Kronig integration. They assumed a paraxial Gaussian beam focused by a lens as a model for the electromagnetic field corresponding to an optical trap[4].
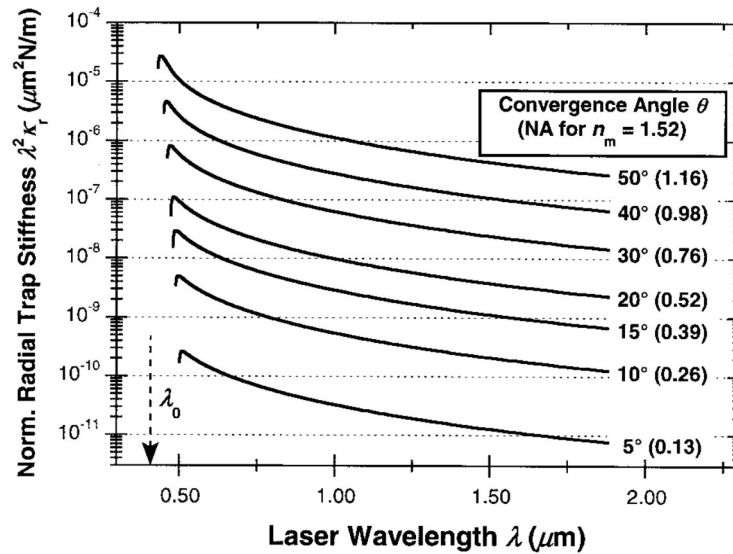
Figure 6.2: **Enhanced trap stiffness near resonance**
Plot of scaled trap stiffness in radial direction over wavelength for different numerical apertures. Calculations were performed on a 10 nm sphere made of pink ruby in a medium with refractive index n_m. The absorption profile with a resonance peak at $\lambda_0 = 406$ nm was fit with a Gaussian. Polarizability was obtained by a Kramers-Kronig relation, assuming a collection of NV non-interacting dipoles. Trapping forces were determined as described in the text. Source: [144]

Figure 6.2 shows the rescaled[5] radial trap stiffness over trapping wavelength for different convergence angles. It reveals that trap stiffness can be increased by about a factor of 50 when comparing values close to and far off from resonances. Radial trap stiffness shows a similar enhancement. The calculations were done for a 10 nm sphere of pink ruby with a Gaussian profile fitted to absorption data[6].

---

[4] For high numerical apertures this approximation breaks down but gives acceptable results for numerical apertures of up to NA=0.78 with average errors of about 15 % of the electric field at the focus.

[5] The potential width scales with wavelength: The Gaussian intensity at the focus is approximated by a harmonic profile $E(r)^2 \propto \exp\left(-2r^2/\omega_0^2\right) \approx 1 - 2r^2/\omega_0^2$, with ω_0 being the radius of the beam waist. This leads to $\kappa \propto 1/\omega_0^2 \propto 1/\lambda^2$, hence a trivial scaling of trap stiffness with the wavelength squared.

[6]If CEO or Lorentzian profiles were used to fit the absorption data, enhancement factors in the range of 2-4 were found.

6.2 | Optical trapping of carbon nanotubes

Carbon nanotubes have diameters on the order of a nanometer. Our preparation methods led to lengths between 100 nm and a few microns. Hence, short CNTs can be small in comparison to visible and NIR wavelengths as described in the previous section. For trapping experiments I used SDBS- and NaDOC-coated CNTs which were diluted in H_2O or D_2O. We found that focused (NIR) laser beams cause a bright spot at the trapping focus which was clearly visible in water and only detectable with the near-infrared sensitive camera. Most likely this is due to Raman scattering in water. After changing to D_2O, the spot was strongly attenuated. With our custom-built setup I was able to trap CNTs, at first with the titanium-sapphire laser. Figure 6.3 shows a series of fluorescence images of the trapping spot. First, a CNT approaches, and then, is clearly and visibly trapped for a few seconds. Finally it exits the trap.
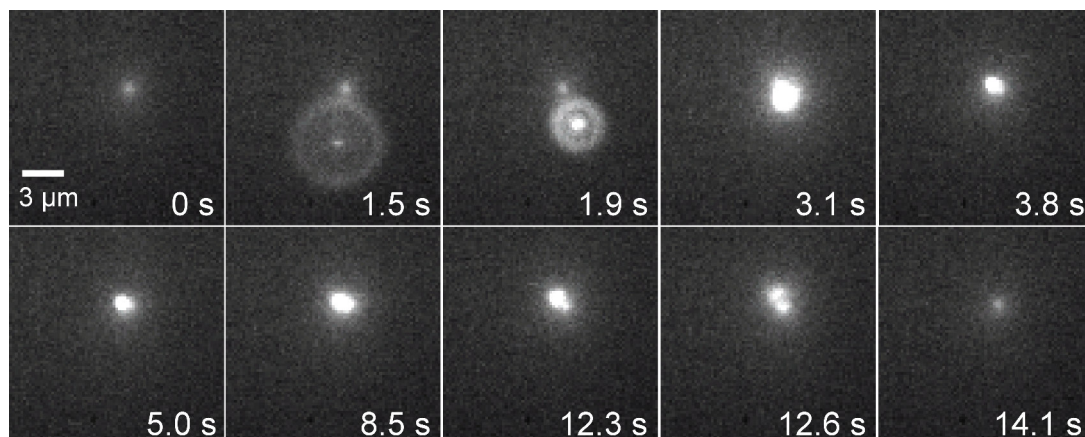

Figure 6.3: Visible proof of optical trapping of carbon nanotubes
Series of fluorescence images of the plain trapping spot (0 s) and a CNT being trapped for approximately ten seconds. Titan sapphire laser at a wavelength of 780 nm and a power of 630 mW was used for trapping SDBS-dispersed CNTs in water.

Trapping of CNTs was hardly reproducible for months. After aligning the setup many times in order to provide optimal trapping parameters, it turned out that the low reproducibility was due to other reasons. Firstly, I tried to trap CNTs with the titanium-sapphire laser (in order to study wavelength effects on trapping), which exhibited laser instabilities and made an interferometric detection impossible (see chapter 2.4.3). So I used fluorescence video microscopy as a benchmark of whether or not a CNT had been trapped. Most of the time the trap seemed empty. It turned out that it was not. Figure 6.4 A shows an image series which demonstrates this. First the trap seems empty. The bright spot is due to Raman scattering in water (which made it even more difficult to determine whether the trap was empty or not). In the consecutive images one sees a long CNT appear. I moved the sample stage to bring it closer to the trap. But instead of being trapped the trap hindered the motion of the long CNT as if it was a solid obstacle. A movement of the stage into the other direction released the CNT immediately, i.e. it was not trapped. The only reasonable explanation is that the trap was filled already (which did not change

the intensity of the bright spot in an observable manner). It might have been filled with other CNTs or with other particles being present in the sample solution. This consideration addresses a second issue which was revealed by another observation: Figure 6.4 B shows an image series of the trapping spot.
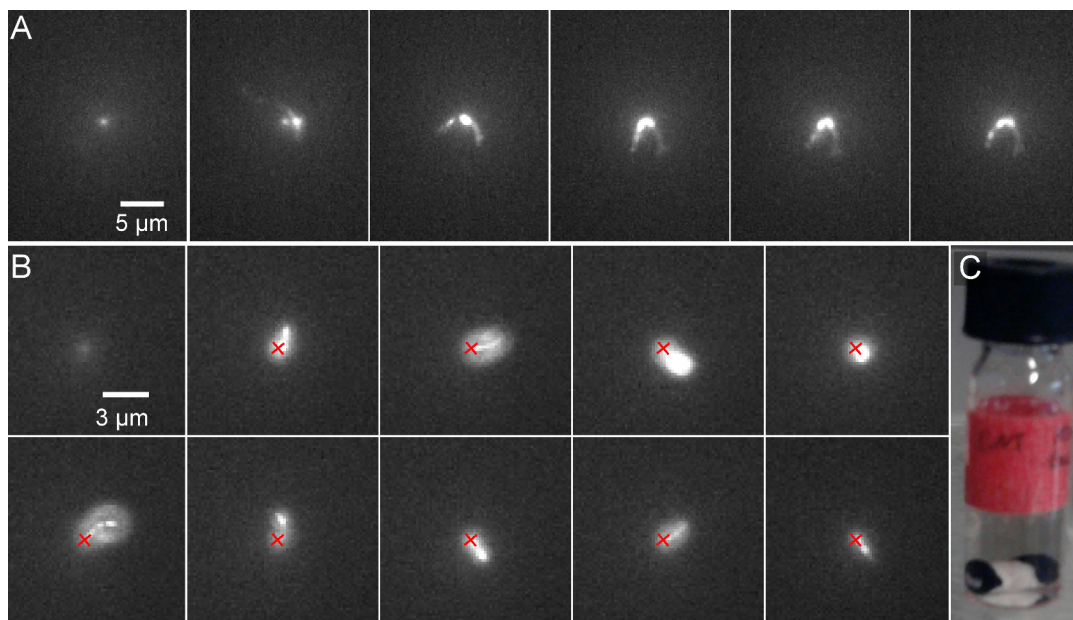
Figure 6.4: Trapping particles other than carbon nanotubes
(A) Series of fluorescence images. The trap seem to be empty (first image) then a CNT appears for about nine seconds. The trap clearly hinders the flow motion of the CNT as if it was a solid obstacle. **(B)** Image series of a trapped CNT taken over 55 seconds. The position of the empty trap (first image) is marked in the consecutive images by a cross. The CNT was stably trapped at one end. With the other end it freely fluctuated around. **(C)** A vial containing the CNT stock solution. The white stirring magnet at the ground is covered at its ends with black CNT raw material.

As before the sample was SDBS-solubilized CNTs diluted in water, hence the trapping spot is visible again. The following images show how a CNT is stably trapped for minutes (first minute shown). The red cross marks the position of the trapping spot in order to demonstrate that the CNT seems to be clamped at one end, whereas the other end is freely fluctuating. It is unlikely that CNTs only interact with one particular segment with the trap, whereas the rest of it remains unaffected. A reasonable explanation for this observation is that a particle which was attached to the CNT, invisible for us, is trapped. As described in section 5.3 our sample CNTs were grown on iron particles used as catalysts. It is a well known fact that not only dielectric but also metallic particles can be trapped [136]. Figure 6.4 C demonstrate convincingly that most of the black CNT raw material in the vial responds to a magnet. CNTs are not magnetic. This further supports the conclusion of iron particles being present in the sample and attached to at least some of the nanotubes. For the experiments of the results presented in the following, I placed a magnet under the sample solution in order to get rid of iron particles.

The second issue which interfered with reproducible trapping became obvious when I tested the same CNT sample on several consecutive days. The CNT stock solution stayed the same between experiments but for each experiment I diluted this

solution. I found a dependence of trappability on the age of the diluted sample. A qualitative test showed that freshly diluted, as well as ten days old samples did not lead to trapping. Only in the three or four days old sample trapping was possible.

This point still remains to be investigated thoroughly in a more quantitative way, but the effect I observed implies that some time-dependent process happens within the sample, triggered upon dilution. After dilution the surfactant concentration is below the critical micelle concentration. This might lead to changes in the CNT's coating, which in turn changes their dielectric properties. This issue remains an open question for future work.

Since fluorescence microscopy alone was insufficient to determine whether CNTs were trapped or not, I expanded the setup to include a 1064 nm laser (see section 2.1 for details) which was stable enough to use it for interferometric position detection. Its trapping and detection capabilities were confirmed by trapping and detecting fluorescent polystyrene beads (see section 2.4.1).
Figure 6.5 shows a dataset taken by simultaneously observing a trapped CNT by fluorescence microscopy and recording its position fluctuations with the interferometric detection system[7]. As a control I recorded the QPD signal for an empty trap. Comparison of the two position-time signals (see fig. 6.5 B) show they differ from each other.

Figure 6.5 C shows power spectra of the QPD signal for x- and y-directions separately. For both directions one sees a clear difference between an empty trap and a trapped particle. At the low and high frequency edge the signal has the same order of magnitude as the noise floor (particularly $1/f$ noise at low frequencies, probably due to laser fluctuations). At intermediate frequencies it well exceeds the signal of the empty trap and the PSD has two regimes, where it follows power laws with different slopes, just like a Lorentzian does. But a least-square fitting of the averaged (30 data point blocks) PSD in the range of 8 to 10,500 Hz reveals a deviation from a Lorentzian form, particularly the PSDs fall of faster than with a Lorentzian slope of -2 at high frequencies.
In some cases more than one CNT was trapped. Figure 6.6 shows an experiment where more and more CNTs entered the trap over time. By video microscopy I could observe CNTs being drawn into the trap one after the other. Simultaneously recorded QPD signals (see fig. 6.6 A) show a broadening of the distribution of positions with respect to the number of particles being trapped. Figure 6.6 B displays corresponding PSDs, showing that they differ from each other when one, two, or multiple particles are trapped.
In order to have an online control of the number of particles in the trap (particularly for the transition of none, one, and two), I extended my custom-written Labview QPD-readout program with a variance calculation (see fig. 6.6 B, inset). It calculates the standard deviation of the position signal for a window of 100 ms. Clear steps in the standard deviation are observed upon consecutive particle entry during the experiment.

---

[7]I assume the voltage output of the QPD to be proportional to the position of the particle relative to the trap. Hence, I will only call it 'position' in the text. Since the orientation dependent drag coefficient of the CNT is not known a proper calibration is not possible.
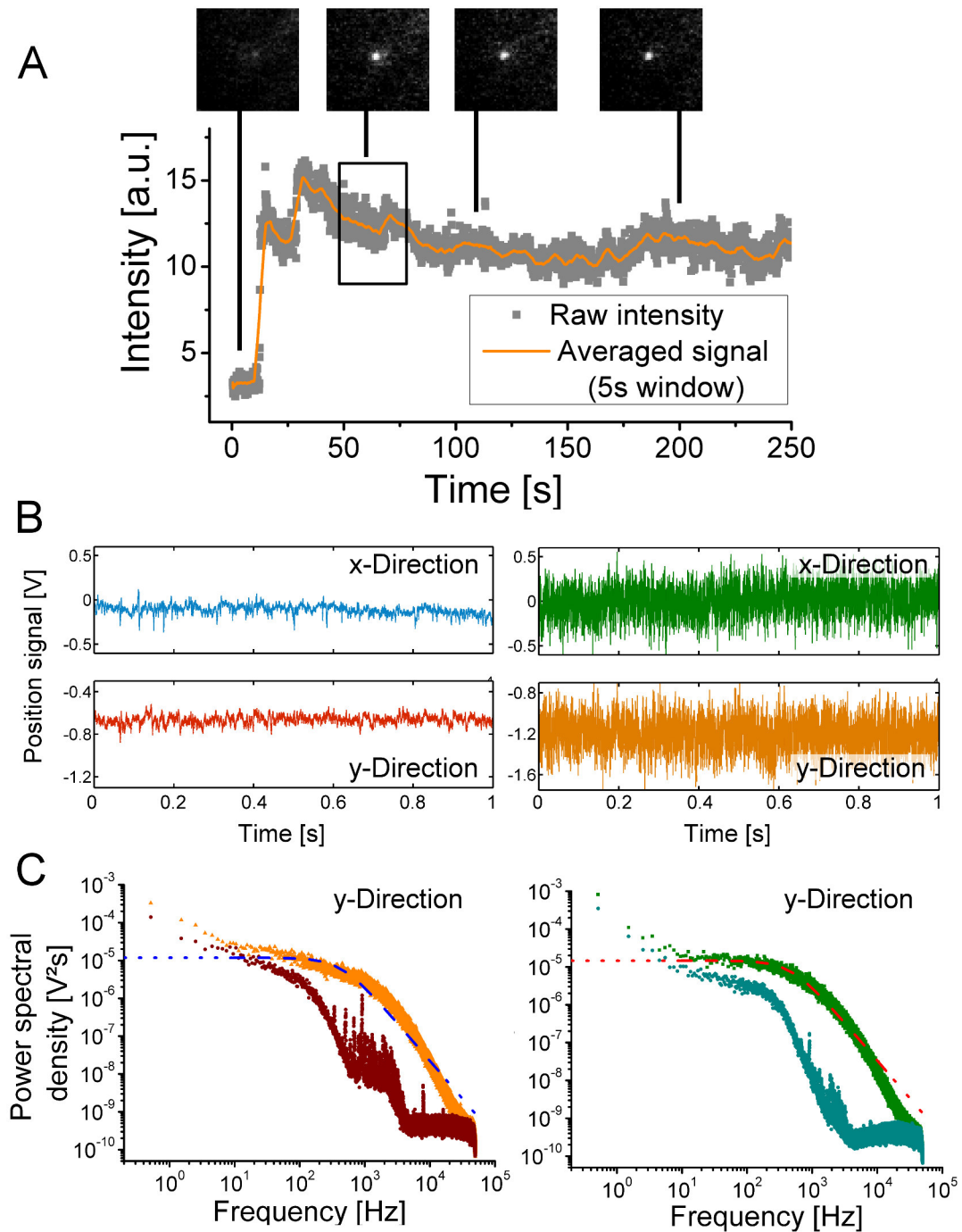
Figure 6.5: Exemplary dataset of a trapped carbon nanotube
(A) Intensity of the trapping spot over time. A fluorescent CNT was visibly trapped, leading to a sharp, step-like increase in the intensity at the trapping spot. Insets show fluorescent images taken at the indicated times. The black rectangle indicates when the recording of the interferometric detection system was taken. **(B)** QPD position signal for an empty trap (left) and when a CNT was trapped (right). The particle position was recorded for thirty seconds (only first second shown) at a sampling frequency of 100 kHz. **(C)** Power spectral densities of the signals shown in (B): Trapped CNT (squares and triangles) and empty trap (circles). Signals were blocked and fitted with a Lorentian function (dashed line) in the range of 8-10,500 Hz. Trapping was done with the 1064 nm laser at a power of 0.8 W.
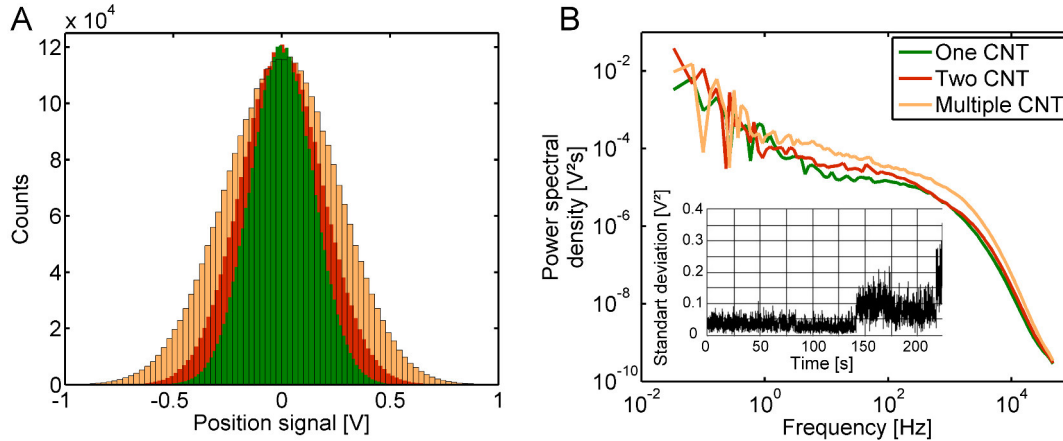
Figure 6.6: Position distribution and power spectral density for multiple trapped carbon nanotubes
(A) Distribution of the QPD position signal in y direction when a single, two or multiple CNTs were trapped. Mean position was subtracted. **(B)** PSDs when a single, two or multiple CNTs were trapped. PSD were logbinned with 100 bins. Inset: Standard deviation of the particle position over time calculated for a 100 ms window. It shows how position variance changes when a second and then multiple particles enter the trap.

Test for resonance effects in optically trapping of nanotubes

Carbon nanotubes are dielectric particles with optical absorption peaking in the visible and near-infrared range of the electromagnetic spectrum. In order to test for a dependence of trapping forces on wavelength, we used different wavelength lasers as trapping sources. Unfortunately the problems described above precluded a quantitative analysis. Thus, I will only state some qualitative results here: Trapping CNTs worked occasionally (see remarks above) for trapping wavelengths of 728 nm, 780 nm and 1064 nm but never with the 561 nm laser. The CNT manufacturer (at Rice University) declared the sample to predominantly contain nanotubes of the (6,5) chirality. I confirmed this by NIR spectroscopy (see section 5.4). The absorption peak of these CNTs was found to be at 567 nm [96]. Thus, the 561 nm laser is almost on-resonance. So it makes sense that trapping was not possible at that wavelength. On-resonance scattering forces become maximal while the gradient force will be negligible.

We tried to use resonance effect as a way to shoot CNTs out of the trap. For that purpose I strongly decreased the illuminated area of the 561 nm laser (or even focused it into the sample) to increase the illumination power density. The 1064 nm laser and 561 nm laser were coincident within the sample plane.
I was not able to see any trapped CNT exiting the trap upon opening the 561 nm laser shutter. Figure 6.7 shows the PSD for each lateral direction of a CNT's position in the trap when solely the 1064 nm trapping laser was activated as well as for the situation when the 561 nm laser was on. The PSDs slightly differ at intermediate frequencies from each other, with CNTs appearing to fluctuate less when the 561 nm laser was switched on.
It is a weak effect and might be explained by a decreased potential well caused by the yellow laser. In the described geometry the additional laser would mainly have an effect along the optical axis, i.e. in z-direction, which was not detected here.
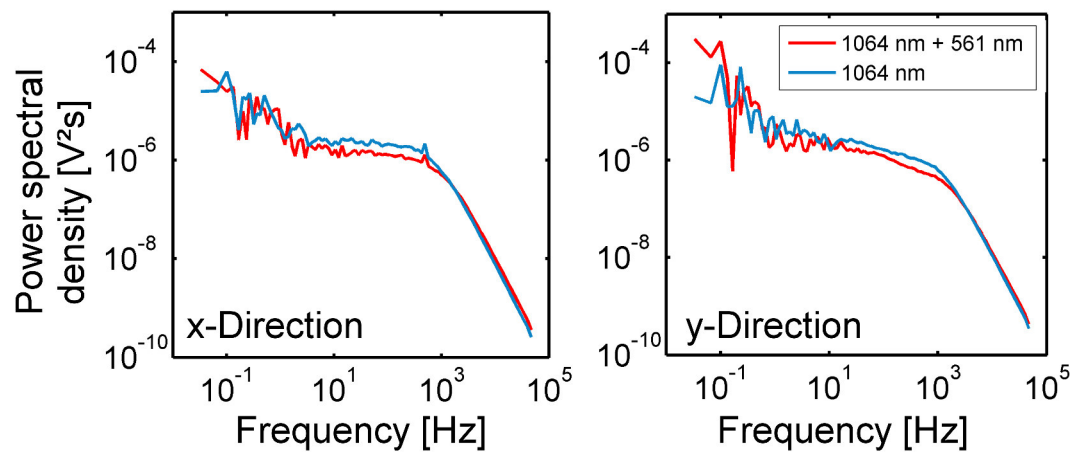
Figure 6.7: Trapped CNT with additional laser on resonance
PSDs of CNT trapped with the 1064 nm laser with and without the 561 nm laser coincident on the trapping spot. Power of the trapping laser was 880 mW. The 561 nm laser was expanded in the sample plane and had a peak power density of 34.4 kW/cm^2.

Nevertheless, the potential well can be approximated to be harmonic around the trapping spot in each direction. The light pressure of the 561 nm laser shifts the mean center-of-mass position of the particle with respect to the potential well of the 1064 nm laser along the optical axis. This results in a more confined lateral motion.

6.3 | **Summary and discussion**

To summarize, I was able to overcome persistent technical/experimental problems and could optically trap carbon nanotubes in our lab. Successful trapping was confirmed by NIR fluorescence video microscopy and simultaneous interferometric detection. In recent years trapping of many nanometer-sized structures has been reported [17]. Nevertheless, there are only a few reports on optically trapped CNTs[8] [147–155]. Most of them describe trapping of bundles or even larger nanotube agglomerates. It has been reported that the fluorescence of CNTs is quenched within bundles [89]. Once individually dispersed, CNT most likely remain fluorescent, even when being close by within the trap. Thus, it is likely that CNTs at the recorded trapping events were single tubes (also supported by their appearance of shape). Moreover, I was able to determine the number of trapped nanotubes with our approach, online, i.e. during the experiment by measuring the standard deviation of the position signal (taken with the interferometric detection).

The power spectral density of such trapped CNTs look similar to a Lorentzian but exhibits some deviation from this functional form. All PSD displayed in figures 6.5 - 6.7 exhibit a power law decay at high frequencies with slopes less than the expected value of -2. In general an oscillating particle in a harmonic potential in an incomperessible fluid has a frequency dependent drag coefficient. Its contribution will make the the PSD decrease faster than at $\sim f^{-2}$ at high frequencies [32]. This might be an explanation for the deviation we see in our experiments. It can also be that the deviations are due to their highly anisotropic shape, however, recent studies on trapped gold nano rods with comparably high aspect ratios presented PSDs in good agreement with a Lorentzian shape [156]. Thus, the origin of the deviation remains to be clarified. Furthermore, PSD plateau values and corner frequencies differ between the recordings presented in figure 6.5 - 6.7. Future investigations will need to quantify this effect.

In this regard, it remains an interesting open question how CNTs align with respect to the optical trap. Selhuber-Unkel *et al.* [156] concluded from their measurements that gold nano rods align with the electric field vector, i.e. perpendicular to the optical axis. For trapped bundles of nanotubes varying orientations were described [149, 150, 152].

When the orientation and geometry of the trapped particle is known, the hydrodynamic friction coefficient can be determined, which then allows for calibration of the optical tweezer. The orientation of a cylindrical particle can in principle be read from the scattered light distribution [157]. Marago *et al.* [152] found that CNT bundles of several microns in length aligned with the optical axis and calculated a maximal force sensitivity of such a force probe to be in the femtonewton range, much lower than that of trapped beads. Single trapped CNT with an even higher aspect ratio than bundles might provide a further enhancement of force sensitivity. Compared to former studies, I used relatively high laser powers, in the range of hundreds of mW. However, I saw that CNTs remained trapped even when the laser power was decreased to 5 mW. This is consistent with previous results [152, 153]. I found two issues that interfered with reproducible trapping: The presence of non-

---

[8]Some of them show trapping indirectly and preliminarily.

fluorescent particles in the sample which occupied the trap and changes of the nanotube coating. Regarding the first point, we found that the HiPCo raw material was attracted by a magnet, indicating the presence of iron particles. It might become a purification method to separate out these particles with a magnet (as we did) in order to improve trapping. The latter point, regarding the CNT coating, is in agreement with findings stating a strong dependence of trapping forces on the used surfactant [153]. In the future this issue can be explored by more quantitative investigations.

To test for resonance effects I added an additional laser to the trap with an emission wavelength close to the absorption resonance of the CNTs. This did not show any strong effect on the particle's motion in the trap. For dye-doped beads the trap stiffness was found to be slightly enhanced when trapped close to resonances. Typically the trapping efficiency for metallic nanoparticles can be increased by illumination close to plasmonic resonances [158, 159] (with the drawback of strong heating due to absorption [160]).

So it is still of great interest to investigate if measurable resonance effects exist for nanotubes. This would not only lead to a more stable trapping at reduced laser powers but also to probe-specific trapping. Both are important within the crowded and radiation-sensitive interior of a cell. It might serve as a sorting or alignment method for material sciences and electronic device fabrication.

Our custom-built setup has different options for further investigations of resonance effects: Preferential trapping of a certain nanotube chirality, as indicated in [151], can be tested with the trap/spectrometer combination. Furthermore, CNT trapping efficiencies at wavelengths of 489 nm, 532 nm, 561 nm, 637 nm, 720-810 nm, 830 nm and 1064 nm can be examined by interferometric detection or by measuring dwell-time distributions of CNTs in the trap with fluorescence microscopy.

To sum up, the work presented here tackled and overcame various technical problems and yielded proof-of-principle CNT trapping and measurements of their trapped dynamics. It also lays the groundwork for further interesting research.

Conclusion | 7

In the presented work I measured the mechanical properties of the cytoplasm of early *Drosophila* embryos and studied optical properties of carbon nanotubes. For that purpose I built a complex measuring setup, capable of imaging multi-colored fluorescent probes simultaneously at kHz frame rates and at normal video rates. This allowed broad band video-based microrheology measurements. I combined existing centroid tracking and microrheology algorithms and added self-written scripts to obtain a collection of analysis programs which extract position PSD and MSD from a series of microscopy images and calculate the shear modulus from it. Applied to the living embryo I found its cytoplasm to be highly viscous. In a region of about 35 μm thickness, between the cortical layer and the central yolk, mechanical properties are homogeneous and the viscosity is approximately thousand times higher than that of water. Close to the nuclear layer, particularly close to the cortex, viscoelasticity increases as expected for the higher density of cytoskeletal filaments. Mechanical response near the nuclear layer is likely to be caused by loosely entangled microtubule networks, whereas in the interior, towards the central yolk, it is due to a macromolecular solution. Besides during nuclear separation at anaphase no signs for non-equilibrium were measurable. Most probable molecular motors act on longer time scales to produce the observed large-scale dynamics during embryonal development. On the one hand, future work will have to address the movements of defined structures, such as centrosomes, in the nuclear layer to analyze the non-equilibrium dynamics. On the other hand, a follow-up investigation could focus on the rheological properties of the actin rich regions near the cortex. For that purpose it is promising to use long CNTs as rheological probes. They are thin enough to enter the existing and fine actin meshwork and still report on mesoscopic fluctuations.

I investigated optical properties of CNTs as a second major subject of the thesis. Therefore, I equipped the setup with near-infrared imaging and spectroscopy instruments as well as multiple trapping lasers and an interferometric detection system. I confirmed CNT's NIR fluorescence characteristics of short fluorescence cycle lifetimes, lacking fluorescence intermittency and a high photostability (though lower than reported before).
I introduced CNTs into the cytoplasm of early fly embryos and found diffusive and subdiffusive motion as well as directed large scale motions, some of them correlating with nuclear motion.
CNTs binding to the targeted kinesin-5 motors could not clearly be confirmed and remains an open task for the future. Nevertheless, this approach opens the possibility to measure molecular dynamics of single force generators and their potential

collective activity in the physiological context of a living organism.

Since these motor proteins accumulate at the centrosomes, CNT-tagged aggregates of them might serve as bright and photostable markers for the mentioned measurement of centrosome fluctuation on a broad time-scale range.

Last, I optically trapped CNTs, simultaneously confirmed by NIR fluorescence microscopy and the interferometric detection. Position PSD of a trapped CNT was close to a Lorentzian shape and the measurement of the position variance allowed a determination of the number of trapped particles. No clear signs for resonance effects on trapping efficiencies were found.

Future work will need to focus on a quantitative calibration of the trap in order to use CNTs as small (intracellular) force sensors or generators. Furthermore, enhanced trapping efficiency due to resonance effects on the radiation forces remain to be investigated. The solution of technical and experimental problems regarding CNT trapping as well as the implementation of multi-fold trapping and detection features into the setup provide a good basis for this task.

Enhanced trapping forces near resonances would not only lead to more stable trapping at reduced laser powers but also to a probe-specific trapping, both important within the crowded and radiation-sensitive interior of a cell.

In summary, this work quantitatively characterized the viscoelasticity inside fly embryos and contributed to the understanding of 'intracellular micromechanics of syncytial *Drosophila* embryos'. Moreover, it set up the basis for further interesting research.

Appendices

Lab protocols, materials and methods $\big|$ A

If not indicated otherwise, all chemicals and materials were obtained from Sigma-Aldrich Chemie Gmbh (Munich, Germany). If not otherwise stated, the term 'beads' describes 1 μm diameter, carboxylated, crimson fluorescent beads (FluoSpheres F-8816, Molecular Probes, Eugene, USA).

Bead immobilization

For bead immobilization described in section 3.3.1 a drop of 10 µl bead solution (concentration 3.7×10^7 particles/ml) was dried out on a glass coverslide and then covered with a 2 wt % agarose gel (Carl Roth GmbH, Karlsruhe, Germany). Fluorescence images were recorded at 20 Hz and 16 kHz.

Glycerol/water control

For the glycerol/water control measurement described in section 3.3.2 Glycerol (Carl Roth GmbH) was mixed with water in different volume fractions of 90%, 70%, 0%, i.e. pure water. Fluorescent beads at a density of 1.1×10^9 particles/ml were added. Video microrheology measurements were taken at 20 Hz and 8 kHz. Theoretical viscosity values were obtained from a webcalculator [1] based on [33]. Control measurements of the viscosity were taken with a cone plate (2° cone plate) rheometer (MCR 501 Rheometer, Anton Paar, Graz, Austria) at a strain amplitude of 1 %.

Drosophila embryo genetics

The following fly strains were used: Nuclei in control and injected embryos were labeled by expression of a Histone 2Av-GFP construct [161]. Microtubules were labeled by expression of cherry-tubulin driven by the Histone2Av promoter (kind gift from C. Lehner, University of Zurich, Zurich, Switzerland). Utrophin-GFP served as a live marker for F-actin [162].
HaloTag-motor plasmids: The vector was a pUAST derivative with ubiquitin promoter (from ubi-E-CadherinGFP-Kinesin-5 fused to halo tag with SV40 transcription termination.

---

[1] $http : //www.met.reading.ac.uk/\tilde{}sws04cdw/viscosity\_calc.html$

Fly stocks were obtained from the Bloomington stock center (Indiana University, Bloomington, IN, USA).

Immunostaining of fly embryos

For immunostaining, embryos were treated as previously described [45]. Embryos were dechorionated with 50% (v/v) bleach, fixed with 37% (v/v) formaldehyde, manually devitellinized and finally rinsed with phosphate-buffered saline (PBS) containing 0.1% (v/v) Tween20. Then they were sequentially incubated in 0.5% (v/v) TritonX-100, in a 5% (w/v) bovine serum albumin solution, in a solution of primary antibody against α-tubulin (B512 clone, Sigma) and in PBS. Embryos were stained with an Alexa568-labeled secondary antibody (Molecular probes) against a tubulin primary antibody, by an Alexa488-labeled phalloidin solution (Molecular probes) and finally with a DAPI (AppliChem) solution with several PBS washing steps in between. Fixed embryos were mounted in Aquapolymount (Polyscience).

Preparation of fly embryos and injection

For all microrheology measurements performed within the fly embryo described in chapter 4 the following procedure was done: Developing embryos were dechorionated by washing them with standard bleach containing 2.8 % sodium hypochlorite (Danklorix, CP GABA, Hamburg, Germany) and then aligned under a stereo microscope and glued (Tesa glue dissolved in heptane) to a coverslip. Next they were desiccated for ten minutes (in a low humidity environment) and covered with halocarbon oil (Voltalef 10S oil, Lehmann & Voss, Hamburg, Germany). Then 1 μm diameter, carboxylated, crimson fluorescent beads (FluoSpheres F-8816, Molecular Probes, Eugene, USA) were pressure-injected with a standard micro-injector (Femtojet Express, Eppendorf, Hamburg, Germany) using custom-pulled borosilicate capillaries. Before injection, the aqueous bead solution (1.1×10^9 particles/ml) was ultrasonicated for three minutes. It was injected into the embryo before the formation of the nuclear layer under an angle of ninety degrees to the long axis straight down towards the substrate approximately 3-6 μm above the surface of the coverslip. The temperature was controlled to be 22.5 ^{o}C. Imaging was performed after the 9th nuclear division when the nuclear layer had formed.

Optionally, chemical agents were injected at the posterior end of the syncytial embryo. The concentrations of injected colcemid (Colcemid, EMD Chemicals, San Diego, CA, USA), latrunculin A (Latrunculin A, Cayman Chemical Company, Ann Arbor, MI, USA) and rho kinase inhibitor Y-27632 (Sigma Aldrich, St. Louis, MO, USA) were 0.1 mg/ml, 1 mM, and 10 mM, respectively.

Injection needles

Two kind of needles were use for the described injection. Needles for bead injection with a long tapper and needles for fluid injection with a short tapper and sharp tip. Needles were pulled from borosilicate capillaries (GB100F-80, 0.58×1.00×80 mm;

Science Products, Hofheim, Germany) with a Sutter pipette puller (P-97; Sutter Instruments Co., Novato, CA, USA) with the following settings:

Long tapper needles:				Short tapper needles:			
Heat	Pull	Velocity	Time	Heat	Pull	Velocity	Time
445	40	50	150	470	100	10	250
Heat ramp value: 440				Heat ramp value: 441			

Bead passivation

For control experiments described in section 4.9 the same tracer particles like in previous experiments, but in a different color (FluoSpheres F-8823, Molecular Probes, Eugene, USA), were passivated with mPEG-NH2 (Poly(ethylene glycol) methyl ether amine 767565, Sigma Aldrich, St. Louis, MO, USA) following the protocol described in [67]:

- 100 µl bead solution (3.3×10^{10} particles/ml) were sonicated (in a bath) for three minutes and then filled into a dialysis bag (Slide-A-Lyzer, 10K MWCO, Thermo Fischer, Waltham, MA, USA)

- Bags were submerged for 2 h in MES buffer (100 mM) at pH 6.0

- Bags were washed three times in water

- Bags were submerged for thirty minutes in a 3.5 ml MES solution 125 mg mPEG-NH2 (equivalent to approx. 125 µl, leading to a concentration of 7,1 mM PEG), 0.7 mM NHS, 2.1 mM EDC.

- Bags were submerged for 8 h in a 3.5 ml borate buffer solution (50 mM borate, pH 8.5) containing 125 mg mPEG-NH2 , 0.7 mM NHS, 2.1 mM EDC. This was repeated two more times.

- Bags were washed for 2 h in borate buffer.

All reactions happened under constant slow stirring. Samples were briefly sonicated at every reaction step.

Proper passivation was tested by fluorescent BSA absorption. 50 µl bead solution (passivated and untreated, respectively) were added to a 1 mg/ml Texas-red-BSA (A23017, Thermo fischer) solution (based on PBS buffer). Beads were incubated for 5 h at 4 °C under slow stirring. Afterwards they were centrifuged three times at 4000 rpm for 30 min and the supernatant was discarded. Fluorescence intensities of plain, untreated probes as well as BSA-exposed probes (passivated and untreated) were compared.

CNT dispersion

A dilute aquaeous dispersion of CNT was prepared by adding the raw HiPco material (batch no. 189.2) to a surfactant solution, either SDBS (sodium dodecylbenzene-sulfonate, 1 % wt) or NaDOC (sodium deoxycholate, 2 % wt). Then the suspension was treated with mild ultra-sonication (7 W, 5-6 s) to obtain long CNT.

The same sample containing DNA-wrapped CNT was used as the one described in [14]: "1.0 mg HiPco SWNTs (batch number 189.2, Rice University) and 2 mg d(T)30 oligonucleotides with an amine-terminated group on the 5' end (Invitrogen) were added to 2 ml DI water in a glass scintillation vial. The vial was placed on ice and sonicated (Vibra Cell, VC-50; Sonics and Materials) at a power of 10 W and 20 kHz for 90 min using a 2-mm diameter microprobe tip. After sonication, the sample was centrifuged at 16000 g for 90 min. The supernatant was carefully collected and filtered using a 4 ml Millipore Amicon ultracentrifuge filter device (MWCO 100 kDa). The SWNT-ssDNA samples thus prepared were stored at 4 ºC."
Same for the preparation of the CNT-Halotag ligand: "SWNT-Halo ligand: 50 mg HaloTag succinimidyl ester (O4) ligand (Promega) was dissolved in 50 μl of dry DMSO (Sigma) and added to 500 μl of 50 mg/l SWNT-ssDNA. The reaction was started by adding 60 μl PBS (10x; Invitrogen) at room temperature and allowed to proceed for 2 h. The excess succinimidyl ester was removed using an Amicon centrifugal filter (MWCO 100 kDa).", copied form [14], *supplementary information.*

Embedding CNT into gels

For Polyacrylamide gel preparation CNT dispersion was mixed with 6 % acrylamide and 0.1 % bisacrylamide in PBS buffer followed by gel polymerization by addition of a 1/100 volume fraction of APS (ammonium persulfate, Sigma) and a 1/1000 volume fraction of TEMED (tetramethylendiamine, Sigma). For agarose gel preparation a drop of CNT solution was dried out on a thin film of a 3 % agarose gel and then covered with an additional layer of agarose.

Detailed list of setup components | B

1. CFI Plan-Apo IR, 60x, NA = 1.27 water; Nikon, Tokyo, Japan

2. α Plan Apochromat 100x/1,46 NA Oil DIC; Zeiss, Göttingen, Germany

3. M-562-xyz ; Newport, Irvine, CA, USA

4. NanoCube P611.3S; Physik Instrumente, Karlsruhe, Germany

5. Piezo Walk Nexact N-381; Physik Instrumente, Karlsruhe, Germany

6. Obis 50 mW, Coherent Inc., Santa Clara, CA, USA

7. Compass 215M 50 mW, Coherent Inc., Santa Clara, CA, USA

8. 500 mW, Cobolt Jive, Cobolt, Solna, Sweden

9. 637 nm 25 mW Cube; Coherent Inc., Santa Clara, CA, USA

10. NDC-25C-2M; Thorlabs, Dachau/Munich, Germany

11. AHWP05M-600; Thorlabs, Dachau/Munich, Germany

12. GL5-A; Thorlabs, Dachau/Munich, Germany

13. z561RDC; Chroma, Vermont, USA , distributor: AHF, Tübingen, Germany

14. z532RDC; Chroma, Vermont, USA , distributor: AHF, Tübingen, Germany

15. z488RDC; Chroma, Vermont, USA , distributor: AHF, Tübingen, Germany

16. AC254-040-A; Thorlabs, Dachau/Munich, Germany

17. AC254-300-A; Thorlabs, Dachau/Munich, Germany

18. Mira 900p 700-820 nm; Coherent Inc., Santa Clara, CA, USA

19. Ophir Spiricon SP 620U, Jerusalem, Isreal

20. AC254-035-B; Thorlabs, Dachau/Munich, Germany

21. AC254-150-B; Thorlabs, Dachau/Munich, Germany

22. AC254-150-A-MR; Thorlabs, Dachau/Munich, Germany

23. AC254-150-A; Thorlabs, Dachau/Munich, Germany

24. AC254-075-A; Thorlabs, Dachau/Munich, Germany

25. 630 DCXR; Chroma, Vermont, USA , distributor: AHF, Tübingen, Germany

26. 900 DCXXR; Chroma, Vermont, USA , distributor: AHF, Tübingen, Germany

27. FF885-Di01; Semrock, Lake Forrest, Illinois, USA; distributor: AHF, Tübingen, Germany

28. zt488/532/561/785tpc; Chroma, Vermont, USA , distributor: AHF, Tübingen, Germany

29. Inject man NI2; Eppendorf, Hamburg, Germany

30. Femto Jet Express; Eppendorf, Hamburg, Germany

31. Xeva-462 XC103, Xenics, Leuven, Belgium

32. 900 lp; Chroma, Vermont, USA , distributor: AHF, Tübingen, Germany

33. Tubuslinse 25; Zeiss, Göttingen, Germany

34. W105BC; Watec, Japan

35. HQ 532/70 M; Chroma, Vermont, USA , distributor: AHF, Tübingen, Germany

36. AC254-060-B; Thorlabs, Dachau/Munich, Germany

37. MXA20696, Nikon, Tokyo, Japan

38. Optosplit III, Cairn Research, Kent, UK

39. HC BS 560imaging; Chroma, Vermont, USA , distributor: AHF, Tübingen, Germany

40. Bright Line HC 511/20; Semrock, Lake Forrest, Illinois, USA; distributor: AHF, Tübingen, Germany

41. Bright Line HC 612/69; Semrock, Lake Forrest, Illinois, USA; distributor: AHF, Tübingen, Germany

42. iXon+ DU-888, Andor Technology, Belfast, UK

43. 555 DCSP; Chroma, Vermont, USA , distributor: AHF, Tübingen, Germany

44. SA1.1, Photron, Bucks, UK

45. ET 570 LP; Chroma, Vermont, USA , distributor: AHF, Tübingen, Germany

46. Acton spectrograph Sp-2150i and InGaAs detector OMA V512-1.7; Princeton Instruments, Trenton NJ, USA

47. Coherent Compass 1064 nm 4 W; Coherent Inc., Santa Clara, CA, USA

48. iQ1C, max. 230 mW, 830 nm; Power Technology, Alexander, AR, USA. Distributor: Laser2000; Wessling, Germany

49. AC254-050-B; Thorlabs, Dachau/Munich, Germany

50. AC254-050-B; Thorlabs, Dachau/Munich, Germany

51. HC BS 885; Chroma, Vermont, USA , distributor: AHF, Tübingen, Germany

52. AC254-030-B; Thorlabs, Dachau/Munich, Germany

53. AC254-100-B; Thorlabs, Dachau/Munich, Germany

54. Aplanatisch-Achromatisher Kondensor 1,4 H, 445453; Zeiss, Göttingen, Germany

55. AC254-250-B; Thorlabs, Dachau/Munich, Germany

56. AC254-045-B; Thorlabs, Dachau/Munich, Germany

57. Quadrant Photo Diode, 0412MS01; Hamamatsu, Hamamatsu, Japan

58. Brightline HC 1064/5; Semrock, Lake Forrest, Illinois, USA; distributor: AHF, Tübingen, Germany

Alignment procedure of the setup | C

All beam paths are aligned along the drill holes of the bread board. So for coarse alignment its feasible to use the L-shaped pinholes and place them along the beam path onto a drill whole. Assuming the detection site of the setup is aligned, one has to do the following steps to align the rest of the setup:

- Remove all lenses and make sure that the beam path of the lasers are aligned with the drill holes. Use mirrors (a) and (b) and mirrors (c) and (d) to align the 1064 nm laser (see fig. C.1). Use mirrors (e) and (f) to align the titanium-sapphire laser. Use the mirrors (g) to (n) to align the diode lasers.

- Place the dichroic mirror (o), which is appropriate for the Nikon objective into the beam path. Place a mirror between (o) and Nikon objective. Tilt the mirror in a way that the lasers are reflected back along their incident beam path. This can be confirmed by coinciding the reflected spot of e.g. the 561 nm laser at the mirror (j). Now turn and tilt (o) in a way that the (strongly attenuated) laser spots fall onto the center of the entrance slits (p) of the image splitter. Control that with the Andor camera. Then replace the mirror between (o) and Nikon objective.

- Place a mirror (or a glass chamber filled with water) into the sample plane of the Nikon objective. Position the Nikon objective in a way that you get a good trap reflection. The central spot should coincide with the center of the two entrance slits (p). The symmetry of the trap reflection should be controlled with another camera (the image splitter uses dielectric mirrors which seem to transmit light intensity differently according to their polarization), e.g. with the Photron camera by placing an appropriate mirror (q) into the beam path. Mark the position of the trap spot on this camera chip and only use one camera to optimize the trap reflection.

- Place an appropriate mirror (o) for the Zeiss objective into the beam path (and replace the tube lens). Now perform the same alignment procedure to obtain good trap reflections. Only the trap reflection of the lasers which will be used for trapping should be as centered and as symmetric as possible. Don't spend too much time with the others. Use the mirrors (c), (d), (o) to obtain a perfect reflection for the 1064 nm laser. Then use (e) to (n) for the rest of the lasers.

- Now switch to the Nikon objective and if necessary reposition it according the reflection.
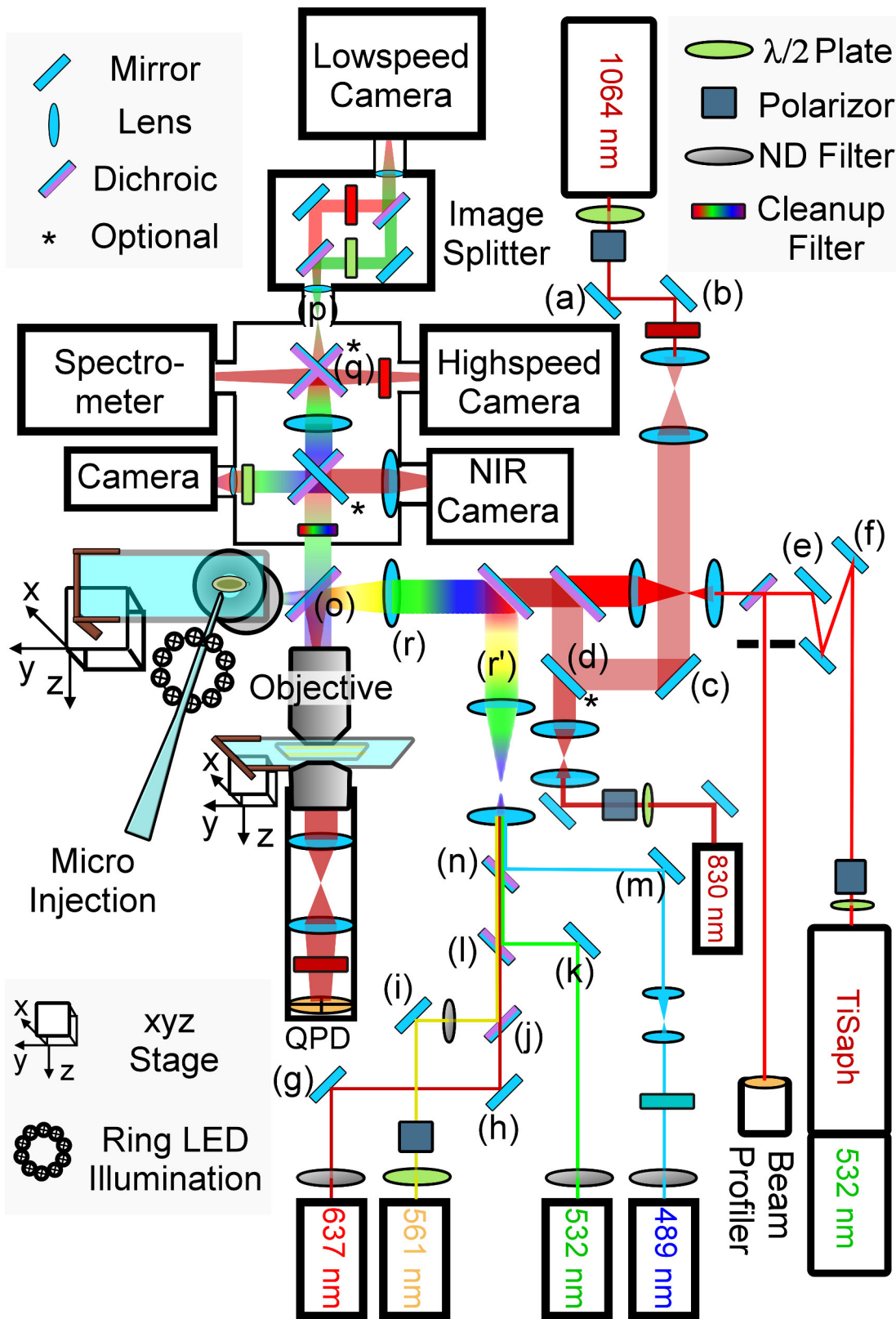
Figure C.1: Setup alignment
Identification of all mirrors needed for alignment.

- Switch back to Zeiss objective and put all lenses back to place. Optimize trap reflections by changing lens positions appropriately. For the diode laser you should choose one laser line to adjust their pair of telescope lenses. Then optimize the trap reflection of the other lasers with their beam steering mirrors (g) to (n).

- According to your application you might want to use wide field microscopy. Therefore, place a lens (r) into the beam path and position it along the xyz-direction to make the beam exit the objective collimated (z-direction) and along the extension axis of the objective symmetry axis (x- and y- direction). Note that there is also a lens which can be placed at position (r') in order to use trapping and wide field microscopy simultaneously.

- The same alignment procedure can be applied to the 830 nm laser after taking mirror (d) out of the beam path.

Alignment of the interferometric detection

If you successfully established a trap in the Zeiss objective follow these steps to align the interferometric detection system:

- Bring the condenser in position, i.e. touching the oil-covered sample coverslip. Unscrew both lenses. Coarse alignment of the condenser (three axis alignment with the three micrometer screws) can be controlled by making sure, that the laser spot which exits the condenser hits the QPD centered. Use a pinhole which can be placed into the Thorlabs cage system to ensure that. For fine alignment, place a 2" mirror right behind the condenser, attached to its back side. This will lead to a second spot looking similar to the actual trap reflection. Use the xyz micrometer screws to make both spots coincide.

- Place the QPD laterally, so that it gives a zero signal.

- Place the first lens laterally so that the QPD signal vanishes.

- Place the second lens laterally so that the QPD signal vanishes.

Description of analysis routines | D

In order to analyze recorded data according to the principles explained in section 3, I used existing Matlab scripts, i.e. the tracking routines from the group of Maria Kilfoil (1) and the microrheology toolbox written by Felix Zörgiebel (2) and added self-written programs (3). Latter ones serve as an interface between the two first collections of scripts but introduce also new analysis methods. The workflow of the whole analysis procedure for video-based microrheology is depicted in figure D.1. All Matlab functions which I contributed will be described in the following. Some of them (called scripts) are only in a preliminary form.

`Analyze_multi_PSD.m`:
This function reads multiple PSDs (`read_multiple_PSD`) from the hard drive. It is the calling function for further analysis: Linearly average a set of power spectral densities (PSDs; `Linearly_average_PSD`), integrate a set of PSDs over a certain frequency range (`integrate_PSD`), fit a set of PSDs (`fit_PSD`), calculate shear moduli from the set of PSDs and truncate them (`truncate_G1PMR`), average and logbin them
(`LogbinAndAverage_G1PMR`) and fit them (`Calc_SlopeAndIntercept_G1PMR`).

`analyse_2_particle_data.m`:
This function reads a dataset of two-particle recordings written and saved by the function `find_two_particle_data`. It prompts a desired interparticle distance range and extracts the particle pairs which fit. Then each particle pair is analyzed one by one, if wanted, calling the function `two_particle_microrheology`, which in turn saves the two particle data.

`average_2PSD.m`:
This script reads two-particle PSD datasets, saved by `two_particle_microrheology`. It averages them in a certain frequency range with a certain number of bins, displays the amount of positively and negatively correlated data points and displays these statistics in a histogram.

`average_G1PMR.m`:
The function gets an array of shear moduli datasets as a parameter. It then calculates maximum and minimum frequency and sets a logarithmically-spaced frequency grid with a specified number of bins. Then it distributes all data points to the according bin and averages all entries in one bin.

Workflow:

```
┌─────────────────────────────────┐
│ Image sequence                  │
└─────────────────────────────────┘

┌──────────────────────────────────────┐
│ Determine tracking parameters        │
│   ↳ Run_feature_finding.m (3)        │
│       ↳ calls mpretrack_init.m (1)   │
└──────────────────────────────────────┘

┌──────────────────────────────────────┐
│ Execute tracking commands            │
│   ↳ feature finding: Mpretrack.m (1) │
│   ↳ tracking: fancy_track.m (1)      │
└──────────────────────────────────────┘

┌────────────────────────────────────────────────────────┐
│ Video microrheology analysis                           │
│   ↳ VMR_analysis.m (3)                                  │
│                                                         │
│       ↳ reads and displays tracking results            │
│                                                         │
│       ↳ further analysis:                              │
│                                                         │
│           ↳ Plot_variance_map.m (3)                    │
│           ↳ find_detection_gaps.m (3)                  │
│           ↳ create_trace_video.m (3)                   │
│           ↳ run_one-particle_microrheology.m (2,3)     │
│           ↳ run_two_particle_microrheology.m (2,3)     │
│           ↳ find_two_particle_data.m (3)               │
│           ↳ MSD_analysis.m (3)                         │
│           ↳ calculate_velocity_distribution.m (3)      │
│           ↳ Analyze_multi_PSD.m (2,3)                  │
│                                                         │
│               ↳ Linearly_average_PSD.m (3)             │
│               ↳ integrate_PSD.m (3)                    │
│               ↳ fit_PSD.m (3)                          │
│               ↳ Calc_SlopeAndItercept_G1PMR.m (3)      │
│               ↳ truncate_G1PMR.m (3)                   │
│               ↳ LogbinAndAverage_G1PMR.m (3)           │
└────────────────────────────────────────────────────────┘
```

Figure D.1: Workflow of the MATLAB analysis script

`Calc_SlopeAndItercept_G1PMR.m`:

This function takes an array of shear moduli datasets and fits a power law to either the full frequency range or a split range. Therefore it uses the function `logfit` (provided by Jonathan Lansey). Resulting fitting parameters are written in to a `result` table.

`calculate_velocity_distribution.m`:

This function is called by `VMR_analysis` and calculates the velocity distribution for a certain time window (`calc_speed`).

`Calc_RMS.m`:

This script extracts position information out of a U-structure and calculates the RMS noise value.

`create_trajectory_video.m`:

This function is called by `VMR_analysis` and reads a certain number of frames from the whole recording. It superimposes the particle trajectories to the image frames and saves them. If wanted it displays the image series as a video. The purpose is to identify particles of interest.

`Error_in_freq_range__emb_av_trunc_G1PMR.m`:

This script takes an array of shear moduli datasets asks for the entries which belong to one experiment (in my case to one embryo) and calculates the mean and variance (SD and SEM) between the experiments for a specified frequency window. The purpose is to compare shear moduli values in one frequency window from different experiments.

`find_detection_gaps.m`:

This function reads the tracking results of `fancytrack` and searches for detection gaps in a user-specified set of trajectories. It then (linearly) interpolates the position of the missed feature in the gap frame. The function `find_NN` finds the next neighbor from this position. A better set of tracking parameters is extracted from the modified feature finding function `mpretrack_init_woOutput` (1,3). This new set of parameters will find the lost feature. This procedure is repeated for all gaps and trajectories. The purpose of this function is to optimize tracking parameters and avoid detection gaps.

`find_two_particle_data.m`:

This function is called by `VMR_analysis` and identifies two-particle pairs in the field of view. It creates a structure containing the benchmark data of the particle pair and appends it to a two-particle data base.

fit_PSD.m:

This function is called by `Analyze_multi_PSD` and takes an array of PSD datasets and fits each curve with a power law (`logfit`, provided by Jonathan Lansey). The PSD can be either fit at the full frequency range or in a split range. Before fitting data is blocked in order to be able to apply a minimized χ^2 fitting approach (see [32] for details).

integrate_PSD.m:

This function is called by `Analyze_multi_PSD` and integrates all assigned PSD curves in a specified frequency range. It suggests the frequency range where all assigned curves overlap.

Linearly_average_PSD.m:

This function takes an array of PSD datasets and averages them over a linear grid with a specified number of bins. In case the maximum number of bins is wanted, it uses a grid with the minimum frequency difference of all datasets. Then it deletes all empty bins and calculates the maximum difference between the remaining frequency points. By that the maximum number of bins is achieved, where no bin is empty.

linearly_interpolate_res.m:

This function linearly interpolates detection gaps in the particle trajectories. If gaps are too long its recommended to use `find_detection_gaps` and redo tracking.

LogbinAndAverage_G1PMR.m:

This is the calling function for `average_G1PMR` and `logbin_G1PMR` which average and logbin an array of shear moduli datasets. Latter function just calls the first function for each single G curve.

LS_TifStackToSeries.m:

This script reads several tiff stacks, appends them and writes them as an image series to a user-specified folder. When recording long image series with the Andor camera it saves them as tiff stacks of a size which can hardly be opened by any other program. Optionally only a region of interest or a subset of frames can be saved.

MSD_analysis.m:

This function is called by `Analyze_multi_PSD` and takes the position trajectories, calculates and plots (`logbin_MSD`, `plot_MSD`) MSDs and saves the datsets to a file: Position trajectories are extracted from the tracking results (`res2MSD`) and for each trajectory (`multi_MSD`) the MSD is calculated (`calc_MSD`, actual MSD calculation happens here) and stored in an MSD data structure. For MSD calculation the distribution of lag times can be chosen as well as if the overlapping or non-overlapping lag intervals are wanted.

`Plot_variance_map.m`:

This function is called by `Analyze_multi_PSD` and calculates the variance of each trajectory. It then plots the variance color-coded into one frame of the image series.

`read_multiple_PSD.m`:

This function reads multiple PSD datasets from the hard drive, either only the last entry of an array of PSDs (reserved for averaged PSD), or all other entries except the last one, or a mixture. This is done by a standard ui-prompt. It stores the origin of the loaded PSD dataset and then appends all datasets to each other. If wanted x- and y- channel will be merged (`PSD_xy_merge`). This multi PSD dataset can be further processed by e.g. `Analyze_multi_PSD.m`.

`run_feature_finding.m`:

This script helps to determine a good set of tracking parameters. It first loads a list of experimental parameters (`parameters.m`) and then calls the feature finding function `mpretrack_init` (1) which displays feature finding results for one frame. If satisfying this is repeated for 80 frames out of the image series to control if important features will be recognized in later images. Finally according feature finding and tracking commands (`Mpretrack()`, `fancytrack()`, (1)) with appropriate parameters are saved to a text file which can be executed later on.

`run_one_particle_microrheology.m`:

This function is the analysis program for one-particle microrheology. It is called by `VMR_analysis`, reads the results from the tracking process (1) and prompts the trajectory numbers which shall be analyzed. It interpolates detection gaps (`linearly_interpolate_res`) and transforms trajectories into a U-file as required for the regular microrheology analysis (`G=A2G1PMR(PSD2A(U2PSD()))`, (2)). There are the following modifications in the analysis procedure: Averaged curves are always appended to the G or PSD data structures, hence new plotting functions are used (`VMR_plot_PSD`, `VMR_plot_G1PMR`). When plotting a PSD it is converted to physical units beforehand (`normalize_to_nm`). A simple PSD averaging is done by `linear_prebin_PSD` before plotting. If wanted the PSD curves can be truncated and interpolated (`truncate_PSD`). Trap correction calculations are circumvented by assigning zero to the trap stiffness.
Finally trajectory plots, PSD plots, G plots as well as PSD datasets and G datasets are saved to hard drive.

`run_two_particle_microrheology.m`:

This function is the analysis program for two-particle microrheology. It is called by `VMR_analysis`. It prompts the desired particle pair, transforms the trajectories into a U-file (`res2U2`) as required for the regular microrheology analysis (`G=A2G2PMR(PSD2A(U2PSD()))`, (2)). Differing from this standard analysis, the PSD can be truncated and interpolated (`truncate_PSD`). Furthermore, a correlation analysis can be performed, where the calibrated Fourier transform of the cross-correlated position signal along the connection axis is plotted linearly and

semi-logarithmically. The imaginary part of the response function will be plotted, too. Moreover, the one-particle shear modulus can be compared with the two-particle shear modulus by plotting them together either in a loglog or a semilog plot.

Finally U-datasets, PSD-datasets and G-datasets as well as all plots are saved to hard drive.

truncate_G1PMR.m:

This function is called by `Analyze_multi_PSD`. It takes an array of non-logbinned shear moduli datasets and plots them with a high number of bins. Then the user can specify a cutoff frequency in the plot (`getDataFromFigure`) where the G-curve shall be truncated. This can be done for all datasets the same or for each dataset individually (real- and imaginary part separately). The purpose of this function is to delete parts of the curve which were affected by the Kramer-Kronig integration (see section 3.2.3).

truncate_PSD.m:

This function takes an array of PSDs (one- or two-particle PSDs) and truncates and interpolates them. Therefore it replots the PSD curves with a finer resolution. The user can now specify the cutoff frequency in the graph (`getDataFromFigure`). This can be done for all curves individually or for all the same. Secondly, one or more frequency ranges can be specified (`getDataFromFigure`) where the curve is interpolated. Therefore PSD data point in a `range` around the interpolation interval are linearly blocked (`linear_blocking`, for details see [32]) and fitted with a power law function (`logfit`, provided by Jonathan Lansey). Then the data is interpolated in this interval. This can be done for all curves the same, for each curve individually or for each curve and each direction individually (for two-particle PSDs this step can be restricted to the parallel PSD curve). The purpose of this function is to delete parts of the curve which were affected by noise (see section 3.2.2).

VMR_analysis.m:

This function loads experimental parameters and tracking settings (`parameters.m`), reads the results of the particle tracking (`load_res`) and hands its over to many possible analysis functions (see D.1).

List of figures

Chapter 4

Chapter 5

Chapter 6

Chapter 7

Page

List of abbreviations

APS   Ammonium persulfate

ATP   Adenosine-5'-triphosphate

BFP   Back focal plane

BSA   Bovine serum albumin

CEO   Classical electron oscillator

CMOS   Complementary metal-oxide-semiconductor

CNT   Carbon nanotube

COOH   Carboxylic acid

DAPI   4',6-diamidino-2-phenylindole

DNA   Deoxyribonucleic acid

EDC   N-(3-Dimethylaminopropyl)-N'-ethylcarbodiimide hydrochloride

EMCCD   electron-multiplying charge-coupled device

GFP   Green fluorescent protein

GTP   Guanosine-5'-triphosphate

InGaAs   Indium Gallium Arsenide

MES   2-(N-morpholino)ethanesulfonic acid

MSD   Mean square displacement

MWCO   Molecular weight cut off

NA   Numerical aperture

NaDOC   Sodium deoxycholate

NIR   Near-infrared

PA   Polyacrylamide

PBS   Phosphate-buffered saline

PEG   Polyethylene glycol

PSD   Power spectral density

QPD   Quadrant photo diode

SD   Standard deviation

SDBS   Sodium dodecylbenzene-sulfonate

SDS   Sodium dodecyl sulfate

SEM   Standard error of the mean

SWNT   Single walled carbon nanotube

TEMED   Tetramethylendiamine

List of references

[1] K. E. Kasza, A. C. Rowat, J. Liu, T. E. Angelini, C. P. Brangwynne, G. H. Koenderink, and D. A. Weitz, "The cell as a material," *Current opinion in cell biology*, vol. 19, no. 1, pp. 101–107, 2007.

[2] D. Wirtz, "Particle-tracking microrheology of living cells: principles and applications," *Annual review of biophysics*, vol. 38, pp. 301–326, 2009.

[3] P. Kollmannsberger and B. Fabry, "Linear and nonlinear rheology of living cells," *Annual Review of Materials Research*, vol. 41, pp. 75–97, 2011.

[4] D. A. Fletcher and R. D. Mullins, "Cell mechanics and the cytoskeleton," *Nature*, vol. 463, no. 7280, pp. 485–492, 2010.

[5] J. Howard *et al.*, "Mechanics of motor proteins and the cytoskeleton," 2001.

[6] P. A. Janmey and C. A. McCulloch, "Cell mechanics: integrating cell responses to mechanical stimuli," *Annu. Rev. Biomed. Eng.*, vol. 9, pp. 1–34, 2007.

[7] J. A. Campos-Ortega and V. Hartenstein, "The embryonic development of drosophilae melanogaster," 1997.

[8] E. D. Schejter and E. Wieschaus, "Functional elements of the cytoskeleton in the early drosophila embryo," *Annual Review of Cell Biology*, vol. 9, no. 1, pp. 67–99, 1993. PMID: 8280474.

[9] V. E. Foe, G. Odell, and B. Edgar, "Mitosis and morphogenesis in the drosophila embryo: point and counterpoint," *The development of Drosophila melanogaster*, vol. 1, pp. 149–300, 1993.

[10] F. C. MacKintosh and C. F. Schmidt, "Active cellular materials," *Current opinion in cell biology*, vol. 22, no. 1, pp. 29–35, 2010.

[11] F. Huber, J. Schnauss, S. Rönicke, P. Rauch, K. Müller, C. Fütterer, and J. Käs, "Emergent complexity of the cytoskeleton: from single filaments to tissue," *Advances in Physics*, vol. 62, no. 1, pp. 1–112, 2013.

[12] F. MacKintosh and C. Schmidt, "Microrheology," *Current Opinion in Colloid & Interface Science*, vol. 4, no. 4, pp. 300–307, 1999.

[13] S. Kruss, A. J. Hilmer, J. Zhang, N. F. Reuel, B. Mu, and M. S. Strano, "Carbon nanotubes as optical biomedical sensors," *Advanced drug delivery reviews*, vol. 65, no. 15, pp. 1933–1950, 2013.

[14] N. Fakhri, A. D. Wessel, C. Willms, M. Pasquali, D. R. Klopfenstein, F. C. MacKintosh, and C. F. Schmidt, "High-resolution mapping of intracellular fluctuations using carbon nanotubes," *Science*, vol. 344, no. 6187, pp. 1031–1035, 2014.

[15] K. Svoboda and S. M. Block, "Biological applications of optical forces," *Annual review of biophysics and biomolecular structure*, vol. 23, no. 1, pp. 247–285, 1994.

[16] D. G. Grier, "A revolution in optical manipulation," *Nature*, vol. 424, no. 6950, pp. 810–816, 2003.

[17] O. M. Maragò, P. H. Jones, P. G. Gucciardi, G. Volpe, and A. C. Ferrari, "Optical trapping and manipulation of nanostructures," *Nature nanotechnology*, vol. 8, no. 11, pp. 807–819, 2013.

[18] J. M. Lerner, "Imaging spectrometer fundamentals for researchers in the biosciences—a tutorial," *Cytometry Part A*, vol. 69, no. 8, pp. 712–734, 2006.

[19] P. Instruments, *Acton Series Monochromators and Spectrographs*. www.princetoninstruments.com, 2014.

[20] J. Lerner and A. Thevenon, "The optics of spectroscopy," *Horiba-Jobin-Yvon tutorial*, 1988.

[21] A. Ashkin, "Forces of a single-beam gradient laser trap on a dielectric sphere in the ray optics regime," *Biophysical journal*, vol. 61, no. 2, pp. 569–582, 1992.

[22] F. Gittes and C. F. Schmidt, "Interference model for back-focal-plane displacement detection in optical tweezers," *Optics letters*, vol. 23, no. 1, pp. 7–9, 1998.

[23] R. W. Bowman and M. J. Padgett, "Optical trapping and binding," *Reports on Progress in Physics*, vol. 76, no. 2, p. 026401, 2013.

[24] W. H. Press, *Numerical recipes 3rd edition: The art of scientific computing*. Cambridge university press, 2007.

[25] F. Gittes and C. F. Schmidt, "Thermal noise limitations on micromechanical experiments," *European biophysics journal*, vol. 27, no. 1, pp. 75–81, 1998.

[26] Thorlabs, *Product catalog*. www.thorlabs.com.

[27] B. Schnurr, F. Gittes, F. MacKintosh, and C. Schmidt, "Determining microscopic viscoelasticity in flexible and semiflexible polymer networks from thermal fluctuations," *Macromolecules*, vol. 30, no. 25, pp. 7781–7792, 1997.

[28] V. Pelletier, N. Gal, P. Fournier, and M. L. Kilfoil, "Microrheology of microtubule solutions and actin-microtubule composite networks," *Physical review letters*, vol. 102, no. 18, p. 188303, 2009.

[29] J. C. Crocker and D. G. Grier, "Methods of digital video microscopy for colloidal studies," *Journal of colloid and interface science*, vol. 179, no. 1, pp. 298–310, 1996.

[30] T. G. Mason and D. Weitz, "Optical measurements of frequency-dependent linear viscoelastic moduli of complex fluids," *Physical review letters*, vol. 74, no. 7, p. 1250, 1995.

[31] F. Zörgiebel, *Viscoelasticity of biopolymer solutions and the mechanical function of topoisomerases investigated with micromechanical trapping techniques.* Diploma thesis, Georg-August-Universität Göttingen, 2009.

[32] K. Berg-Sørensen and H. Flyvbjerg, "Power spectrum analysis for optical tweezers," *Review of Scientific Instruments*, vol. 75, no. 3, pp. 594–612, 2004.

[33] N.-S. Cheng, "Formula for the viscosity of a glycerol-water mixture," *Industrial & engineering chemistry research*, vol. 47, no. 9, pp. 3285–3288, 2008.

[34] W. M. Roberts, J. Howard, and A. J. Hudspeth, "Hair cells: Transduction, tuning, and transmission in the inner ear," *Annual Review of Cell Biology*, vol. 4, no. 1, pp. 63–92, 1988. PMID: 2461723.

[35] A. Mazumdar and M. Mazumdar, "How one becomes many: blastoderm cellularization in drosophila melanogaster," *Bioessays*, vol. 24, no. 11, pp. 1012–1022, 2002.

[36] T. L. Karr and B. M. Alberts, "Organization of the cytoskeleton in early drosophila embryos.," *The Journal of cell biology*, vol. 102, no. 4, pp. 1494–1509, 1986.

[37] W. Sullivan and W. E. Theurkauf, "The cytoskeleton and morphogenesis of the early drosophila embryo," *Current opinion in cell biology*, vol. 7, no. 1, pp. 18–22, 1995.

[38] R. Warn, R. Magrath, and S. Webb, "Distribution of f-actin during cleavage of the drosophila syncytial blastoderm.," *The Journal of cell biology*, vol. 98, no. 1, pp. 156–162, 1984.

[39] R. Warn, "The cytoskeleton of the early drosophila embryo," *Journal of Cell Science*, vol. 1986, no. Supplement 5, pp. 311–328, 1986.

[40] J. Cao, J. Crest, B. Fasulo, and W. Sullivan, "Cortical actin dynamics facilitate early-stage centrosome separation," *Current Biology*, vol. 20, no. 8, pp. 770–776, 2010.

[41] M. Mavrakis, R. Rikhy, and J. Lippincott-Schwartz, "Plasma membrane polarity and compartmentalization are established before cellularization in the fly embryo," *Developmental cell*, vol. 16, no. 1, pp. 93–104, 2009.

[42] J. W. Raff and D. M. Glover, "Centrosomes, and not nuclei, initiate pole cell formation in drosophila embryos," *Cell*, vol. 57, no. 4, pp. 611–619, 1989.

[43] J. T. Blankenship and E. Wieschaus, "Two new roles for the drosophila ap patterning system in early morphogenesis," *Development*, vol. 128, no. 24, pp. 5129–5138, 2001.

[44] T. Idema, J. O. Dubuis, L. Kang, M. L. Manning, P. C. Nelson, T. C. Lubensky, and A. J. Liu, "The syncytial drosophila embryo as a mechanically excitable medium," *PloS one*, vol. 8, no. 10, p. e77216, 2013.

[45] T. Kanesaki, C. M. Edwards, U. S. Schwarz, and J. Grosshans, "Dynamic ordering of nuclei in syncytial embryos: a quantitative analysis of the role of cytoskeletal networks," *Integrative Biology*, vol. 3, no. 11, pp. 1112–1119, 2011.

[46] J. Baker, W. E. Theurkauf, and G. Schubiger, "Dynamic changes in microtubule configuration correlate with nuclear migration in the preblastoderm drosophila embryo," *The Journal of cell biology*, vol. 122, no. 1, pp. 113–121, 1993.

[47] J. M. Scholey, "Kinesin-5 in drosophila embryo mitosis: Sliding filament or spindle matrix mechanism?," *Cell Motility and the Cytoskeleton*, vol. 66, no. 8, pp. 500–508, 2009.

[48] K. M. Addas, C. F. Schmidt, and J. X. Tang, "Microrheology of solutions of semiflexible biopolymer filaments using laser tweezers interferometry," *Physical Review E*, vol. 70, no. 2, p. 021503, 2004.

[49] A. C. Spradling, "Developmental genetics of oogenesis," *The development of Drosophila melanogaster*, vol. 1, pp. 1–70, 1993.

[50] M. Doi and S. Edwards, "The theory of polymer dynamics, 1986," *Claredon, Oxford. ISBN 0-19-852033-6*, 1986.

[51] D. Chen, E. Weeks, J. C. Crocker, M. Islam, R. Verma, J. Gruber, A. Levine, T. C. Lubensky, and A. Yodh, "Rheological microscopy: local mechanical properties from microrheology," *Physical review letters*, vol. 90, no. 10, p. 108301, 2003.

[52] F. Gittes, B. Schnurr, P. Olmsted, F. MacKintosh, and C. Schmidt, "Microscopic viscoelasticity: shear moduli of soft materials determined from thermal fluctuations," *Physical review letters*, vol. 79, no. 17, p. 3286, 1997.

[53] D. C. Morse, "Viscoelasticity of tightly entangled solutions of semiflexible polymers," *Physical Review E*, vol. 58, no. 2, p. R1237, 1998.

[54] F. Gittes and F. MacKintosh, "Dynamic shear modulus of a semiflexible polymer network," *Physical Review E*, vol. 58, no. 2, p. R1241, 1998.

[55] G. Koenderink, M. Atakhorrami, F. MacKintosh, and C. Schmidt, "High-frequency stress relaxation in semiflexible polymer solutions and networks," *Physical review letters*, vol. 96, no. 13, p. 138307, 2006.

[56] B. D. Hoffman, G. Massiera, K. M. Van Citters, and J. C. Crocker, "The consensus mechanics of cultured mammalian cells," *Proceedings of the National Academy of Sciences*, vol. 103, no. 27, pp. 10259–10264, 2006.

[57] M. Atakhorrami, G. H. Koenderink, J. F. Palierne, F. C. MacKintosh, and C. F. Schmidt, "Scale-dependent nonaffine elasticity of semiflexible polymer networks," *Phys. Rev. Lett.*, vol. 112, p. 088101, Feb 2014.

[58] B. R. Daniels, B. C. Masi, and D. Wirtz, "Probing single-cell micromechanics in vivo: The microrheology of c. elegans developing embryos," *Biophysical journal*, vol. 90, no. 12, pp. 4712–4719, 2006.

[59] G. Pesce, L. Selvaggi, A. Caporali, A. C. De Luca, A. Puppo, G. Rusciano, and A. Sasso, "Mechanical changes of living oocytes at maturation investigated by multiple particle tracking," *Applied Physics Letters*, vol. 95, no. 9, p. 093702, 2009.

[60] M. Valentine, Z. Perlman, T. Mitchison, and D. Weitz, "Mechanical properties of xenopus egg cytoplasmic extracts," *Biophysical journal*, vol. 88, no. 1, pp. 680–689, 2005.

[61] D. Mizuno, C. Tardin, C. Schmidt, and F. MacKintosh, "Nonequilibrium mechanics of active cytoskeletal networks," *Science*, vol. 315, no. 5810, pp. 370–373, 2007.

[62] A. Caspi, M. Elbaum, R. Granek, A. Lachish, and D. Zbaida, "Semiflexible polymer network: a view from inside," *Physical review letters*, vol. 80, no. 5, p. 1106, 1998.

[63] J. C. Crocker, M. T. Valentine, E. R. Weeks, T. Gisler, P. D. Kaplan, A. G. Yodh, and D. A. Weitz, "Two-point microrheology of inhomogeneous soft materials," *Physical Review Letters*, vol. 85, no. 4, p. 888, 2000.

[64] A. J. Levine and T. Lubensky, "One-and two-particle microrheology," *Physical review letters*, vol. 85, no. 8, p. 1774, 2000.

[65] M. Buchanan, M. Atakhorrami, J. Palierne, and C. Schmidt, "Comparing macrorheology and one-and two-point microrheology in wormlike micelle solutions," *Macromolecules*, vol. 38, no. 21, pp. 8840–8844, 2005.

[66] T. Savin and P. S. Doyle, "Static and dynamic errors in particle tracking microrheology," *Biophysical journal*, vol. 88, no. 1, pp. 623–638, 2005.

[67] M. Valentine, Z. Perlman, M. Gardel, J. Shin, P. Matsudaira, T. Mitchison, and D. Weitz, "Colloid surface chemistry critically affects multiple particle tracking measurements of biomaterials," *Biophysical journal*, vol. 86, no. 6, pp. 4004–4014, 2004.

[68] B. Fabry, G. N. Maksym, J. P. Butler, M. Glogauer, D. Navajas, and J. J. Fredberg, "Scaling the microrheology of living cells," *Physical review letters*, vol. 87, no. 14, p. 148102, 2001.

[69] J. Alcaraz, L. Buscemi, M. Grabulosa, X. Trepat, B. Fabry, R. Farré, and D. Navajas, "Microrheology of human lung epithelial cells measured by atomic force microscopy," *Biophysical journal*, vol. 84, no. 3, pp. 2071–2079, 2003.

[70] K. M. Van Citters, B. D. Hoffman, G. Massiera, and J. C. Crocker, "The role of f-actin and myosin in epithelial cell rheology," *Biophysical journal*, vol. 91, no. 10, pp. 3946–3956, 2006.

[71] S. Yamada, D. Wirtz, and S. C. Kuo, "Mechanics of living cells measured by laser tracking microrheology," *Biophysical Journal*, vol. 78, no. 4, pp. 1736–1747, 2000.

[72] D. Mizuno, R. Bacabac, C. Tardin, D. Head, and C. F. Schmidt, "High-resolution probing of cellular force transmission," *Physical review letters*, vol. 102, no. 16, p. 168102, 2009.

[73] J. Guck, R. Ananthakrishnan, H. Mahmood, T. J. Moon, C. C. Cunningham, and J. Käs, "The optical stretcher: a novel laser tool to micromanipulate cells," *Biophysical Journal*, vol. 81, no. 2, pp. 767–784, 2001.

[74] Y. Tseng, T. P. Kole, and D. Wirtz, "Micromechanical mapping of live cells by multiple-particle-tracking microrheology," *Biophysical journal*, vol. 83, no. 6, pp. 3162–3176, 2002.

[75] A. W. Lau, B. D. Hoffman, A. Davies, J. C. Crocker, and T. C. Lubensky, "Microrheology, stress fluctuations, and active behavior of living cells," *Physical review letters*, vol. 91, no. 19, p. 198101, 2003.

[76] C. Wilhelm, "Out-of-equilibrium microrheology inside living cells," *Physical review letters*, vol. 101, no. 2, p. 028101, 2008.

[77] M. Guo, A. J. Ehrlicher, S. Mahammad, H. Fabich, M. H. Jensen, J. R. Moore, J. J. Fredberg, R. D. Goldman, and D. A. Weitz, "The role of vimentin intermediate filaments in cortical and cytoplasmic mechanics," *Biophysical journal*, vol. 105, no. 7, pp. 1562–1568, 2013.

[78] T. Gregor, W. Bialek, R. R. d. R. van Steveninck, D. W. Tank, and E. F. Wieschaus, "Diffusion and scaling during early embryonic pattern formation," *Proceedings of the National Academy of Sciences of the United States of America*, vol. 102, no. 51, pp. 18403–18407, 2005.

[79] F. C. MacKintosh and A. J. Levine, "Nonequilibrium mechanics and dynamics of motor-activated gels," *Physical review letters*, vol. 100, no. 1, p. 018104, 2008.

[80] A. J. Levine and F. MacKintosh, "The mechanics and fluctuation spectrum of active gels†," *The Journal of Physical Chemistry B*, vol. 113, no. 12, pp. 3820–3830, 2009.

[81] D. Mizuno, D. Head, F. MacKintosh, and C. Schmidt, "Active and passive microrheology in equilibrium and nonequilibrium systems," *Macromolecules*, vol. 41, no. 19, pp. 7194–7202, 2008.

[82] C. G. Battle, *Mechanics & Dynamics of the Primary Cilium.* PhD thesis, Georg-August-Universität Göttingen, 2013.

[83] B. M. Lansdorp and O. A. Saleh, "Power spectrum and allan variance methods for calibrating single-molecule video-tracking instruments," *Review of Scientific Instruments*, vol. 83, no. 2, p. 025115, 2012.

[84] A. van der Horst, N. R. Forde, *et al.*, "Power spectral analysis for optical trap stiffness calibration from high-speed camera position detection with limited bandwidth," *Optics express*, vol. 18, no. 8, pp. 7670–7677, 2010.

[85] M. Gardel, M. Valentine, J. C. Crocker, A. Bausch, and D. Weitz, "Microrheology of entangled f-actin solutions," *Physical review letters*, vol. 91, no. 15, p. 158302, 2003.

[86] S. Iijima *et al.*, "Helical microtubules of graphitic carbon," *nature*, vol. 354, no. 6348, pp. 56–58, 1991. CNT.

[87] A. Jorio, G. Dresselhaus, and M. Dresselhaus, *Carbon nanotubes: advanced topics in the synthesis, structure, properties and applications*. Springer Verlag, 2008. CNT.

[88] M. Dresselhaus, G. Dresselhaus, and P. Avouris, *Carbon nanotubes: synthesis, structure, properties, and applications*. Springer Verlag, 2001. CNT.

[89] M. O'Connell, S. Bachilo, C. Huffman, V. Moore, M. Strano, E. Haroz, K. Rialon, P. Boul, W. Noon, C. Kittrell, *et al.*, "Band gap fluorescence from individual single-walled carbon nanotubes," *Science*, vol. 297, no. 5581, p. 593, 2002.

[90] L. Van Hove, "The occurrence of singularities in the elastic frequency distribution of a crystal," *Physical Review*, vol. 89, no. 6, pp. 1189–1193, 1953.

[91] L. Cognet, D. Tsyboulski, J. Rocha, C. Doyle, J. Tour, and R. Weisman, "Stepwise quenching of exciton fluorescence in carbon nanotubes by single-molecule reactions," *Science*, vol. 316, no. 5830, p. 1465, 2007. CNT.

[92] F. Wang, G. Dukovic, L. Brus, and T. Heinz, "The optical resonances in carbon nanotubes arise from excitons," *Science*, vol. 308, no. 5723, p. 838, 2005. CNT.

[93] R. Saito, G. Dresselhaus, and M. Dresselhaus, *Physical properties of carbon nanotubes*. Imperial College Pr, 1998. CNT.

[94] K. Arnold, *Photolumineszenzspektroskopie an Kohlenstoffnanoröhren und Entwicklung von Trennungsmethoden*. PhD thesis, Forschungszentrum Karlsruhe. CNT.

[95] R. Hauge, S. Bachilo, R. Smattey, M. Strano, R. Weisman, and C. Kittrell, "Structure-Assigned Optical Spectra of Single-Walled Carbon Nanotubes," *Science*, vol. 298, no. 5602, p. 2361, 2002. CNT.

[96] S. M. Bachilo, M. S. Strano, C. Kittrell, R. H. Hauge, R. E. Smalley, and R. B. Weisman, "Structure-assigned optical spectra of single-walled carbon nanotubes," *Science*, vol. 298, no. 5602, pp. 2361–2366, 2002.

[97] D. Tsyboulski, E. Bakota, L. Witus, J. Rocha, J. Hartgerink, and R. Weisman, "Self-assembling peptide coatings designed for highly luminescent suspension of single-walled carbon nanotubes," *J. Am. Chem. Soc*, vol. 130, no. 50, pp. 17134–17140, 2008. CNT.

[98] J. Aubin, "Autofluorescence of viable cultured mammalian cells.," *Journal of Histochemistry & Cytochemistry*, vol. 27, no. 1, pp. 36–43, 1979.

[99] D. A. Heller, S. Baik, T. E. Eurell, and M. S. Strano, "Single-walled carbon nanotube spectroscopy in live cells: Towards long-term labels and optical sensors," *Advanced Materials*, vol. 17, no. 23, pp. 2793–2799, 2005.

[100] A. Hartschuh, H. Pedrosa, L. Novotny, and T. Krauss, "Simultaneous fluorescence and Raman scattering from single carbon nanotubes," *Science*, vol. 301, no. 5638, p. 1354, 2003. CNT.

[101] J. Lefebvre, Y. Homma, and P. Finnie, "Bright band gap photoluminescence from unprocessed single-walled carbon nanotubes," *Physical review letters*, vol. 90, no. 21, p. 217401, 2003. CNT.

[102] D. Tsyboulski, S. Bachilo, and R. Weisman, "Versatile visualization of individual single-walled carbon nanotubes with near-infrared fluorescence microscopy," *Nano Lett*, vol. 5, no. 5, pp. 975–979, 2005. CNT.

[103] S. Berciaud, L. Cognet, and B. Lounis, "Luminescence decay and the absorption cross section of individual single-walled carbon nanotubes," *Physical review letters*, vol. 101, no. 7, p. 077402, 2008.

[104] J. A. Fagan, J. R. Simpson, B. J. Bauer, S. H. De Paoli Lacerda, M. L. Becker, J. Chun, K. B. Migler, A. R. Hight Walker, and E. K. Hobbie, "Length-dependent optical effects in single-wall carbon nanotubes," *Journal of the American Chemical Society*, vol. 129, no. 34, pp. 10607–10612, 2007.

[105] N. Fakhri, D. A. Tsyboulski, L. Cognet, R. B. Weisman, and M. Pasquali, "Diameter-dependent bending dynamics of single-walled carbon nanotubes in liquids," *Proceedings of the National Academy of Sciences*, vol. 106, no. 34, pp. 14219–14223, 2009.

[106] R. Duggal and M. Pasquali, "Dynamics of individual single-walled carbon nanotubes in water by real-time visualization," *Physical review letters*, vol. 96, no. 24, p. 246104, 2006.

[107] J. Crochet, M. Clemens, and T. Hertel, "Quantum yield heterogeneities of aqueous single-wall carbon nanotube suspensions," *J. Am. Chem. Soc*, vol. 129, no. 26, pp. 8058–8059, 2007. CNT.

[108] M. Zheng, A. Jagota, E. Semke, B. Diner, R. McLean, S. Lustig, R. Richardson, and N. Tassi, "DNA-assisted dispersion and separation of carbon nanotubes," *Nature Materials*, vol. 2, no. 5, pp. 338–342, 2003. CNT.

[109] M. Zheng, A. Jagota, M. Strano, A. Santos, P. Barone, S. Chou, B. Diner, M. Dresselhaus, R. Mclean, G. Onoa, *et al.*, "Structure-based carbon nanotube sorting by sequence-dependent DNA assembly," *Science*, vol. 302, no. 5650, p. 1545, 2003. CNT.

[110] D. Tsyboulski, J. Rocha, S. Bachilo, L. Cognet, and R. Weisman, "Structure-dependent fluorescence efficiencies of individual single-walled carbon nanotubes," *Nano Lett*, vol. 7, no. 10, pp. 3080–3085, 2007. CNT.

[111] L. Carlson, S. Maccagnano, M. Zheng, J. Silcox, and T. Krauss, "Fluorescence efficiency of individual carbon nanotubes," *Nano Lett*, vol. 7, no. 12, pp. 3698–3703, 2007. CNT.

[112] P. Cherukuri, S. Bachilo, S. Litovsky, and R. Weisman, "Near-infrared fluorescence microscopy of single-walled carbon nanotubes in phagocytic cells," *J. Am. Chem. Soc*, vol. 126, no. 48, pp. 15638–15639, 2004. CNT.

[113] H. Jin, D. Heller, and M. Strano, "Single-particle tracking of endocytosis and exocytosis of single-walled carbon nanotubes in NIH-3T3 cells," *Nano Lett*, vol. 8, no. 6, pp. 1577–1585, 2008. CNT.

[114] L. Witus, J. Rocha, V. Yuwono, S. Paramonov, R. Weisman, and J. Hartgerink, "Peptides that non-covalently functionalize single-walled carbon nanotubes to give controlled solubility characteristics," *Journal of Materials Chemistry*, vol. 17, no. 19, pp. 1909–1915, 2007. CNT.

[115] P. Barone, S. Baik, D. Heller, and M. Strano, "Near-infrared optical sensors based on single-walled carbon nanotubes," *Nature Materials*, vol. 4, no. 1, pp. 86–92, 2004. CNT.

[116] D. Heller, H. Jin, B. Martinez, D. Patel, B. Miller, T. Yeung, P. Jena, C. H "obartner, T. Ha, S. Silverman, *et al.*, "Multimodal optical sensing and analyte specificity using single-walled carbon nanotubes," *Nature nanotechnology*, vol. 4, no. 2, pp. 114–120, 2008. CNT.

[117] R. N. Day and M. W. Davidson, "The fluorescent protein palette: tools for cellular imaging," *Chemical Society Reviews*, vol. 38, no. 10, pp. 2887–2921, 2009.

[118] F. Pinaud, S. Clarke, A. Sittner, and M. Dahan, "Probing cellular events, one quantum dot at a time," *Nature methods*, vol. 7, no. 4, pp. 275–285, 2010.

[119] G. V. Los, L. P. Encell, M. G. McDougall, D. D. Hartzell, N. Karassina, C. Zimprich, M. G. Wood, R. Learish, R. F. Ohana, M. Urh, *et al.*, "Halotag: a novel protein labeling technology for cell imaging and protein analysis," *ACS chemical biology*, vol. 3, no. 6, pp. 373–382, 2008.

[120] X. Tu, S. Manohar, A. Jagota, and M. Zheng, "Dna sequence motifs for structure-specific recognition and separation of carbon nanotubes," *Nature*, vol. 460, no. 7252, pp. 250–253, 2009.

[121] A. Krüger, *Neue Kohlenstoffmaterialien*. Vieweg+ Teubner Verlag, 2007.

[122] R. M. Dickson, D. Norris, Y.-L. Tzeng, and W. Moerner, "Three-dimensional imaging of single molecules solvated in pores of poly (acrylamide) gels," *Science*, vol. 274, no. 5289, pp. 966–968, 1996.

[123] N. Fakhri, F. C. MacKintosh, B. Lounis, L. Cognet, and M. Pasquali, "Brownian motion of stiff filaments in a crowded environment," *Science*, vol. 330, no. 6012, pp. 1804–1807, 2010.

[124] A. Caspi, R. Granek, and M. Elbaum, "Enhanced diffusion in active intracellular transport," *Physical Review Letters*, vol. 85, no. 26, p. 5655, 2000.

[125] C. P. Brangwynne, G. H. Koenderink, F. C. MacKintosh, and D. A. Weitz, "Cytoplasmic diffusion: molecular motors mix it up," *The Journal of cell biology*, vol. 183, no. 4, pp. 583–587, 2008.

[126] D. Arcizet, B. Meier, E. Sackmann, J. O. Rädler, and D. Heinrich, "Temporal analysis of active and passive transport in living cells," *Physical review letters*, vol. 101, no. 24, p. 248103, 2008.

[127] S. van den Wildenberg, L. Tao, L. Kapitein, C. Schmidt, J. Scholey, and E. Peterman, "The homotetrameric kinesin-5 KLP61F preferentially crosslinks microtubules into antiparallel orientations," *Current Biology*, vol. 18, no. 23, pp. 1860–1864, 2008.

[128] C. Georgi, N. Hartmann, T. Gokus, A. A. Green, M. C. Hersam, and A. Hartschuh, "Photoinduced luminescence blinking and bleaching in individual single-walled carbon nanotubes," *ChemPhysChem*, vol. 9, no. 10, pp. 1460–1464, 2008.

[129] S. Kim, Y. T. Lim, E. G. Soltesz, A. M. De Grand, J. Lee, A. Nakayama, J. A. Parker, T. Mihaljevic, R. G. Laurence, D. M. Dor, *et al.*, "Near-infrared fluorescent type ii quantum dots for sentinel lymph node mapping," *Nature biotechnology*, vol. 22, no. 1, pp. 93–97, 2003.

[130] T. Mitchison and M. Kirschner, "Dynamic instability of microtubule growth," *Nature*, vol. 312, no. 5991, pp. 237–242, 1984.

[131] T. Wittmann, A. Hyman, and A. Desai, "The spindle: a dynamic assembly of microtubules and motors," *Nature cell biology*, vol. 3, no. 1, pp. E28–E34, 2001.

[132] A. Ashkin, "Acceleration and trapping of particles by radiation pressure," *Physical review letters*, vol. 24, no. 4, p. 156, 1970.

[133] A. Ashkin, "Atomic-beam deflection by resonance-radiation pressure," *Physical Review Letters*, vol. 25, no. 19, p. 1321, 1970.

[134] R. Grimm, M. Weidemüller, and Y. B. Ovchinnikov, "Optical dipole traps for neutral atoms," *Advances in atomic, molecular, and optical physics*, vol. 42, pp. 95–170, 2000.

[135] A. Ashkin, J. Dziedzic, J. Bjorkholm, and S. Chu, "Observation of a single-beam gradient force optical trap for dielectric particles," *Optics letters*, vol. 11, no. 5, pp. 288–290, 1986.

[136] K. Svoboda and S. M. Block, "Optical trapping of metallic rayleigh particles," *Optics letters*, vol. 19, no. 13, pp. 930–932, 1994.

[137] W. Wright, G. Sonek, and M. Berns, "Radiation trapping forces on microspheres with optical tweezers," *Applied physics letters*, vol. 63, no. 6, pp. 715–717, 1993.

[138] A. Rohrbach and E. H. Stelzer, "Optical trapping of dielectric particles in arbitrary fields," *JOSA A*, vol. 18, no. 4, pp. 839–853, 2001.

[139] P. Chaumet and M. Nieto-Vesperinas, "Time-averaged total force on a dipolar sphere in an electromagnetic field," *Optics letters*, vol. 25, no. 15, pp. 1065–1067, 2000.

[140] L. Novotny and B. Hecht, *Principles of nano-opticsa*. Cambridge university press, 2012.

[141] C. F. Bohren and D. R. Huffman, *Absorption and scattering of light by small particles*, vol. 10. Wiley New York, 1983.

[142] H. C. Hulst and H. Van De Hulst, *Light scattering by small particles*. Courier Dover Publications, 1957.

[143] B. T. Draine, "The discrete-dipole approximation and its application to interstellar graphite grains," *The Astrophysical Journal*, vol. 333, pp. 848–872, 1988.

[144] R. R. Agayan, F. Gittes, R. Kopelman, and C. F. Schmidt, "Optical trapping near resonance absorption," *Applied optics*, vol. 41, no. 12, pp. 2318–2327, 2002.

[145] C. Gerthsen and D. Meschede, *Gerthsen Physik*. Springer DE, 2010.

[146] M. Kendrick, D. McIntyre, and O. Ostroverkhova, "Wavelength dependence of optical tweezer trapping forces on dye-doped polystyrene microspheres," *JOSA B*, vol. 26, no. 11, pp. 2189–2198, 2009.

[147] S. Tan, H. A. Lopez, C. W. Cai, and Y. Zhang, "Optical trapping of single-walled carbon nanotubes," *Nano Letters*, vol. 4, no. 8, pp. 1415–1419, 2004.

[148] J. Plewa, E. Tanner, D. Mueth, and D. Grier, "Processing carbon nanotubes with holographic optical tweezers," *Optics Express*, vol. 12, no. 9, pp. 1978–1981, 2004.

[149] J. Zhang, H. I. Kim, C. H. Oh, X. Sun, and H. Lee, "Multidimensional manipulation of carbon nanotube bundles with optical tweezers," *Applied physics letters*, vol. 88, no. 5, p. 053123, 2006.

[150] J. Zhang, T. G. Kim, S. C. Jeoung, F. Yao, H. Lee, and X. Sun, "Controlled trapping and rotation of carbon nanotube bundle with optical tweezers," *Optics communications*, vol. 267, no. 1, pp. 260–263, 2006.

[151] T. Rodgers, S. Shoji, Z. Sekkat, and S. Kawata, "Selective aggregation of single-walled carbon nanotubes using the large optical field gradient of a focused laser beam," *Physical review letters*, vol. 101, no. 12, p. 127402, 2008.

[152] O. Marago, P. Jones, F. Bonaccorso, V. Scardaci, P. Gucciardi, A. Rozhin, and A. Ferrari, "Femtonewton force sensing with optically trapped nanotubes," *Nano letters*, vol. 8, no. 10, pp. 3211–3216, 2008.

[153] O. Marago, P. Gucciardi, F. Bonaccorso, G. Calogero, V. Scardaci, A. Rozhin, A. Ferrari, P. Jones, R. Saija, F. Borghese, *et al.*, "Optical trapping of carbon nanotubes," *Physica E: Low-dimensional Systems and Nanostructures*, vol. 40, no. 7, pp. 2347–2351, 2008.

[154] P. J. Pauzauskie, A. Jamshidi, J. K. Valley, J. H. Satcher Jr, and M. C. Wu, "Parallel trapping of multiwalled carbon nanotubes with optoelectronic tweezers," *Applied physics letters*, vol. 95, no. 11, p. 113104, 2009.

[155] M. Donato, S. Vasi, R. Sayed, P. Jones, F. Bonaccorso, A. Ferrari, P. Gucciardi, and O. Maragò, "Optical trapping of nanotubes with cylindrical vector beams," *Optics letters*, vol. 37, no. 16, pp. 3381–3383, 2012.

[156] C. Selhuber-Unkel, I. Zins, O. Schubert, C. So?nnichsen, and L. B. Oddershede, "Quantitative optical trapping of single gold nanorods," *Nano letters*, vol. 8, no. 9, pp. 2998–3003, 2008.

[157] H. Kress, E. H. Stelzer, and A. Rohrbach, "Tilt angle dependent three-dimensional-position detection of a trapped cylindrical particle in a focused laser beam," *Applied physics letters*, vol. 84, no. 21, pp. 4271–4273, 2004.

[158] P. M. Hansen, V. K. Bhatia, N. Harrit, and L. Oddershede, "Expanding the optical trapping range of gold nanoparticles," *Nano letters*, vol. 5, no. 10, pp. 1937–1942, 2005.

[159] E. Messina, E. Cavallaro, A. Cacciola, M. A. Iatì, P. G. Gucciardi, F. Borghese, P. Denti, R. Saija, G. Compagnini, M. Meneghetti, *et al.*, "Plasmon-enhanced optical trapping of gold nanoaggregates with selected optical properties," *ACS nano*, vol. 5, no. 2, pp. 905–913, 2011.

[160] Y. Seol, A. E. Carpenter, and T. T. Perkins, "Gold nanoparticles: enhanced optical trapping and sensitivity coupled with significant heating," *Optics letters*, vol. 31, no. 16, pp. 2429–2431, 2006.

[161] M. Clarkson and R. Saint, "A his2avdgfp fusion gene complements a lethal his2avd mutant allele and provides an in vivo marker for drosophila chromosome behavior," *DNA and cell biology*, vol. 18, no. 6, pp. 457–462, 1999.

[162] M. Rauzi, P.-F. Lenne, and T. Lecuit, "Planar polarized actomyosin contractile flows control epithelial junction remodelling," *Nature*, vol. 468, no. 7327, pp. 1110–1114, 2010.

Acknowledgements/ Danksagung

Curriculum Vitae

Personal data

Name:	**Alok Daniel Weßel**
Address:	Ostlandstraße 34
	37139 Adelebsen
	Germany
E-Mail:	a.d.wessel@phys.uni-goettingen.de
Date of birth:	10/30/1984
Place of birth:	Friedberg (Hesse)
Nationality:	German

Work experience

02/2011-present	Researcher at the CRC SFB 937 for "Collective behavior of soft and biological matter"

Education

02/2011 - 03/2015	**PhD studies in Physics** Georg-August University Göttingen, Germany Third Institute of Physics - Biophysics PhD thesis: "Intracellular micromechanics of the syncytial Drosophila embryo" Supervisor: Prof. Christoph F. Schmidt
since 02/2011	**Member at the Göttingen Graduate School for Neurosciences, Biophysics, and Molecular Biosciences** within the doctoral program "Physics of Biological and Complex Systems"

10/2005 - 10/2010	**Diploma in Physics** (equivalent to M.Sc.) Georg-August University Göttingen, Germany Third Institute of Physics - Biophysics Diploma thesis: "Untersuchung von Kinesin-5-Motorkonstrukten und Kohlenstoffnanoröhren mittels Fluoreszenzmikroskopie" Supervisor: Prof. Christoph F. Schmidt
09/2004 - 05/2005	**Community service** Wohnen und Betreuung, Göttingen, Germany
07/1995 - 06/2004	**Abitur** (final secondary-school degree) Geschwister-Scholl-Gesamtschule, Göttingen, Germany

Publications

Biophysical Journal	Thiede, Christina and Lakämper, Stefan and Wessel, Alok D and Kramer, Stefanie and Schmidt, Christoph F, "A chimeric kinesin-1 head/kinesin-5 tail motor switches between diffusive and processive motility", vol. 104, no. 2, pp. 432–441, 2013.
Science	N. Fakhri, A. D. Wessel, C. Willms, M. Pasquali, D. R. Klopfenstein, F. C. MacKintosh, and C. F. Schmidt, "High-resolution mapping of intracellular fluctuations using carbon nanotubes", vol. 344, no. 6187, pp. 1031?1035, 2014.
Biophysical Journal	Alok D. Wessel, Maheshwar G. Reddy, Jörg Grosshans, Christoph F. Schmidt, "The mechanical properties of early Drosophila embryos measured by high-speed video microrheology", accepted

March, 2015